

DISSERTATION

EXPECTED DISTANCES ON HOMOGENEOUS MANIFOLDS AND NOTES ON PATTERN
FORMATION

Submitted by

Brenden Balch

Department of Mathematics

In partial fulfillment of the requirements

For the Degree of Doctor of Philosophy

Colorado State University

Fort Collins, Colorado

Fall 2023

Doctoral Committee:

Advisor: Patrick Shipman

Mark Bradley
Clay Shonkwiler
Chris Peterson
Hua Chen

Copyright by Brenden Balch 2023

Rights Reserved

ABSTRACT

EXPECTED DISTANCES ON HOMOGENEOUS MANIFOLDS AND NOTES ON PATTERN FORMATION

Flag manifolds are generalizations of projective spaces and other Grassmannians: they parametrize flags, which are nested sequences of subspaces in a given vector space. These are important objects in algebraic and differential geometry, but are also increasingly being used in data science, where many types of data are properly understood as subspaces rather than vectors. In Chapter 1 of this dissertation, we discuss partially oriented flag manifolds, which parametrize flags in which some of the subspaces may be endowed with an orientation. We compute the expected distance between random points on some low-dimensional examples, which we view as a statistical baseline against which to compare the distances between particular partially oriented flags coming from geometry or data.

Lens spaces are a family of manifolds that have been a source of many interesting phenomena in topology and differential geometry. Their concrete construction, as quotients of odd-dimensional spheres by a free linear action of a finite cyclic group, allows a deeper analysis of their structure. In Chapter 2, we consider the *problem of moments* for the distance function between randomly selected pairs of points on homogeneous three-dimensional lens spaces. We give a derivation of a recursion relation for the moments, a formula for the k^{th} moment, and a formula for the moment generating function, as well as an explicit formula for the volume of balls of all radii in these lens spaces.

Motivated by previous results showing that the addition of a linear dispersive term to the two-dimensional Kuramoto-Sivashinsky equation has a dramatic effect on the pattern formation, we study the Swift-Hohenberg equation with an added linear dispersive term, the dispersive Swift-Hohenberg equation (DSHE) in Chapter 3. The DSHE produces stripe patterns with spatially

extended defects that we call seams. A seam is defined to be a dislocation that is smeared out along a line segment that is obliquely oriented relative to an axis of reflectional symmetry. In contrast to the dispersive Kuramoto-Sivashinsky equation, the DSHE has a narrow band of unstable wavelengths close to an instability threshold. This allows for analytical progress to be made. We show that the amplitude equation for the DSHE close to threshold is a special case of the anisotropic complex Ginzburg-Landau equation (ACGLE) and that seams in the DSHE correspond to spiral waves in the ACGLE. Seam defects and the corresponding spiral waves tend to organize themselves into chains, and we obtain formulas for the velocity of the spiral wave cores and for the spacing between them. In the limit of strong dispersion, a perturbative analysis yields a relationship between the amplitude and wavelength of a stripe pattern and its propagation velocity. Numerical integrations of the ACGLE and the DSHE confirm these analytical results.

Chapter 4 explores the measurement and characterization of order in non-equilibrium pattern forming systems. The study focuses on the use of topological measures of order, via persistent homology and the Wasserstein metric. We investigate the quantification of order with respect to ideal lattice patterns and demonstrate the effectiveness of the introduced measures of order in analyzing imperfect three-dimensional patterns and their time evolution. The paper provides valuable insights into the complex pattern formation and contributes to the understanding of order in three dimensions.

ACKNOWLEDGEMENTS

The project in Chapter 1 grew out of conversations in the Pattern Analysis Lab at Colorado State University, and we are very grateful to all of the participants in the lab for ongoing inspiration. This work was partially supported by the National Science Foundation (ATD #1712788, CCF-BSF:CIF #1830676, CP) and the Simons Foundation (#354225, CS).

We thank all the participants in the Pattern Analysis Lab at Colorado State University for their energy, ideas, and ongoing inspiration, Tom Needham for enlightening conversations, the anonymous referee for a number of helpful comments, and the National Science Foundation (CCF-BSF:CIF #1712788, ATD #1830676, CP) and the Simons Foundation (#354225, CS) for their support of the material in Chapter 2.

The work in Chapter 3 was supported by Grants DMS-1814941 and DMR-2116753 awarded by the U.S. National Science Foundation.

The endeavor in Chapter 4 was supported by Grant DMS-1814941 awarded by the U.S. National Science Foundation.

TABLE OF CONTENTS

ABSTRACT	ii
ACKNOWLEDGEMENTS	iv
LIST OF TABLES	vii
LIST OF FIGURES	viii
Chapter 1	Expected Distances on Manifolds of Partially Oriented Flags 1
1.1	Introduction 1
1.2	Flags and Partially Oriented Flags 3
1.3	$SO(3)$ and Lifts to the 3-Sphere 7
1.3.1	Lifting for Analytic Computation 8
1.3.2	Monte Carlo Methods 10
1.4	Expected Distances Between Partially Oriented Flags 12
1.4.1	S^2 and $\mathbb{R}P^2$ 13
1.4.2	Flags with $\lambda = (1, 1, 1)$ 14
1.5	Conclusion and Open Questions 20
Chapter 2	Distributions of Distances and Volumes of Balls in Homogeneous Lens Spaces 22
2.1	Introduction 22
2.2	Lens Spaces 25
2.2.1	Coordinate systems 27
2.3	Algorithms and Experiments 28
2.4	Distributions of Distances 31
2.5	Concluding Remarks 40
Chapter 3	Spatially Extended Dislocations Produced by the Dispersive Swift-Hohenberg Equation 41
3.1	Introduction 41
3.2	The Dispersive Swift-Hohenberg Equation 44
3.3	The Strongly Dispersive Limit 45
3.4	Near-Threshold Behavior 49
3.5	Numerical simulations 51
3.5.1	Simulations of the Dispersive Swift-Hohenberg Equation 52
3.5.2	Simulations of the Amplitude Equation 58
3.6	Discussion 67
3.7	Conclusions 69
Chapter 4	Topological Measure of Order 71
4.1	Introduction 71
4.2	Measures of order 72
4.2.1	Persistent Homology and the Wasserstein Metric 72
4.2.2	Delaunay Triangulation 75

4.3	A note on ideal lattices	79
4.4	Perturbed Lattices	83
4.4.1	Single Point Perturbations	83
4.4.2	Random perturbations	83
4.5	Pattern Formation in Three Dimensions	85
4.5.1	Linear Dispersive Terms	85
4.5.2	Forced Swift-Hohenberg Equation	87
4.6	Conclusions	99
Chapter 5	Discussion of open problems	100
5.1	Moduli Space of Bravais Lattices	100
5.2	Close-Packed Lattices	101
5.3	H_1 count of a random set points	101
5.4	Linear Dispersive Terms in Non-Equilibrium Pattern Forming Systems	105
5.5	Forced SH Equation	106
Bibliography	107

LIST OF TABLES

- 2.1 Values of the k th moment of distance $I_{n,k}$ for small k and $n \geq 3$ 34
- 2.2 $\lim_{n \rightarrow \infty} I_{n,k}$ for small k . The coefficient of π is the coefficient of $n \tan \frac{\pi}{n}$ in the corresponding entry in Table 2.1, and the remaining term is the constant term from Table 2.1. 37

LIST OF FIGURES

1.1	Tower of flags for $\lambda = (1, 1, 1)$	6
1.2	On the left is the Young diagram corresponding to the partition $\lambda = (4, 3, 2, 2, 1)$. The conjugate Young diagram is on the right, with corresponding partition $\bar{\lambda} = (5, 4, 2, 1)$	7
1.3	Stereographic projection to \mathbb{R}^3 of join coordinates on \mathbb{S}^3 . θ_1 and θ_2 are simply the arguments of the two complex coordinates, while α gives the angle a given vector makes with the z_1 -plane. The level sets of α are generically tori, collapsing to the unit circle in the z_1 -plane when $\alpha = 0$ and to the unit circle in the z_2 -plane (which stereographically projects to the z -axis) when $\alpha = \pi/2$	17
2.1	A fundamental domain of the lens space $L(n; m)$. The arrows indicate the directions of the join coordinates $(\theta_1, \theta_2, \eta)$ that will be defined on page 27.	25
2.2	Histograms of distances in $L(5; 1)$ and $L(5; 2)$	30
2.3	Histogram of distances between 10,000,000 random points on $L(3; 1)$ generated by Algorithm 6 compared to the pdf $f_3(x) = \frac{6}{\pi} (\sin^2 x + \Theta(x - \pi/3)(-\sin^2 x + \sqrt{3} \sin x \cos x))$	38
2.4	The cumulative distribution function of distance on $L(n; 1)$ for $2 \leq n \leq 6$ and in the limit as $n \rightarrow \infty$	39
3.1	The first row depicts solutions to Eq. (3.8) on the spatial domain $x \in [-100, 100]$, and the second row shows the corresponding PSDs. In all cases, $\mu = 0.1$, which is near the threshold for pattern formation. From left to right, $\gamma = 0, 25, 50, 75$ and 100. All images are for time $t = 100$	53
3.2	Comparison of Eq. (3.22) to simulation results for values of γ between 1 and 100. Each data point gives the relative error of the amplitude for the corresponding value of γ . In each simulation, $\mu = 1$, the domain was $x \in [-100, 100]$, and the measurements were taken at $t = 100$. We note that the relative error is less than 1% for values of γ larger than 50, and decreases as γ increases.	54
3.3	The phase velocity of the steady-state propagating solution versus γk^2 , as computed from numerical simulations (+'s). Each point is the result of a single simulation with $\mu = 1$ and a value of γ between 1 and 100. The solid line shows the theoretical prediction. The domain for each simulation was $x \in [-100, 100]$, and the velocities were calculated at time $t = 100$	55
3.4	Solutions to Eq. (3.4) with parameters $\mu = \beta = 1$ on the domain $(x, y) \in [-100, 100]^2$. The values of γ are the 0, 10 and 100 for the first, second and third pairs of rows, respectively. In each pair of rows, the first row shows the solution at the times listed and the second row shows the corresponding PSDs. The columns from left to right depict the solutions at times $t = 30, 60, 100, 500$ and 1500.	57
3.5	(a) A solution to Eq. (3.4) at time $t = 40$ that was started with a low amplitude spatial white noise initial condition. Note the chain of three defects between the horizontal lines. (b) A solution to Eq. (3.4) with a banded initial condition of the form (3.47) at time $t = 100$. The initial condition had $n_1 = 28$ and $n_2 = 31$. The parameter values were $\mu = \beta = 1$ and $\gamma = 100$ in both (a) and (b).	58

3.6	The time evolution of a solution to Eq. (3.4) with $\mu = \beta = 1$ and $\gamma = 100$ is shown in the first row. The domain is $(x, y) \in [-100, 100]^2$. The phase velocity in the x direction was computed for each of the cuts parallel to the x axis that are shown. The second row shows the observed velocities along each cut (+’s) versus the velocities predicted by Eq. (3.29) (solid lines).	59
3.7	A solution to Eq. (3.4) with the parameter values $\mu = \beta = 1$ and $\gamma = 100$ on the domain $(x, y) \in [-100, 100]^2$ at times (a) $t = 25$, (b) $t = 50$ and (c) $t = 500$. The initial condition was given by Eq. (3.47) with k_1 and k_2 chosen so that $n_1 = 25$ and $n_2 = 31$.	59
3.8	Solutions to Eq. (3.4) on the domain $(x, y) \in [-100, 100]^2$ are shown at time $t = 100$. The parameter values are $\mu = \beta = 1$ for each panel, and $\gamma = 0, 2,$ and 50 , as labelled. The initial conditions were given by Eq. (3.47) with k_1 and k_2 chosen so that $n_1 = 28$ and $n_2 = 31$. There are therefore $n_2 - n_1 = 3$ defects in each chain.	60
3.9	Solutions to Eq. (3.4) on the domain $(x, y) \in [-100, 100]^2$. The parameter values are $\mu = \beta = 1$ and $\gamma = 50$. The initial conditions were given by Eq. (3.47). Panel (a) shows a solution at time $t = 100$ with $n_1 = 31$ and $n_2 = 30$, and panel (b) shows a solution at time $t = 50$ with $n_1 = 31$ and $n_2 = 25$.	60
3.10	Two simulations of Eq. (3.48) starting from low amplitude spatial white noise initial conditions are shown at time $t = 60$. In panels (a) and (b), the amplitude $ A $ is plotted as a function of x for $\eta = 10$ and 100 , respectively. The corresponding phase ϕ is depicted in panels (a’) and (b’).	62
3.11	The time evolution of three simulations of Eq. (3.46) on the spatial domain $(x, y) \in [-100, 100]^2$. Rows (a)-(e), (f)-(j), and (k)-(o) show the magnitude of the solution $ A(x, y, t) $ for $\eta = 0, 10$ and 100 , respectively. Rows (a’)-(e’), (f’)-(j’), and (k’)-(o’) show the corresponding phases $\phi(x, y, t)$. The solution at times $t = 50, 250, 500, 1000$ and 2500 is shown in columns 1 through 5, respectively.	63
3.12	Chains of spiral waves created by simulating Eq. (3.46) with a banded initial condition of the form given by Eq. (3.49). The spatial domain was $(x, y) \in [-100, 100]^2$ and the snapshot was taken at $t = 100$. We set $\eta = 1$ and the wave numbers q_1 and q_2 were chosen so that $n_1 = 2$ and $n_2 = 5$.	64
3.13	Simulations of Eq. (3.46) with banded initial conditions of the form given by Eq. (3.49) were carried out with q_1 fixed at zero and with $q_2 = \pi n_2/L$, where $n_2 = 2, 3, 4, 5,$ and 7 . The spatial domain was $(x, y) \in [-100, 100]^2$ and η was 100 . The defect velocities and spacings were computed at $t = 200$. The observed values (dots) are compared to the values predicted by Eqs. (3.53) and (3.54) (solid curves).	66
3.14	Simulations were run of Eq. (3.46) with initial conditions given by Eq. (3.49) on the spatial domain $(x, y) \in [-100, 100]^2$, and the average angle ψ that the defects made with the x -axis was computed. This was repeated for $\eta = 5, 10, \dots, 145$ and for $q_2 = n_2\pi/100$ with $n_2 = 2, 3,$ and 4 . In each case, $q_1 = 0$. Each data point represents the average angle obtained from a simulation, while the curve is a fit that is proportional to $1/\eta$. The constant of proportionality depends on Δn .	67

3.15	(a) A simulation of Eq. (3.2) for $\gamma = 5$ at time $t = 65$ that shows the raised and depressed triangular regions traversed by ripples. The initial condition was low amplitude spatial white noise. We employed an 512×512 spatial grid and a time step of $\Delta t = 0.01$. (b) An enlargement of the portion of panel (a) that is outlined in black. The dislocation cores within two seams are circled.	70
4.1	The VR complex of an SC cell whose side lengths are $1/2$. Filtration values of $r = .1, .5$ and $.75$ are shown to capture the different stages the VR complex undergoes. The highlighted edges show a tetrahedron in the center of the cell that kills the H_1 data, and also prevents any H_2 data from being formed.	75
4.2	The VR complex of an FCC cell whose side lengths are $1/2$. Filtration values of $r = .1, .36$ and $.5$ show the different topologies of the FCC VR complex. The highlighted edges are the edges of the octahedron at the center, which begets the H_2 data.	76
4.3	The VR complex of two BCC cells whose side lengths are $1/2$. Filtration values of $r = .1, .45$ and $.5$ show the different stages of the VR complex of the BCC lattice. The highlighted edges show one of the loops that is formed, and eventually dies. There are three others- one around each edge that is shared between the two cells of the lattice.	77
4.4	Delaunay triangulation of single cell for SC, BCC and FCC lattices. Note that the number of neighbors differs between vertices. Thus the coordination number of 3D lattices are not immediately obvious.	78
4.5	The distance distributions of ideal lattices on the domain $[0, 10]^3$ with 10 unit cells. The DT edge length distributions are more distinguishable and are depicted in the first row of Fig. 4.7.	80
4.6	(Top row) From left to right, are the persistence diagrams of ideal SC, BCC and FCC lattices. It is interesting to note that SC and BCC have no H_2 data while the FCC lattice has no H_1 data. (Bottom row) The PDs of an ideal Bravais lattice with a randomly selected single point perturbed. The measures of order (written as $(m_L^0(L_p), m_L^1(L_p), m_L^2(L_p))$) are about SC: (0.2328, 0.4253, 0.0), BCC: (0.4407, 0.4152, 0.1367) and FCC: (0.4614, 0.0487, 0.48).	81
4.7	(First row) The Delaunay triangulation edge length distributions and angle distributions of the ideal lattices. The lattices are all on the domain $[0, 10]^3$ with 64 unit cells. (Second row) The distribution data from the DT of the perturbed lattices- namely an ideal lattice with one randomly chosen point perturbed a small amount. The measures of orders (written $(m_L^e(L_p), m_L^o(L_p))$) are approximately SC: (0.57, 3.33), BCC: (0.24, 1.74) and FCC: (0.24, 1.98).	82
4.8	These figures exhibit the time evolution of the measure of orders of the perturbed SC, BCC, and FCC lattices with respect their ideal form lattices. The first row shows the MoO in the PH case, while the second row shows their MoO in the DT case. In each case, the perturbations were random walks with the initial configuration being an ideal lattice. The left column shows a random walk where the initial starting configuration is an SC lattice. The middle column shows a random walk with initial configuration of a BCC lattice. The right column depicts random walk whose initial configuration is an FCC lattice. In both the SC and BCC cases, the measure of order (in the PH case) contain a spike in the H_2 data- in part because both ideal lattices have no H_2 . Similarly, the H_1 measure of order spikes in the FCC case.	84

- 4.9 The first row depicts solutions of Eqs. (4.7) and (4.8) at $t=5000$. In all cases, the domain is $[-6\pi, 6\pi]^3$ and the parameters used were $A = 2, B = 3.1, C = 1, D_1 = 1$ and $D_2 = 7.1111$. The left column shows a solution obtain with no dispersion. The middle column shows the solution obtained with the dispersive term $P = \partial_x \partial_y \partial_z$ and its corresponding persistence diagram computed from the max locations. The second column shows the solution and its corresponding persistence data with $P = \partial_x^3$ 88
- 4.10 This figure shows the time evolution of the measure of orders with respect to the ideal BCC lattice. Six simulations of Eqs. (4.7) and (4.8) on the domain $[-3\pi, 3\pi]^3$ up to $t=5000$ (the time was cut off to $t=1600$ since perfect order was achieved sooner). Each simulation used low amplitude white-noise initial conditions and the parameters were $A = 2, B = 3.1, C = 1, D_1 = 1$ and $D_2 = 7.1111$. The dispersive term was $P = \partial_x^3$. The mean and confidence intervals of two standard deviations are plotted. 89
- 4.11 Simulations of Eq. 4.9 with SC, BCC and FCC forcing terms respectively. In each case, we used a 64^3 grid on the domain $[-6\pi, 6\pi]^3$ and the parameters $\mu = -.1$ and $\beta = 1.1$. The forcing parameters were $\alpha = 1$ with a 1:1 resonance with $q = 0$. The initial condition were low amplitude white noise and the solutions are shown at $t = 50$. 95
- 4.12 Each figure depicts a collection of 50 simulations of Eq. 4.9 with SC, BCC and FCC forcing terms respectively. The measure of order was computed from the PH of the local maxima at each time step of the solution until $t = 50$. In all the the simulations, low amplitude white-noise initial conditions were used, a 64^3 grid was used on the domain $[-6\pi, 6\pi]^3$ with the parameters $\mu = -.1, \beta = 1.1$ and the forcing parameters $\alpha = 1$ and with $k_f = k_c = 1$. The means of the results are plotted, as well as confidence intervals within 2 standard deviations, with the area between the bands being shaded. 95
- 4.13 Three snapshots of the time evolution of Eq. 4.9 with BCC forcing. A 64^3 grid was used on the domain $[-6\pi, 6\pi]^3$. The parameters were $\mu = -.1$ and $\beta = 1.1$ and the forcing parameters where $\alpha = 1$ and $k_f = k_c = 1$. The times shown are at $t = 4, t = 8$ and $t = 30$ respectively. 96
- 4.14 Each panel depicts the time evolution of the measures of order for 50 simulations of Eq. 4.9. In each case, a 64^3 grid was used on the domain $[-6\pi, 6\pi]^3$. The parameters were $\mu = -.1$ and $\beta = 1.1$. In the first row, the forcing strength was $\alpha = .5$ and in the second row $\alpha = .2$. In all cases, $k_f = k_c = 1$ and the final time was $t = 50$ 96
- 4.15 Each panel depicts the time evolution of the measures of order for 50 simulations of Eq. 4.9. In each case, a 64^3 grid was used on the domain $[-6\pi, 6\pi]^3$. The parameters were $\mu = -.1$ and $\beta = 1.1$. The forcing strength in each simulation was $\alpha = 1$. The forced resonance was 1:1 but a small deviation in the forced wavenumber was introduced. In the first row, the deviation was $q = .05$ and in the second row $q = .1$. In all cases, the final time was $t = 50$ 97
- 4.16 This figure shows the results of two simulations of Eq. (4.9) with a BCC periodic forcing term. In each case, we used 64^2 grids on a domain of $[-6\pi, 6\pi]^3$. The parameters were $\mu = -.1$ and $\beta = 1.1$. In both cases the forcing strength was $\alpha = 1$. The left panel shows when the forced wavenumber had a mismatch of $q = .05$ while the right panel shows a solution whose forced wavenumber was $q = .1$. In both cases, the solutions are shown at $t = 50$ 98

- 5.1 The PD of an HCP lattice with 216 points, generated by vertices $r(2i + (j + k) \bmod 2, \sqrt{3}(j + (k \bmod 2) - i))$ with $i, j, k = 1, 2, \dots, 6$ and with $r = 1.1$ 102
- 5.2 The top row shows a single instance of a perturbed lattice (orange points) and the corresponding H_1 count distributions over 1,000,000 independent instances. The second row shows the same but for random point clouds. This simulation gives the $E(\#PH_1) \approx .20$ and $\text{var}(\#PH_1) \approx .16$ for perturbed hexagonal lattices and $E(\#PH_1) \approx .04$ and $\text{var}(\#PH_1) \approx .04$ for the random point clouds. Note in both cases, these are Bernoulli distributions. 103
- 5.3 The top row shows a single instance of a perturbed lattice (orange points) and the corresponding H_1 count distributions over 1,000,000 independent instances. The second row shows the same but for random point clouds. This simulation gives the $E(\#PH_1) \approx 107$ and $\text{var}(\#PH_1) \approx 26$ for perturbed hexagonal lattices and $E(\#PH_1) \approx 63$ and $\text{var}(\#PH_1) \approx 26$ for the random point clouds. 104
- 5.4 This figure shows the mean and variance of the H_1 count data over several Monte Carlo simulations. Each simulation had 1,000,000 samples, and increased the size of each configuration, starting with 3 points, and up to 279 points. 105

Chapter 1

Expected Distances on Manifolds of Partially

Oriented Flags ¹

1.1 Introduction

Let V be an n -dimensional vector space. A **flag** in V is a nested sequence of subspaces $V_1 \subset V_2 \subset \dots \subset V_k = V$. If d_i is the dimension of V_i , then associated to the flag is an increasing sequence $d_1 < d_2 < \dots < d_k = n$. We call the sequence (d_1, d_2, \dots, d_k) the **signature** of the flag. For this paper, we will make the assumption that V is a real vector space and the flag manifold $F\ell(d_1, d_2, \dots, d_k)$ will be the real manifold whose points parametrize all flags of signature (d_1, d_2, \dots, d_k) . Flag manifolds are natural generalizations of Grassmann manifolds and have found applications in image analysis [1] and face, pose, and action recognition [2, 3]; as Ye, Wong, and Lim point out [4], they are also implicit in many tasks in numerical and statistical analysis, ranging from mesh refinement to multiresolution analysis to canonical correlation analysis. The key feature of flag manifolds is they locally look the same at each point, i.e. flag manifolds are homogeneous spaces. Homogeneous spaces naturally admit nice coordinates which allow for tangible calculations.

In this paper we generalize the notion of flag manifold, defining **partially oriented flag manifolds**. These manifolds are slight generalizations of the partially oriented flag manifolds introduced by Lam [5] and studied by Sankaran and Zvengrowski [6, 7], among others. Flag manifolds are natural models for data which is properly represented as (nested) subspaces, rather than as individual vectors, and partially oriented flag manifolds should prove useful as models for subspace data when some or all of the nested subspaces are equipped with an orientation. These spaces are rather

¹This project is with Chris Peterson and Clay Shonkwiler. This manuscript was first published in the Proceedings of the AMS.

simple to define as homogeneous spaces, but do not seem to have appeared previously in the data science literature.

Given two data, represented as points in some Riemannian manifold or more general metric space, it is natural to use the distance between the points as a measure of similarity. However, the raw distance is meaningless without further context to know whether the distance is, say, much smaller than expected. A reasonable statistical baseline for such a comparison is the expected distance between two random points in the space. With an eye towards applications of partially oriented flag manifolds to data problems, we determine the expected geodesic distance between random points in all manifolds of partially oriented flags in \mathbb{R}^3 ; compare to Absil, Edelman, and Koev's work using a slightly different notion of distance in Grassmannians [8].

More precisely, recall that $F\ell(1, 2, 3)$ is the manifold of all $(1, 2, 3)$ -flags in \mathbb{R}^3 ; that is, each point represents a line inside a plane inside \mathbb{R}^3 . We will shortly introduce some more involved notation for this space, but for the moment let M be the manifold of such flags in which the line has a preferred orientation, but the plane and \mathbb{R}^3 do not. Then the most interesting expectations we compute are:

Theorem 1. *The expected distance between two random points in M is*

$$\mathbb{E}[d; M] = 1 + \frac{\pi}{4}.$$

The expected distance between random $(1, 2, 3)$ -flags is

$$\mathbb{E}[d; F\ell(1, 2, 3)] = \frac{3\pi}{2} + \frac{96}{\pi^2} \int_0^{\pi/4} \left[\arctan \left(\tan^2 \left(\frac{\arctan(\sec \varphi_3)}{2} \right) \right) - \frac{\arctan^2 \left(\sqrt{1 + \sec^2 \varphi_3} \right)}{\sqrt{1 + \sec^2 \varphi_3}} \right] d\varphi_3 \approx 1.31172503.$$

We define the partially oriented flag manifolds in Section 1.2 and discuss a number of examples and relationships to more familiar manifolds, including Grassmannians, Stiefel manifolds, and

classical flag manifolds. In Section 1.3 we compute the expected distance between two random points in $SO(3)$ both analytically and numerically using Monte Carlo integration. While this computation is not new, it serves as a starting point and template for determining the expected distances between random points in all the manifolds of (partially oriented) flags on \mathbb{R}^3 , which is the focus of Section 1.4.

1.2 Flags and Partially Oriented Flags

Let \mathbb{N} denote the set of all positive integers and let $n \in \mathbb{N}$. An **ordered partition of the integer** n is the tuple $\lambda = (\lambda_1, \dots, \lambda_k)$ with $\lambda_j \in \mathbb{N}$ such that $\sum_{j=1}^k \lambda_j = n$.² In this case, we say the **size** of λ is k . Notice that for an ordered partition of size k , the symmetric group S_k acts by permuting elements; *i.e.* if $\sigma \in S_k$ we define $\sigma \cdot \lambda = (\lambda_{\sigma(1)}, \dots, \lambda_{\sigma(k)})$. Now suppose that $I_\lambda = \{1, \dots, k\}$ is the collection of indices of the partition λ . Then a **partition of the set** I_λ is a collection of disjoint nonempty subsets of I_λ whose union is all of I_λ . We call the partition $\{I_\lambda\}$ the **trivial partition**, and the partition $\{\{1\}, \{2\}, \dots, \{k\}\}$ the **complete partition**. All other partitions of I_λ will be called **proper partitions**.

Let $O(r)$ denote the group of real $r \times r$ orthogonal matrices. For any fixed ordered partition λ of n , define the group $G_\lambda = \prod_{j \in I_\lambda} O(\lambda_j)$. An easy exercise in group theory shows that if $\sigma \in S_k$, then $G_\lambda \cong G_{\sigma \cdot \lambda}$. Since elements of G_λ are of the form $\bigoplus_{j \in I_\lambda} A_j$ where $A_j \in O(\lambda_j)$, we can interpret G_λ as a block-diagonal subgroup of $O(n)$.

Now suppose that $I_\alpha = \{i_1, \dots, i_m\}$ is a subset of I_λ . We define a **special orthogonal block of** G_α to be the set

$$S(O(\lambda_{i_1}) \times \dots \times O(\lambda_{i_m})) = \{A \in G_\alpha \mid \det(A) = 1\}.$$

For brevity of notation, we will denote this set as SG_α . If P is a partition of I_λ , define a **special orthogonal partition of** G_λ to be the group $SG_\lambda^P = \prod_{I_\alpha \in P} SG_\alpha$. If the partition of I_λ is trivial,

²Contrast this with the usual definition of a partition, in which the order does not matter, and hence one can assume $\lambda_1 \geq \lambda_2, \dots, \geq \lambda_k$.

complete, or proper, we call the corresponding special orthogonal partition the same. SG_λ^P is a block-diagonal subgroup of $SO(n)$ which is finite if and only if $\lambda = (1, 1, \dots, 1)$. Since the SG_λ^P are subgroups of $SO(n)$, the quotients will be homogeneous spaces which are the central object of this paper.

Definition 1. Suppose that λ is any ordered partition of the integer n . Then if P is a partition of I_λ , we may define the orbit space $F\ell(\lambda; P) = SO(n)/SG_\lambda^P$. If the partition P is trivial, then $F\ell(\lambda; P)$ is called a **flag manifold**. If P is a complete partition, we say that $F\ell(\lambda; P)$ is an **oriented flag manifold**. Finally, if the partition P is proper, then $F\ell(\lambda; P)$ is called a **partially oriented flag manifold**.

Example 1.2.1. If $\lambda = (k, n - k)$ and $P_T = \{\{1, 2\}\}$ is the trivial partition, then

$$F\ell(\lambda; P_T) = SO(n)/S(O(k) \times O(n - k)) \cong \text{Gr}(k, n),$$

the Grassmannian of k -dimensional linear subspaces of \mathbb{R}^n . If instead we take the complete partition $P_C = \{\{1\}, \{2\}\}$, then

$$F\ell(\lambda; P_C) = SO(n)/(SO(k) \times SO(n - k)) \cong \widetilde{\text{Gr}}(k, n),$$

the oriented Grassmannian of oriented k -dimensional subspaces of \mathbb{R}^n , which double covers $\text{Gr}(k, n)$.

Example 1.2.2. If $1 \leq d_1 < d_2 < \dots < d_k = n$, recall that the flag manifold $F\ell(d_1, \dots, d_k)$ consists of nested subspaces

$$V_1 \subset V_2 \subset \dots \subset V_k = \mathbb{R}^n$$

where $\dim(V_m) = d_m$.

If $\lambda = (\lambda_1, \dots, \lambda_k)$ is an ordered partition of the integer n , define $d_m = \sum_{j=1}^m \lambda_j$ for each $1 \leq m \leq k$. If P_T is the trivial partition of I_λ , then

$$F\ell(\lambda; P_T) = SO(n)/S(O(\lambda_1) \times \dots \times O(\lambda_k)) \cong F\ell(d_1, \dots, d_k)$$

really is a flag manifold. Notice that if $\sigma \in S_k$, then $Fl(\sigma \cdot \lambda; P_T)$ yields a different space parametrizing entirely different geometric objects which is nonetheless diffeomorphic to $Fl(\lambda; P_T)$. This helps explain our use of ordered partitions of n rather than just partitions: we are thinking of the $Fl(\lambda; P)$ spaces as data models, with points corresponding to actual data, so we want to avoid the complication of applying a diffeomorphism before we can think of our data as points in a (partially oriented) flag manifold.

Example 1.2.3. Take $\lambda = (n - k, 1, 1, \dots, 1)$ and suppose that P_C is the complete partition of I_λ . Then

$$Fl(\lambda; P_C) = SO(n)/(SO(n - k) \times SO(1) \times \dots \times SO(1)) \cong SO(n)/SO(n - k) \cong \text{St}(k, n),$$

the Stiefel manifold of orthonormal k -frames in \mathbb{R}^n .

Example 1.2.4. In this example, we'll consider all special orthogonal partitions when $n = 3$ and $\lambda = (1, 1, 1)$. If $P_C = \{\{1\}, \{2\}, \{3\}\}$ is the complete partition of I_λ , then $SG_\lambda^{P_C} = SO(1) \times SO(1) \times SO(1)$ is the trivial group, so $Fl(\lambda; P_C) \cong SO(3)$. At the other extreme, if $P_T = \{\{1, 2, 3\}\}$ is the trivial partition, then $Fl(\lambda; P_T) \cong Fl(1, 2, 3)$ and $SG_\lambda^{P_T} = S(O(1) \times O(1) \times O(1))$ is the copy of the Klein 4-group

$$SG_\lambda^{P_T} = \left\{ \begin{pmatrix} 1 & 0 & 0 \\ 0 & 1 & 0 \\ 0 & 0 & 1 \end{pmatrix}, \begin{pmatrix} -1 & 0 & 0 \\ 0 & -1 & 0 \\ 0 & 0 & 1 \end{pmatrix}, \begin{pmatrix} 1 & 0 & 0 \\ 0 & -1 & 0 \\ 0 & 0 & -1 \end{pmatrix}, \begin{pmatrix} -1 & 0 & 0 \\ 0 & 1 & 0 \\ 0 & 0 & -1 \end{pmatrix} \right\}.$$

If $P_1 = \{\{1\}, \{2, 3\}\}$, $P_2 = \{\{2\}, \{1, 3\}\}$, and $P_3 = \{\{3\}, \{1, 2\}\}$ are proper partitions, then the corresponding groups are

$$SG_\lambda^{P_1} = \left\{ \begin{pmatrix} 1 & 0 & 0 \\ 0 & 1 & 0 \\ 0 & 0 & 1 \end{pmatrix}, \begin{pmatrix} 1 & 0 & 0 \\ 0 & -1 & 0 \\ 0 & 0 & -1 \end{pmatrix} \right\}$$

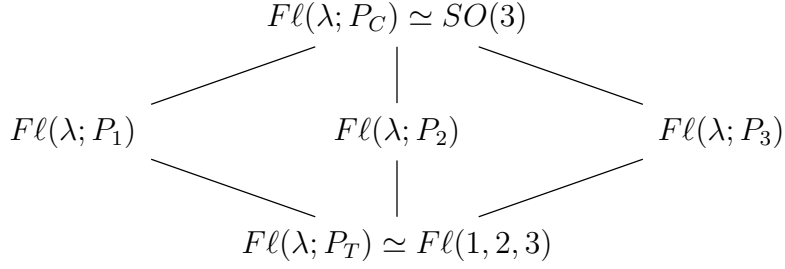


Figure 1.1: Tower of flags for $\lambda = (1, 1, 1)$.

$$SG_{\lambda}^{P_2} = \left\{ \left(\begin{pmatrix} 1 & 0 & 0 \\ 0 & 1 & 0 \\ 0 & 0 & 1 \end{pmatrix}, \begin{pmatrix} -1 & 0 & 0 \\ 0 & 1 & 0 \\ 0 & 0 & -1 \end{pmatrix} \right) \right\}$$

$$SG_{\lambda}^{P_3} = \left\{ \left(\begin{pmatrix} 1 & 0 & 0 \\ 0 & 1 & 0 \\ 0 & 0 & 1 \end{pmatrix}, \begin{pmatrix} -1 & 0 & 0 \\ 0 & -1 & 0 \\ 0 & 0 & 1 \end{pmatrix} \right) \right\}.$$

Clearly each $SG_{\lambda}^{P_i}$ is a subgroup of $SG_{\lambda}^{P_T}$ of index 2, so in the quotients we have natural double covers captured by the tower in Figure 1.1.

The double coverings in the previous example are special cases of a more general phenomenon. Given an ordered partition λ of n and any partition P of I_{λ} , suppose that P' is a refinement of P . Then the number of sets contained in P' and P differ by an integer m . It follows that $|SG_{\lambda}^{P'} : SG_{\lambda}^P| = 2^m$, and hence we have the proposition:

Proposition 2. *Suppose that λ is an ordered partition of n and P is a set partition of I_{λ} . Given any refinement P' of P with $m = |P'| - |P|$, $F\ell(\lambda; P')$ is a 2^m -cover of $F\ell(\lambda; P)$.*

Example 1.2.5. In light of the proposition and Example 1.2.1, we re-verify that $\widetilde{\text{Gr}}(k, n)$ is a double cover of $\text{Gr}(k, n)$.

Since $F\ell(\lambda; P)$ is defined by quotients of orthogonal groups, we can find the total volume of $F\ell(\lambda; P)$. If λ is of length k and $\sigma \in S_k$, we have $\text{Vol}(F\ell(\lambda; P)) = \text{Vol}(F\ell(\sigma \cdot \lambda; \sigma \cdot P))$, so,

for the purposes of computing volume, we may assume that λ is in decreasing order. To simplify notation, let \mathbb{S}^r denote the unit r -sphere and set $V_i = \text{Vol}(\mathbb{S}^{i-1})$ for $i \in \{1, 2, \dots, n\}$; then

$$\text{Vol}(O(m)) = \prod_{i=1}^m V_i,$$

so we see:

Proposition 3. *With notation as above,*

$$\text{Vol}(F\ell(\lambda; P)) = 2^{|P|-1} \frac{V_1 V_2 \cdots V_n}{\prod_{i=1}^{\lambda_1} V_i \cdots \prod_{i=1}^{\lambda_k} V_i} = 2^{|P|-1} \frac{V^{\mathbb{1}}}{V^{\bar{\lambda}}} = 2^{|P|-1} V^{\mathbb{1}-\bar{\lambda}}.$$

In this expression, $\bar{\lambda}$ denotes the conjugate of the partition λ given by taking the Young diagram corresponding to λ , reflecting across the main diagonal, and then taking the partition corresponding to this new diagram; see Figure 1.2 for an example.³ Also, we use the notation $\mathbb{1} := (1, \dots, 1)$ and $x^\mu := x_1^{\mu_1} x_2^{\mu_2} \cdots x_n^{\mu_n}$.

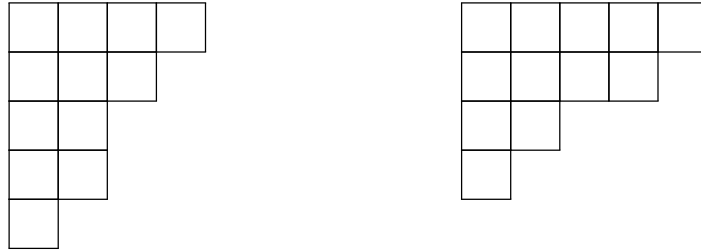


Figure 1.2: On the left is the Young diagram corresponding to the partition $\lambda = (4, 3, 2, 2, 1)$. The conjugate Young diagram is on the right, with corresponding partition $\bar{\lambda} = (5, 4, 2, 1)$.

1.3 $SO(3)$ and Lifts to the 3-Sphere

In this section and the next, we generalize [9] and compute the expected (Riemannian) distance between two random points in a partially oriented flag manifold. We will discuss this computation for all flags for the case $n = 3$. The strategy for each of these computations is similar. The idea is to

³It is in converting the partition λ into a Young diagram that it is important we assume λ is in decreasing order.

lift $SO(3)$ to the unit 3-sphere and carry out computations upstairs. Lifting to \mathbb{S}^3 gives us a natural coordinate system for $SO(3)$ which is then used to describe the Haar measure on $SO(3)$. The push-forward measure is then used to find an invariant measure on each of the flags, and amounts to only changing the region of integration in each case. Additionally, we'll discuss how we can do these calculations via Monte Carlo integration.

1.3.1 Lifting for Analytic Computation

We begin with a known calculation [9] of the expected distance between random points in $SO(3)$. The calculations for partial flags will follow from a refinement of this approach. First we'll briefly describe the Haar measure on $SO(3)$ as parametrized by \mathbb{S}^3 . It is not hard to see that $SO(3)$ is double covered by the unit 3-sphere. Indeed, \mathbb{S}^3 has a natural group structure as the unit quaternions, which act on the quaternions by conjugation. This action clearly fixes the real line since the reals commute with quaternions under multiplication. Hence the purely imaginary quaternions are also invariant under the action of unit quaternions. The restriction of the action to the purely imaginary quaternions is an isometry. To see this, suppose that q is a unit quaternion and that x and y are both purely imaginary quaternions. Then

$$|qxq^{-1} - qyq^{-1}| = |q||x - y||q^{-1}| = |x - y|.$$

By identifying the purely imaginary quaternions with \mathbb{R}^3 , this calculation shows that \mathbb{S}^3 acts by isometries on \mathbb{R}^3 . In fact, this action is by rotations: if $u, n \in \mathbb{R}^3$ are unit vectors, which we interpret as purely imaginary quaternions, and we define $q = \cos \theta + \sin \theta n \in \mathbb{S}^3$, then a straightforward calculation shows that

$$quq^{-1} = (\cos \theta + \sin \theta n)u(\cos \theta - \sin \theta n) = \cos 2\theta u + \sin 2\theta(n \times u) + (1 - \cos 2\theta)(u \cdot n)n, \quad (1.1)$$

which is the Rodrigues formula for rotation of u around the axis n by an angle 2θ . Therefore, \mathbb{S}^3 acts on \mathbb{R}^3 by rotation; moreover, since q and $-q$ both induce the same rotations, it readily follows that $SO(3)$ is double covered by \mathbb{S}^3 .

The double covering of $SO(3)$ provides us a natural way to parametrize $SO(3)$: each element of $SO(3)$ corresponds to an antipodal pair of points in \mathbb{S}^3 , so each rotation corresponds to a (almost always unique) point in the hemisphere of \mathbb{S}^3 where the first coordinate is positive. We can use hyperspherical coordinates on \mathbb{S}^3 to parametrize $SO(3)$:

$$\begin{aligned}x &= \cos \varphi_1 \\y &= \sin \varphi_1 \cos \varphi_2 \\z &= \sin \varphi_1 \sin \varphi_2 \cos \varphi_3 \\w &= \sin \varphi_1 \sin \varphi_2 \sin \varphi_3,\end{aligned}$$

where $\varphi_1 \in [0, \pi/2]$, $\varphi_2 \in [0, \pi]$ and $\varphi_3 \in [0, 2\pi)$. The volume form on \mathbb{S}^3 is

$$\sin^2 \varphi_1 \sin \varphi_2 d\varphi_1 \wedge d\varphi_2 \wedge d\varphi_3,$$

but we need to make a slight adjustment to write down the volume form on $SO(3)$. If $0 \leq \theta \leq \pi/2$ and n is a purely imaginary unit quaternion, then the point $q = \cos \theta + \sin \theta n$ has positive first coordinate and lies at a distance θ from 1 in \mathbb{S}^3 . However, looking at (1.1), the corresponding element of $SO(3)$ is at Frobenius distance 2θ from the identity. Therefore, the map $\mathbb{S}^3 \rightarrow SO(3)$ scales distances by 2 and hence 3-dimensional volumes by $2^3 = 8$, so we conclude that, with respect to hyperspherical coordinates,

$$d\text{Vol}_{SO(3)} = 8 \sin^2 \varphi_1 \sin \varphi_2 d\varphi_1 \wedge d\varphi_2 \wedge d\varphi_3.$$

With this in mind, an easy calculation shows that

$$\text{Vol}(SO(3)) = \int_0^{2\pi} \int_0^\pi \int_0^{\pi/2} 8 \sin^2 \varphi_1 \sin \varphi_2 d\varphi_1 d\varphi_2 d\varphi_3 = 8\pi^2,$$

as expected since the first column lies on the unit 2-sphere, with an area of 4π , the second column lies on a perpendicular unit circle of circumference 2π , and the third column is determined by the first two.

Now, we can compute the expected distance between two random points in $SO(3)$. Since the Frobenius distance is equivariant with respect to the left action of $SO(3)$ on itself, we can rotate one of the two points to the identity and, equivalently, compute the expected distance from a random point in $SO(3)$ to the identity. Equivalently, since an element of $SO(3)$ is a rotation by an angle θ around an axis n , and θ is exactly the Frobenius distance to the identity, we are computing the expected rotation angle of a random element of $SO(3)$.⁴

In order to compute the expected rotation, we note that if $q = \cos \varphi_1 + n \sin \varphi_1$, the angle of rotation is $2\varphi_1$. In other words, up in \mathbb{S}^3 we are computing the expectation of twice the distance φ_1 from a random point in the hemisphere of points with positive real part to the identity element 1:

$$\begin{aligned} \mathbb{E}[d; SO(3)] &= \frac{1}{\text{Vol}(SO(3))} \int_{SO(3)} 2\varphi_1 d\text{Vol}_{SO(3)} \\ &= \frac{2}{\pi^2} \int_0^{2\pi} \int_0^\pi \int_0^{\pi/2} \varphi_1 \sin^2 \varphi_1 \sin \varphi_2 d\varphi_1 d\varphi_2 d\varphi_3 = \frac{2}{\pi} + \frac{\pi}{2}. \end{aligned}$$

This calculation agrees with that found in [9].

1.3.2 Monte Carlo Methods

This computation can also be done numerically using Monte Carlo integration. First, we will describe how to randomly generate matrices in $SO(n)$. With this, we will be able to easily compute

⁴This can also be computed by integrating the rotation angle against the known density of the circular real ensemble [10].

expected distances on $SO(3)$. From here, we will be able to use the same algorithms with slight modifications for similar computations on flag and partially oriented flag manifolds.

Following Chikuse [11], we can generate random orthogonal matrices in Algorithm 1 by applying Gram–Schmidt to a random Gaussian matrix.

Algorithm 1 Random Special Orthogonal Matrix

```

1: function RANDSO( $n$ )
2:    $A \leftarrow$  random  $n \times n$  Gaussian
3:    $Q \leftarrow$  GRAMSCHMIDT( $A$ )
4:   if  $\det(Q) = 1$  then
5:     return  $Q$ 
6:   else  $Q \leftarrow E_{1,2}Q$   $\triangleright E_{1,2}$  is the elementary row swap matrix
7:   return  $Q$ 
8:   end if
9: end function

```

The next algorithm depends on the geodesic distance on $SO(n)$. Fix $A, B \in SO(n)$, and let $AB^T = U\Lambda U^*$ be the spectral decomposition of AB^T . Then because B is an isometry,

$$d(A, B) = d(AB^T, I) = d(U\Lambda U^*, I) = d(U\Lambda, U) = d(\Lambda, I).$$

This means the geodesic distance between A and B depends only on the eigenvalues of AB^T . Thus when approximating the integral via a Monte Carlo algorithm, we only need to generate one random special orthogonal matrix at each step, which reduces computation time significantly.

In fact, the distance $d(A, I)$ is described in [12] and is given by

$$d(A, I) = \left(\frac{1}{2} \sum_{k=1}^n |\log \mu_k|^2 \right)^{1/2}.$$

where μ_k are the eigenvalues of A . The factor of $1/2$ ensures that we aren't overusing $\arg \mu_k$, since the eigenvalues come in complex conjugate pairs. Algorithm 2 describes the Monte Carlo experiment. Using Algorithms 1 and 2 with $n = 3$ and $N = 10,000,000$ gives the approximation

$\mathbb{E}[d; SO(3)] \approx 2.207478465$, with absolute error

$$\left| \frac{2}{\pi} + \frac{\pi}{2} - 2.207478465 \right| \approx 0.000062365.$$

Algorithm 2 Calculating Expected Distance

```

1:  $D \leftarrow [0] * N$  ▷ Begin with a list of  $N$  zeroes
2: for  $i \leftarrow 1, N$  do
3:    $A \leftarrow \text{RANDSO}(n)$ 
4:    $D(i) \leftarrow d(A, I)$ 
5: end for

return MEAN( $D$ )

```

1.4 Expected Distances Between Partially Oriented Flags

Following the example computations on $SO(3)$, we now compute the expected distance between two random points on each (partially oriented) flag manifold $F\ell(\lambda; P)$ obtained from $SO(3)$. In all but one case we'll be able to find an analytic expression for the expectation, and in all cases we'll get a numerical result from a Monte Carlo experiment.

Notice that for λ of length k , $\sigma \in S_k$, and P a partition of I_λ , we have $F\ell(\lambda; P) \cong F\ell(\sigma \cdot \lambda; \sigma \cdot P)$. This is true in general, but in the special case of $SO(3)$ we also observe that if partitions P and P' of I_λ have the same order, then $F\ell(\lambda; P)$ and $F\ell(\lambda; P')$ are diffeomorphic. Combined with the previous fact, we see that $F\ell(\lambda; P) \cong F\ell(\sigma \cdot \lambda; \widehat{P})$ so long as the partitions P of I_λ and \widehat{P} of $I_{\sigma \cdot \lambda}$ are the same size. This reduces the number of computations to be done.

In each case, we can use a trick already mentioned above to simplify our calculations. Since each $F\ell(\lambda; P) = SO(3)/SG_\lambda^P$ is a homogeneous space, and since we will always choose the Riemannian submersion metric on the quotient which is invariant under the left $SO(3)$ action, we can always move one point to the orbit of the identity, and hence the expected distance between two random points in $F\ell(\lambda; P)$ is the same as the expected distance between a single random point and the identity orbit (or any other preferred point).

1.4.1 \mathbb{S}^2 and $\mathbb{R}P^2$

In this section we'll consider the simplest (oriented) flag manifolds derived from $SO(3)$.⁵ Suppose that $\lambda = (1, 2)$. Let $P_C = \{\{1\}, \{2\}\}$ and $P_T = \{\{1, 2\}\}$ denote the complete and trivial partitions of I_λ , respectively. Then we have the identifications $\mathbb{S}^2 \cong Fl(\lambda; P_C)$ and $\mathbb{R}P^2 \cong Fl(\lambda; P_T)$.

Using standard spherical coordinates, the area form on \mathbb{S}^2 is $d\text{Area}_{\mathbb{S}^2} = \sin \varphi d\varphi \wedge d\theta$, where $\varphi \in [0, \pi]$ is the polar angle and $\theta \in [0, 2\pi]$ is the azimuthal angle. Indeed, we verify from the volume formula in Proposition 3 that $\text{Vol}(Fl((1, 2); \{\{1\}, \{2\}\})) = 4\pi$, the area of the unit sphere. Since \mathbb{S}^2 is homogeneous, it suffices to consider the distance between a point and the north pole, which is simply the polar angle φ . Hence we have

$$\mathbb{E}[d; Fl((1, 2); P_C)] = \frac{1}{\text{Area}(\mathbb{S}^2)} \int_{\mathbb{S}^2} \varphi d\text{Area}_{\mathbb{S}^2} = \frac{1}{4\pi} \int_0^{2\pi} \int_0^\pi \varphi \sin \varphi d\varphi d\theta = \frac{\pi}{2}.$$

This is what we expect, since a point is just as likely to be in the northern hemisphere as in the southern. The calculation can also be carried out using Monte Carlo integration: generate a 3-vector v with independent, normally distributed entries. Normalize v to get \hat{v} which is uniformly distributed on the sphere. As above, it suffices to compute the angle between \hat{v} and the north pole. Taking the average of N samples gives the numerical estimate; indeed, an experiment with $N = 10,000,000$ yields the estimate $\mathbb{E}[d; Fl((1, 2); P_C)] \approx 1.570989$, with an absolute error of $|\frac{\pi}{2} - 1.570989| \approx 0.000193$.

The story for $\mathbb{R}P^2$ is similar. The map $\pi : \mathbb{S}^2 \rightarrow \mathbb{R}P^2$ given by $p \mapsto [p] := \{p, -p\}$ is a Riemannian submersion, so the area form on $\mathbb{R}P^2$ is $\pi_* d\text{Area}_{\mathbb{S}^2} = \sin \varphi d\varphi \wedge d\theta$, and computing the distance between points in $\mathbb{R}P^2$ is equivalent to computing the minimum distance between two pairs of antipodal points in \mathbb{S}^2 , so our computation reduces to determining the expected angle

⁵For completeness, we can consider the trivial flag manifold $SO(3)/SO(3)$ which clearly has expected distance 0.

between a random point in the northern hemisphere and the north pole:

$$\mathbb{E}[d; F\ell((1, 2); P_T)] = \frac{1}{\text{Area}(\mathbb{RP}^2)} \int_{\mathbb{RP}^2} \varphi \, d\text{Area}_{\mathbb{RP}^2} = \frac{1}{2\pi} \int_0^{2\pi} \int_0^{\pi/2} \varphi \sin \varphi \, d\varphi d\theta = 1.$$

To carry this out with Monte Carlo methods, take \hat{v} as before, but compute the average of $\arccos |\hat{v} \cdot e_3|$ where e_3 is the point at the north pole. An experiment with $N = 10,000,000$ produces the estimate $\mathbb{E}[d; F\ell((1, 2); P_T)] \approx 0.999975$.

1.4.2 Flags with $\lambda = (1, 1, 1)$

In this section we consider flags with the ordered partition $\lambda = (1, 1, 1)$. First we'll describe the problem of finding expected distances via Monte Carlo integration. Following this, we'll take a look at each individual case. Suppose that P is any partition of I_λ . In this case SG_λ^P contains only a finite number of elements in $SO(3)$ as we have already seen in Example 1.2.4. Computing the expected distance on $SO(3)/SG_\lambda^P$ is hardly any different from what we've done before: we simply take the minimum distance from each point in the orbit gSG_λ^P to the identity as in Algorithm 3.

Algorithm 3 Expected Distance on $SO(3)/SG_\lambda^P$

```

1:  $D \leftarrow [0] * N$  ▷ Begin with a list of  $N$  zeroes
2: for  $i \leftarrow 1, N$  do
3:    $A \leftarrow \text{RANDSO}(3)$ 
4:    $\text{orbitdata} \leftarrow [0] * |SG_\lambda^P|$  ▷  $|SG_\lambda^P|$  denotes the order of  $SG_\lambda^P$ 
5:   for  $j \leftarrow 1, |SG_\lambda^P|$  do
6:      $\text{orbitdata}(j) \leftarrow d(Ah_j, I)$  ▷ Each  $h_j$  denotes a distinct element of  $SG_\lambda^P$ 
7:   end for
8:    $D(i) \leftarrow \text{MIN}(\text{orbitdata})$ 
9: end for

return  $\text{MEAN}(D)$ 

```

Oriented Flags

When $P = P_C$ is the complete partition, the oriented flag manifold $F\ell(\lambda; P) \cong SO(3)$ and we saw in Section 1.3.1 that the expected distance between two random points in this space is

$$\mathbb{E}[d; F\ell((1, 1, 1); P_C)] = E[d; SO(3)] = \frac{2}{\pi} + \frac{\pi}{2}.$$

Partially Oriented Flags

For the case of the partially oriented flags we may choose P to be P_1, P_2 , or P_3 as in Example 1.2.4. In any case, SG_λ^P will contain two matrices. Without loss of generality, suppose that $P = P_1$. We can readily apply Algorithm 3 with $N = 10,000,000$ to see that the expected distance is ≈ 1.78548266 .

To get an analytic expression, the strategy is to lift the computation to \mathbb{S}^3 as in Section 1.3. Since the composite map $\mathbb{S}^3 \rightarrow SO(3) \rightarrow SO(3)/SG_\lambda^P$ is (up to the scale factor 2) a Riemannian submersion, the distance between a pair of points in $F\ell(\lambda; P) = SO(3)/SG_\lambda^P$ is equal to twice the minimum distance between the sets of preimages in \mathbb{S}^3 .

As usual, the expected distance between two random points in $F\ell(\lambda; P)$ is the same as the expected distance between a single random point and any preferred point, which we will take to be the identity coset ISG_λ^P . In turn, the identity coset consists of the identity and the rotation by angle π around the axis $(1, 0, 0)$, so its preimages in \mathbb{S}^3 are $\{1, -1, i, -i\}$; in general, if $g \in SO(3)$ is rotation by θ around an axis n , then the preimage of gSG_λ^P in \mathbb{S}^3 is $\{q, -q, iq, -iq\}$, where $q = \cos \frac{\theta}{2} + \sin \frac{\theta}{2}n$. In turn, since multiplication by -1 and multiplication by i are isometries,

$$d(\{1, -1, i, -i\}, \{q, -q, iq, -iq\}) = d(1, \{q, -q, iq, -iq\}),$$

where the minimum distance will be achieved by the element of $\{q, -q, iq, -iq\}$ which is closer to 1 than to $-1, i$, or $-i$.

Therefore, the expected distance between a random coset gSG_λ^P and the identity coset (and hence, between two random points in $F\ell(\lambda; P)$), is simply the expectation of twice the distance

from 1 to a random point in the subset of \mathbb{S}^3 which is closer to 1 than to -1 , i , or $-i$. In terms of Cartesian coordinates (x, y, z, w) , this is precisely the set $\{(x, y, z, w) : x \geq |y|\}$; in hyperspherical coordinates, $x \geq |y|$ is equivalent to $0 \leq \phi_1 \leq \arctan(\sec \phi_2)$.

Hence, the volume of the partial flag is given by

$$\begin{aligned} \text{Vol}(Fl(\lambda; P)) &= \int_{Fl(\lambda; P)} d\text{Vol}_{Fl(\lambda; P)} = \int_0^{2\pi} \int_0^\pi \int_0^{\arctan(\sec \varphi_2)} 8 \sin^2 \varphi_1 \sin \varphi_2 d\varphi_1 d\varphi_2 d\varphi_3 \\ &= 2 \int_0^{2\pi} \int_0^{\pi/2} \int_0^{\arctan(\sec \varphi_2)} 8 \sin^2 \varphi_1 \sin \varphi_2 d\varphi_1 d\varphi_2 d\varphi_3, \end{aligned}$$

where we use symmetry to restrict to $\varphi_2 \in [0, \pi/2)$ and avoid any issues with $\arctan(\sec \varphi_2)$.

Mathematica will happily compute the above integral to be $4\pi^2$, which agrees with the volume calculation from Proposition 3, but the limits of integration on the innermost integral make this unpleasant to compute by hand.

We can make things easier by changing coordinate systems. Thinking of \mathbb{S}^3 as the unit sphere in \mathbb{C}^2 , we will interpret points on \mathbb{S}^3 as pairs $(z_1, z_2) \in \mathbb{C}^2$ with $|z_1|^2 + |z_2|^2 = 1$. Then the condition $x > |y|$ is equivalent to $|\arg z_1| < \frac{\pi}{4}$ – which will be a lens-shaped region in \mathbb{S}^3 ; the analogous region on \mathbb{S}^2 is a lune – so it is desirable to use $\arg z_1$ as one of our coordinates. In fact, $|z_1|^2 + |z_2|^2 = 1$ means that

$$(z_1, z_2) = (\cos \alpha e^{i\theta_1}, \sin \alpha e^{i\theta_2})$$

for $\alpha \in [0, \pi/2]$ and $\theta_1, \theta_2 \in [0, 2\pi]$. Notice that each value of α determines a torus in \mathbb{S}^3 except the extremal values $\alpha = 0$ and $\alpha = \pi/2$, where the torus collapses to the unit circle in the z_1 - or z_2 -plane. See Figure 1.3 for a visualization.

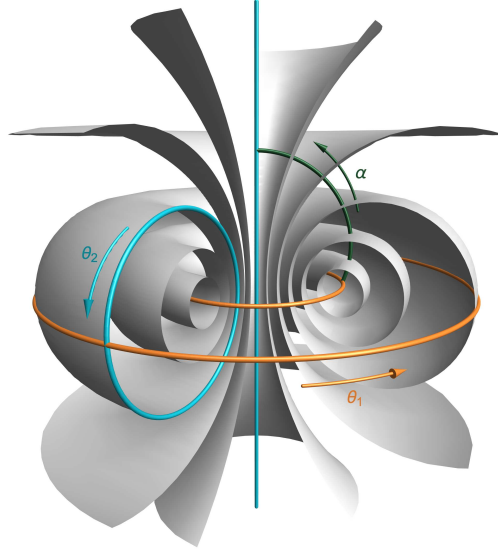


Figure 1.3: Stereographic projection to \mathbb{R}^3 of join coordinates on \mathbb{S}^3 . θ_1 and θ_2 are simply the arguments of the two complex coordinates, while α gives the angle a given vector makes with the z_1 -plane. The level sets of α are generically tori, collapsing to the unit circle in the z_1 -plane when $\alpha = 0$ and to the unit circle in the z_2 -plane (which stereographically projects to the z -axis) when $\alpha = \pi/2$.

We can write these coordinates – which we call **join coordinates** because they give a concrete realization of \mathbb{S}^3 as the topological join of two copies of \mathbb{S}^1 – in terms of Cartesian coordinates as

$$x = \cos \alpha \cos \theta_1$$

$$y = \cos \alpha \sin \theta_1$$

$$z = \sin \alpha \cos \theta_2$$

$$w = \sin \alpha \sin \theta_2$$

and the volume form on \mathbb{S}^3 is easily computed to be $d\text{Vol}_{\mathbb{S}^3} = \cos \alpha \sin \alpha d\alpha \wedge d\theta_1 \wedge d\theta_2$. In these coordinates, the volume of $F\ell(\lambda; P)$ is easy to compute by hand, as it reduces to a simple u -substitution:

$$\text{Vol}(F\ell(\lambda; P)) = \int_0^{2\pi} \int_{-\pi/4}^{\pi/4} \int_0^{\pi/2} 8 \cos \alpha \sin \alpha d\alpha d\theta_1 d\theta_2 = 4\pi^2$$

We want to compute the expectation of twice the spherical distance from 1 to a random point in the region $-\frac{\pi}{4} < \theta_1 < \frac{\pi}{4}$. The distance is simply $\arccos(\cos \alpha \cos \theta_1)$, and so the expected distance between two random points in $F\ell(\lambda; P)$ is

$$\begin{aligned} \frac{1}{\text{Vol}(F\ell(\lambda; P))} & \int_{-\pi}^{\pi} \int_{-\pi/4}^{\pi/4} \int_0^{\pi/2} 2 \arccos(\cos \alpha \cos \theta_1) 8 \cos \alpha \sin \alpha \, d\alpha \, d\theta_1 \, d\theta_2 \\ &= \frac{4}{\pi^2} \int_{-\pi}^{\pi} \int_{-\pi/4}^{\pi/4} \int_0^{\pi/2} \arccos(\cos \alpha \cos \theta_1) \cos \alpha \sin \alpha \, d\alpha \, d\theta_1 \, d\theta_2 \\ &= \frac{16}{\pi} \int_0^{\pi/4} \int_0^{\pi/2} \arccos(\cos \alpha \cos \theta_1) \cos \alpha \sin \alpha \, d\alpha \, d\theta_1 \end{aligned}$$

by integrating out θ_2 and using the fact that the integrand is even in θ_1 .

This is slightly tedious but essentially straightforward to compute using the substitutions $u = \cos \alpha$ and $\sin v = u \cos \theta_1$, producing the first half of Theorem 1, which we restate in slightly more general form:

Theorem 4. *For $i = 1, 2, 3$, the expected distance between two random points in $F\ell((1, 1, 1); P_i)$ is*

$$\mathbb{E}[d; F\ell((1, 1, 1); P_i)] = 1 + \frac{\pi}{4}.$$

Note that

$$\left| 1 + \frac{\pi}{4} - 1.78548266 \right| \approx 0.0000844966$$

which once again shows that our Monte Carlo experiment does a good job of approximating the analytic result.

Flags

Finally, we consider the case when P is the trivial partition, so SG_{λ}^P contains four matrices as in Example 1.2.4 and $F\ell(\lambda; P) \cong F\ell(1, 2, 3)$, the manifold of (complete) flags on \mathbb{R}^3 . We may readily apply Algorithm 3 with $N = 10,000,000$ to find that the expected distance between two random points in $F\ell(1, 2, 3)$ is ≈ 1.311751687 .

Finding an explicit integral for this calculation only requires a few additional changes to the bounds from the previous section. The orbit of the identity lifts to $\{\pm 1, \pm i, \pm j, \pm k\}$, which are the vertices of the regular 16-cell dual to the standard hypercube. Other orbits are simply rotated copies of the orbit of the identity, so they also get lifted to regular 16-cells. Hence, computing the expected distance between points in $F\ell(1, 2, 3)$ is equivalent to computing the expected distance from 1 to all the other unit quaternions which are closer to 1 than any of the other integer points on \mathbb{S}^3 .

This set is nothing but the radial projection of the cube

$$\{(x, y, z, w) : x = 1, -1 \leq |y|, |z|, |w| \leq 1\}$$

to \mathbb{S}^3 , namely those points with $x \geq |y|$, $x \geq |z|$, and $x \geq |w|$. This spherical cube is partitioned into $3! \times 2^3$ spherical tetrahedra, each congruent to the spherical tetrahedron $x \geq y \geq z \geq w \geq 0$. To integrate over this tetrahedron in hyperspherical coordinates we get the limits of integration $\varphi_1 \in [0, \arctan(\sec \varphi_2)]$, $\varphi_2 \in [0, \arctan(\sec \varphi_3)]$, and $\varphi_3 \in [0, \pi/4]$. Since the simplex is $\frac{1}{48}$ of the full spherical cube, we see that

$$\text{Vol}(F\ell(1, 2, 3)) = 48 \int_0^{\pi/4} \int_0^{\arctan(\sec(\varphi_3))} \int_0^{\arctan(\sec(\varphi_2))} 8 \sin^2 \varphi_1 \sin \varphi_2 d\varphi_1 d\varphi_2 d\varphi_3;$$

using *Mathematica's* numerical integration algorithm reassuringly yields a number numerically indistinguishable from $2\pi^2$, which we know from Proposition 3 is the true volume.

Therefore, the expected distance between two points on $F\ell(1, 2, 3)$ is given by the integral

$$\frac{48}{2\pi^2} \int_0^{\pi/4} \int_0^{\arctan(\sec(\varphi_3))} \int_0^{\arctan(\sec(\varphi_2))} 2\varphi_1 8 \sin^2 \varphi_1 \sin \varphi_2 d\varphi_1 d\varphi_2 d\varphi_3.$$

In join coordinates, the corresponding integral turns out to be

$$\frac{4}{2\pi^2} \int_{-\pi/4}^{\pi/4} \int_{-\pi/4}^{\pi/4} \int_0^{\arctan\left(\frac{\cos \theta_1}{\cos \theta_2}\right)} 2 \arccos(\cos \alpha \cos \theta_1) 8 \cos \alpha \sin \alpha d\alpha d\theta_1 d\theta_2.$$

It is not clear how to evaluate either of these integrals exactly, though the former can be reduced to the one-dimensional integral given in the second half of Theorem 1, which we restate:

Theorem 5. *The expected distance between two random $(1, 2, 3)$ -flags is*

$$\mathbb{E}[d; F\ell(1, 2, 3)] = \frac{3\pi}{2} + \frac{96}{\pi^2} \int_0^{\pi/4} \left[\arctan \left(\tan^2 \left(\frac{\arctan(\sec \varphi_3)}{2} \right) \right) - \frac{\arctan^2 \left(\sqrt{1 + \sec^2 \varphi_3} \right)}{\sqrt{1 + \sec^2 \varphi_3}} \right] d\varphi_3.$$

Of course, this can be numerically evaluated to an arbitrary degree of precision; to 20 digits, we can compute that the expected distance between two random points in $F\ell(1, 2, 3)$ is 1.3117250347224445929. Using the PSLQ algorithm [13], this does not appear to be in the vector space over \mathbb{Q} generated by 1, π , and $\frac{1}{\pi}$, unlike all the other expected values we have computed.

1.5 Conclusion and Open Questions

The manifolds of partially oriented flags described in this paper have the potential to be a natural home for data which is interpretable in terms of nested subspaces, of which some may be oriented. We encourage mathematicians, engineers, and other practitioners who are beginning to see the usefulness of flag manifolds in data analysis to keep these spaces in mind.

While partially oriented flag manifolds have been studied by algebraic topologists [5–7], we have not been able to find much evidence of their being studied by geometers. Given the fundamental role played by flag varieties in algebraic geometry, it would be interesting to find a more algebraic definition or interpretation of these spaces. We also look forward to further geometric computation on these spaces, whether it be computing expected distances on a larger class of partially oriented flag manifolds or determining other geometric quantities of interest.

For data living in a metric space, the expected distance between two random points in that space is a simple statistical baseline for distance-based similarity measures. While this quantity can often be estimated effectively using Monte Carlo techniques, it would be interesting to see

analytic expressions for expected distance on spaces which are nice geometrically or useful as data models.

Chapter 2

Distributions of Distances and Volumes of Balls in Homogeneous Lens Spaces⁶

2.1 Introduction

Given a set of data, what is the best guess for the random process that produced the data? Attempts to answer special cases of this question have motivated new developments in statistics, mathematics, and machine learning. As a starting point, one would like to understand whether the observed data has a distribution differing from what is “expected.” However, determining what is expected can be quite subtle when the data takes values on a manifold, though when the manifold is homogeneous, there are additional tools that one can use to simplify the problem. At an intuitive level, a homogeneous manifold is a space in which each point is indistinguishable from any other point.

For distance data, one would ideally like to check whether the distribution of pairwise distances is compatible with the corresponding distribution on the manifold. In a previous paper [14], we considered the problem of computing the expected distances between randomly drawn points on manifolds of partially oriented flags. These manifolds generalize projective spaces and other Grassmannians and form a large family of homogeneous spaces. The examples in which we had the most success computing expected distances turn out to be (scaled) lens spaces; that is, quotients of an odd-dimensional sphere by the free action of a cyclic group. In this paper we go beyond simple expectations and determine precisely the distributions of distances between pairs of random points in all homogeneous three-dimensional lens spaces.

These distributions are examples of *distance distributions* (or sometimes *shape distributions* or *distance histograms*), which make sense on arbitrary metric measure spaces, and are often used

⁶This project is with Chris Peterson and Clay Shonkwiler. This manuscript was first published in *Differential Geometry and its Applications*.

for geometric classification and shape analysis [15–21]. Our results provide a strong statistical baseline against which to compare data on lens spaces, which have recently been applied to data science [22], appear frequently in the cosmography literature [23–26], and are the natural setting for spherical data with cyclic symmetries.

To establish notation, each pair of positive integers (n, m) with $n > m$ and $\gcd(n, m) = 1$ determines a three-dimensional lens space $L(n; m)$ which is a quotient of the 3-sphere \mathbb{S}^3 by the cyclic group of order n . By requiring the quotient to be a Riemannian submersion, we induce a Riemannian metric on $L(n; m)$, which turns out to be homogeneous when $m = 1$ or $n - 1$. Moreover, $L(n; 1)$ and $L(n; n - 1)$ are isometric, so to understand distance distributions on homogeneous lens spaces it suffices to consider those lens spaces of the form $L(n; 1)$.

As a first step, we determine all moments of distance (i.e., expected values of powers of distance) by solving a recurrence relation that they satisfy:

Theorem 6. *For each $k \geq 0$ and each $n \geq 2$, the k th moment of distance on $L(n; 1)$ is*

$$I_{n,k} = \frac{1}{(k+1)(k+2)} \left[\frac{4}{k+3} \left(\frac{\pi}{n}\right)^{k+2} {}_1F_2 \left[\frac{1}{\frac{k+4}{2}, \frac{k+5}{2}}; -\frac{\pi^2}{n^2} \right] + \tan \frac{\pi}{n} \left(n \left(\frac{\pi}{2}\right)^{k+1} {}_1F_2 \left[\frac{1}{\frac{k+3}{2}, \frac{k+4}{2}}; -\frac{\pi^2}{4} \right] - 2 \left(\frac{\pi}{n}\right)^{k+1} {}_1F_2 \left[\frac{1}{\frac{k+3}{2}, \frac{k+4}{2}}; -\frac{\pi^2}{n^2} \right] \right) \right],$$

where for $n = 2$ this is interpreted as the limit of the above expression as $n \rightarrow 2$, and ${}_1F_2$ is a hypergeometric function whose definition we recall on page 33 below.

The alternating finite sum formula given in (2.8) is typically more useful for small k , but one virtue of this formulation in terms of hypergeometric functions is that it is easy to extract asymptotic information:

Corollary 7. *As $k \rightarrow \infty$ the k th moment of distance grows like*

$$I_{2,k} \sim \frac{2}{k} \left(\frac{\pi}{2}\right)^k \quad \text{and} \quad I_{n,k} \sim \frac{n}{k^2} \left(\frac{\pi}{2}\right)^{k+1} \tan \frac{\pi}{n} \quad \text{for } n \geq 3.$$

A more attractive and systematic packaging of the moments is in the form of the moment-generating function of distance:

Theorem 8. *The moment-generating function of distance on $L(n; 1)$ is*

$$M_n(t) = \begin{cases} \frac{4}{\pi(4+t^2)} \left(\frac{2(e^{t\pi/2}-1)}{t} + te^{t\pi/2} \right) & \text{if } n = 2 \\ \frac{2n}{\pi(4+t^2)} \left(\frac{2(e^{t\pi/n}-1)}{t} + \tan \frac{\pi}{n} (e^{t\pi/2} - e^{t\pi/n}) \right) & \text{if } n \geq 3. \end{cases}$$

We then use the moment-generating function to determine the cumulative distribution function of distance, which (up to scaling) simply reports volumes of balls. Consequently, our probabilistic approach to studying distances on lens spaces yields the following purely geometric result:

Theorem 9. *For $n \geq 2$, the volume of a ball of radius r in $L(n; 1)$ is*

$$V_n(r) = \begin{cases} 2\pi(r - \sin r \cos r) & \text{if } r \leq \frac{\pi}{n} \\ \frac{2\pi^2}{n} - 2\pi \cos^2 r \tan \frac{\pi}{n} & \frac{\pi}{n} < r < \frac{\pi}{2} \\ \frac{\pi}{2} & r \geq \pi/2 \end{cases}$$

Notice, in particular, that this formula for volume extends beyond the injectivity radius $\frac{\pi}{n}$ of $L(n; 1)$, in contrast to most results about volumes of balls in Riemannian manifolds (e.g., [27]). In addition to the potential applications of these ideas to data problems, this seems to be a novel result to add to existing knowledge about the geometry and topology of lens spaces [28–36].

We describe our perspective, provide basic background material on lens spaces, and give the setting in which algorithms and analytic computations are to be made in Section 2.2. In Section 2.3 we describe algorithms for sampling random points and determining their distance apart. In addition, we present the results of several Monte Carlo experiments that illustrate differences between distributions of distances on homogeneous and non-homogeneous lens spaces. Section 2.4 contains the main theoretical results of the paper.

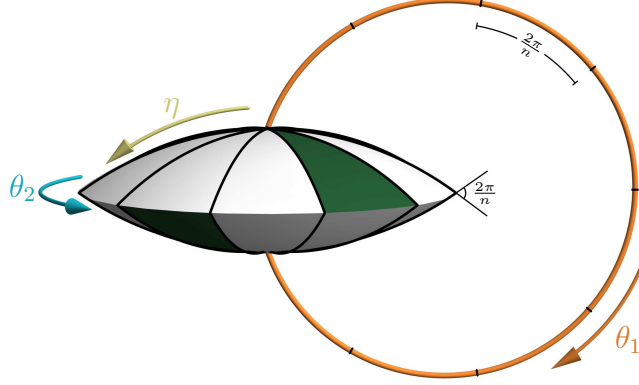


Figure 2.1: A fundamental domain of the lens space $L(n; m)$. The arrows indicate the directions of the joint coordinates $(\theta_1, \theta_2, \eta)$ that will be defined on page 27.

2.2 Lens Spaces

Three-dimensional lens spaces are a family of manifolds that arise as the orbit space of a finite cyclic group acting freely on the unit 3-sphere. More precisely, let $Z_n = \{e^{i2\pi k/n} \in \mathbb{C} \mid 1 \leq k \leq n\}$ denote the cyclic group of order n and consider $\mathbb{S}^3 = \{(\alpha, \beta) \in \mathbb{C}^2 \mid |\alpha|^2 + |\beta|^2 = 1\}$. Given $n, m \in \mathbb{N}$ with $\gcd(m, n) = 1$, there is a free action of Z_n on \mathbb{S}^3 defined by

$$\omega \cdot (\alpha, \beta) = (\omega\alpha, \omega^m\beta),$$

for each $\omega \in Z_n$. The resulting orbit space is the lens space $L(n; m)$.

To visualize $L(n; m)$, we can look at the fundamental domain of the Z_n action on $\mathbb{S}^3 \subseteq \mathbb{C}^2$, as in Figure 2.1. The fundamental domain of the rotation $e^{2\pi i/n}$ in the first factor is an arc of length $\frac{2\pi}{n}$ in the unit circle in the z_1 -plane of \mathbb{C}^2 . All points in \mathbb{S}^3 with first coordinate in such a fundamental domain form a lens-shaped domain as pictured. The top and bottom faces of the lens consist of all points lying on geodesics connecting an endpoint of the arc to all points in the unit circle in the z_2 -plane: these are hemispheres of unit 2-spheres meeting at an angle of $\frac{2\pi}{n}$ along the unit circle in the z_2 -plane. Since the endpoints of the arc are identified under the $\frac{2\pi}{n}$ rotation in the z_1 -coordinate, the bottom face is identified with the top face by this rotation. However, this identification happens with a $\frac{2\pi m}{n}$ twist in the z_2 -coordinate, so that the green sector in the bottom face is glued to the green sector in the top face (in the picture, $m = 2$).

Lens spaces were introduced by Tietze [37] and have historically provided interesting examples of manifolds which cannot be distinguished by homology or homotopy groups. For example, $L(5; 1)$ and $L(5; 2)$ are not homeomorphic (nor even homotopy equivalent) despite the fact that $\pi_1(L(5; 1)) \cong \pi_1(L(5; 2))$ and $H_\bullet(L(5; 1)) \cong H_\bullet(L(5; 2))$ [28]. In fact, the lens spaces $L(n; m_1)$ and $L(n; m_2)$ are homotopy equivalent if and only if $m_1 m_2 = \pm a^2 \pmod{n}$ for some $a \in \mathbb{N}$, and are homeomorphic if and only if $m_1 = \pm m_2^{\pm 1} \pmod{n}$ [29, 33]. Using these criteria, one can easily conclude that $L(7; 1)$ and $L(7; 2)$ are examples of manifolds which are homotopy equivalent but not homeomorphic.

In addition to their topological structure, lens spaces have geometric structure. The round metric on \mathbb{S}^3 induces a unique metric on $\mathbb{S}^3/Z_n = L(n; m)$ that makes $\pi : \mathbb{S}^3 \rightarrow L(n; m)$ a Riemannian submersion. A result of Ikeda and Yamamoto [30] implies that two three-dimensional lens spaces are isometric if and only if they are homeomorphic. This result, combined with work of Tanaka [35], shows that the spectrum of the Laplacian uniquely determines a three-dimensional lens space among all Riemannian manifolds. An explicit orthonormal eigenbasis for the Laplacian is given in [31]. Moreover, the isoperimetric problem has been solved in all lens spaces $L(n; m)$ with n large enough [36].

With respect to this Riemannian metric, some lens spaces are homogeneous, meaning the isometry group acts transitively. Theorem 7.6.6 of Wolf [38] says that \mathbb{S}^d/G is homogeneous if and only if the group G has a *Clifford representation*—that is, a faithful orthogonal representation $\rho : G \rightarrow O(d+1)$ such that $\rho(g) = \pm I$ or half of the eigenvalues of $\rho(g)$ are $\lambda \in \mathbb{S}^1$ and the other half are $\bar{\lambda}$. The action of Z_n on \mathbb{S}^3 has the faithful orthogonal representation $\rho : Z_n \rightarrow O(4)$ given by

$$\rho(\omega) = \begin{pmatrix} \cos 2\pi/n & -\sin 2\pi/n & 0 & 0 \\ \sin 2\pi/n & \cos 2\pi/n & 0 & 0 \\ 0 & 0 & \cos 2\pi m/n & -\sin 2\pi m/n \\ 0 & 0 & \sin 2\pi m/n & \cos 2\pi m/n \end{pmatrix},$$

and has eigenvalues $e^{i2\pi/n}, e^{-i2\pi/n}, e^{i2\pi m/n}$ and $e^{-i2\pi m/n}$. Hence $L(n; m)$ is homogeneous precisely when $m = 1$ or $m = n - 1$. Since $L(n; 1)$ and $L(n; n - 1)$ are homeomorphic and hence isometric, we may simply take $m = 1$ when dealing with homogeneous lens spaces.

2.2.1 Coordinate systems

Using the natural group structure on \mathbb{S}^3 given by its identification with the unit quaternions, we can describe an isomorphism between \mathbb{S}^3 and $SU(2)$. Writing quaternions in the form $\alpha + \beta\mathbf{j}$ for $\alpha, \beta \in \mathbb{C}$, define $\varphi : \mathbb{S}^3 \rightarrow SU(2)$ by

$$\varphi : \alpha + \beta\mathbf{j} \mapsto \begin{pmatrix} \alpha & -\beta \\ \bar{\beta} & \bar{\alpha} \end{pmatrix},$$

where $\bar{\zeta}$ denotes the complex conjugate of ζ . It is easy to check that φ is a Lie group isomorphism. The action of Z_n on \mathbb{S}^3 then induces an action on $SU(2)$ given explicitly by

$$\omega \cdot \begin{pmatrix} \alpha & -\beta \\ \bar{\beta} & \bar{\alpha} \end{pmatrix} = \begin{pmatrix} \omega\alpha & -\omega^m\beta \\ \overline{\omega^m\beta} & \overline{\omega\alpha} \end{pmatrix}. \quad (2.1)$$

Describing the lens space in this way will make our computations straightforward. The idea is that we can easily generate random elements of $SU(2)$ according to Haar measure (which corresponds to the uniform probability measure on \mathbb{S}^3), compute the orbits explicitly, and then distances between orbits correspond to distances in the lens space.

For homogeneous lens spaces, we will be able to make explicit analytic calculations in Section 2.4. To do so, we'll parametrize \mathbb{S}^3 using *join coordinates*, which realize the 3-sphere as the join of two circles. Since $\mathbb{S}^3 = \{(\alpha, \beta) \in \mathbb{C}^2 \mid |\alpha|^2 + |\beta|^2 = 1\}$, we can write $\alpha = e^{i\theta_1} \cos \eta$ and $\beta = e^{i\theta_2} \sin \eta$ for $\theta_1, \theta_2 \in [-\pi, \pi)$ and $\eta \in [0, \pi/2]$. This can also be expressed in Cartesian

coordinates on \mathbb{R}^4 as

$$\begin{aligned}
 x &= \cos \theta_1 \cos \eta \\
 y &= \sin \theta_1 \cos \eta \\
 z &= \cos \theta_2 \sin \eta \\
 w &= \sin \theta_2 \sin \eta.
 \end{aligned}
 \tag{2.2}$$

These coordinates easily yield the volume form $d\text{Vol}_{\mathbb{S}^3} = \cos \eta \sin \eta d\eta \wedge d\theta_1 \wedge d\theta_2$, and the volume form induced by the Riemannian submersion metric on the homogeneous lens space $L(n; 1)$ is $d\text{Vol}_{L(n;1)} = \cos \eta \sin \eta d\eta \wedge d\theta_1 \wedge d\theta_2$, where now $\theta_1, \theta_2 \in [-\pi/n, \pi/n)$. A straightforward calculation shows that $\text{Vol}(L(n; 1)) = 2\pi^2/n^2$.

2.3 Algorithms and Experiments

In this section we'll provide an algorithm for a Monte Carlo experiment. We then use this as a guide for analysis on higher moments.

Our aim is to describe a Monte Carlo simulation which will allow us to approximate expected (Riemannian) distances between two points in $L(n; m)$. We will use Algorithm 4 to randomly generate elements of $SU(n)$.

Algorithm 4 Random Special Unitary Matrix

- 1: **function** RANDSU(n)
 - 2: $A, B \leftarrow$ random $n \times n$ Gaussian
 - 3: $C \leftarrow A + iB$ \triangleright where $i = \sqrt{-1}$
 - 4: $Q \leftarrow$ GRAMSCHMIDT(C)
 - 5: $Q_{1,n} \leftarrow \frac{1}{\det(Q)} Q_{1,n}$ $\triangleright Q_{1,n}$ is the last column of Q
 - 6: **end function**
-

We will use the Riemannian distance function on $SU(2)$ (see [39]), then use the Riemannian submersion $\pi : SU(2) \rightarrow L(n; m)$ to obtain a distance function on the lens space. Suppose that $A, B \in SU(2)$, and let λ_1, λ_2 be the eigenvalues of AB^* . For a nonzero complex number

$z = x + yi$, we let $\log z$ denote the principal value logarithm whose imaginary part lies in the interval $(-\pi, \pi]$. The geodesic distance in $SU(2)$ is given by

$$d(A, B) = \frac{1}{\sqrt{2}} \sqrt{|\log \lambda_1|^2 + |\log \lambda_2|^2}$$

or, since $\lambda_2 = \bar{\lambda}_1$, $d(A, B) = |\log \lambda_1|$. To compute distances on $L(n; m)$, we first compute the orbits, then compute pairwise distances between the elements of each orbit, and finally take the minimum of all distances computed. Thus for $[A], [B] \in L(n; m)$, we have

$$d([A], [B]) = \min_{1 \leq j, k \leq n} \{d(\omega^j \cdot A, \omega^k \cdot B)\},$$

where $\omega = e^{2\pi i/n}$. This leads to Algorithm 5.

Algorithm 5 Expected Distance on $L(n; m)$

```

1:  $D \leftarrow [0] * N$  ▷ Begin with a list of  $N$  zeroes
2: for  $k \leftarrow 1, N$  do
3:    $A \leftarrow \text{RANDSU}(2)$ 
4:    $B \leftarrow \text{RANDSU}(2)$ 
5:    $\text{orbitdata} \leftarrow [0] * n \times n$  ▷ Initialize  $n \times n$  zero matrix
6:   for  $i \leftarrow 1, n$  do
7:     for  $j \leftarrow 1, n$  do
8:        $\text{orbitdata}(i, j) \leftarrow d(\omega^i \cdot A, \omega^j \cdot B)$ 
9:     end for
10:  end for
11:   $D(k) \leftarrow \text{MIN}(\text{orbitdata})$ 
12: end for

return  $\text{MEAN}(D)$ 

```

For example, using Algorithm 5 with $N = 1,000,000$, we estimate the expected distances between random points on $L(5; 1)$ and $L(5; 2)$ to be approximately 0.85897 and 0.80378, respectively, reflecting the fact that these lens spaces are not isometric (nor even homeomorphic); see Figure 2.2. The corresponding estimates for $L(7; 1)$ and $L(7; 2)$ are 0.82641 and 0.73641, respec-

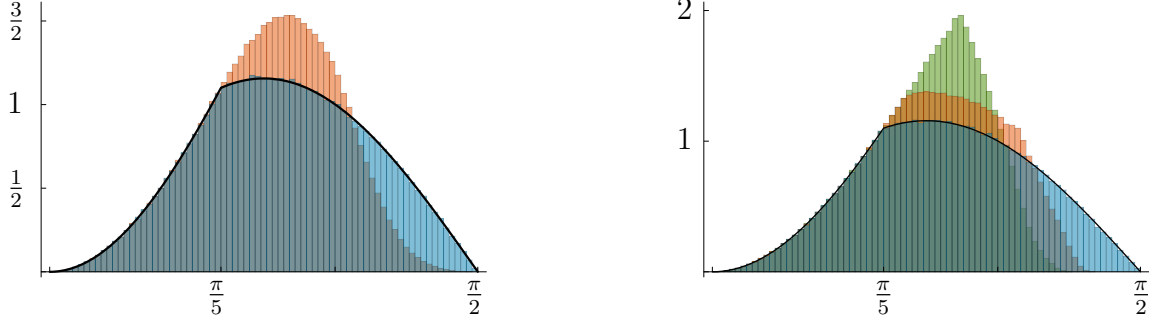


Figure 2.2: On the left are histograms of distances between 1,000,000 random pairs of points in $L(5; 1)$ [blue] and $L(5; 2)$ [red], computed using Algorithm 5; the curve shows the true density of distances in $L(5; 1)$ from (2.11). The right shows histograms of distances in $L(5; 2)$ from 1,000,000 random points to different fixed points, where the fixed points are the images in $L(5; 2)$ of $SU(2)$ elements of the form $\begin{pmatrix} \cos \phi & -\sin \phi \\ \sin \phi & \cos \phi \end{pmatrix}$, where $\phi = 0$ [blue], $\pi/8$ [red], and $\pi/4$ [green]; the curve shows the density of distances from random points in $L(5; 1)$ to any fixed point, again from (2.11). In particular, whereas the distributions of distances from random points to any fixed point in the homogeneous space $L(5; 1)$ are all the same, these distributions vary with the fixed point in the non-homogeneous $L(5; 2)$.

tively, again reflecting the fact that these spaces are neither isometric nor homeomorphic, though they are homotopy equivalent.

In the homogeneous case, it actually suffices to fix a representative of a fixed orbit, then check the distances between the chosen representative and each element of the other orbit. To see this, note that

$$\begin{aligned} d([A], [B]) &= \min_{1 \leq i, j \leq n} \{d(\omega^i \cdot A, \omega^j \cdot B)\} \\ &= \min_{1 \leq k \leq n} \{d(\omega^k \cdot AB^*, I)\}. \end{aligned}$$

If A, B are chosen according to Haar measure on $SU(2)$, then AB^* will also be distributed according to Haar measure, which is definitionally invariant under the (left or right) action of $SU(2)$ on itself. Hence, when doing a computational experiment, we can generate one random element of $SU(2)$, compute the orbit under the action, and then compute the distances from each element in the orbit to the identity. This yields the less computationally expensive Algorithm 6.

Algorithm 6 Expected Distance on $L(n; 1)$

```
1:  $D \leftarrow [0] * N$ 
2: for  $l \leftarrow 1, N$  do
3:    $A \leftarrow \text{RANDSU}(2)$ 
4:   orbitdata  $\leftarrow [0] * n$ 
5:   for  $k \leftarrow 1, n$  do
6:     orbitdata( $k$ )  $\leftarrow d(\omega^k \cdot A, I)$ 
7:   end for
8:    $D(l) \leftarrow \text{MIN}(\text{orbitdata})$ 
9: end for

return  $\text{MEAN}(D)$ 
```

For $N = 1,000,000$, a naïve Matlab implementation of Algorithm 5 gives the estimate $E[d; L(5, 1)] \approx 0.85897$ in about 940 seconds on a laptop, whereas Algorithm 6 yields $E[d; L(5, 1)] \approx 0.85921$ in about 86 seconds.

2.4 Distributions of Distances

We now restrict to the case that $L(n; m)$ is homogeneous; as previously mentioned, we can (and will) assume in what follows that $m = 1$. In this section we derive an analytic description of the distributions of distances on all the $L(n; 1)$ lens spaces.

As a first step to understanding these distributions of distances, we will compute the k th moment of distance between 2 random points in $L(n; 1)$. We now work in join coordinates (2.2), and we think of points in $L(n; 1)$ as orbits of points in \mathbb{S}^3 . Since $L(n; 1)$ is homogeneous, we may fix one point to be (the orbit of) the point $q = (1, 0, 0, 0)$. The fundamental domain of the Z_n action centered at this point (depicted in Figure 2.1) is determined by the join coordinate inequalities

$$-\frac{\pi}{n} \leq \theta_1, \theta_2 < \frac{\pi}{n},$$

so computing the expectation of k th power of distance in $L(n; 1)$ is equivalent to computing the expectation of $[d_{\mathbb{S}^3}(p, q)]^k$, where p varies over this fundamental domain. With p written in join coordinates, $d_{\mathbb{S}^3}(p, q) = \arccos(p \cdot q) = \arccos(\cos \theta_1 \cos \eta)$, so the k th moment of distance is

exactly

$$\begin{aligned} I_{n,k} &:= \mathbb{E}[d^k; L(n; 1)] = \frac{1}{\text{Vol}(L(n; 1))} \int_{L(n; 1)} [d_{L(n; 1)}([p], [q])]^k \, d\text{Vol}_{L(n; 1)} \\ &= \frac{n^2}{2\pi^2} \int_{-\pi/n}^{\pi/n} \int_{-\pi/n}^{\pi/n} \int_0^{\pi/2} \arccos^k(\cos \theta_1 \cos \eta) \cos \eta \sin \eta \, d\eta \, d\theta_1 \, d\theta_2. \end{aligned}$$

Obviously,

$$I_{n,0} = 1. \quad (2.3)$$

For $k \geq 1$, the integral expression for $I_{n,k}$ can be simplified somewhat by integrating out θ_2 , observing that the integrand is even in θ_1 , and making the substitution $\cos u = \cos \theta_1 \cos \eta$. Doing so produces the integral

$$I_{n,k} = \frac{2n}{\pi} \int_0^{\pi/n} \sec^2 \theta_1 \int_{\theta_1}^{\pi/2} u^k \cos u \sin u \, du \, d\theta_1. \quad (2.4)$$

Notice that this integral is improper for $n = 2$. For $n \geq 3$ we can apply the reduction formula [40, 2.631.1] for the inner integral to compute the first moment

$$I_{n,1} = \frac{\pi}{2n} + \frac{n-2}{4} \tan \frac{\pi}{n} \quad (2.5)$$

and the relation

$$I_{n,k} = -\frac{k(k-1)}{4} I_{n,k-2} + \frac{1}{k+1} \left(\frac{\pi}{n}\right)^k + \frac{n}{2\pi} \left[\left(\frac{\pi}{2}\right)^k - \left(\frac{\pi}{n}\right)^k \right] \tan \frac{\pi}{n} \quad (2.6)$$

for $k \geq 2$.

We can solve this recurrence using standard methods. The following theorem expresses the solution in terms of *generalized hypergeometric functions* ${}_pF_q \left[\begin{smallmatrix} a_1 & a_2 & \dots & a_p \\ b_1 & b_2 & \dots & b_q \end{smallmatrix}; z \right]$. In the definition of this class of functions, it is convenient to introduce the *Pochhammer symbol* $(a)_n$, defined by the

rule

$$(a)_n = \begin{cases} 1 & \text{if } n = 0 \\ a(a+1) \cdots (a+n-1) & \text{if } n \geq 1. \end{cases}$$

Equivalently, so long as a is not a nonpositive integer $(a)_n = \frac{\Gamma(a+n)}{\Gamma(a)}$.

In terms of the Pochhammer symbol, the generalized hypergeometric function is defined by the series

$${}_pF_q \left[\begin{matrix} a_1 & a_2 & \cdots & a_p \\ b_1 & b_2 & \cdots & b_q \end{matrix}; z \right] = \sum_{n=0}^{\infty} \frac{(a_1)_n (a_2)_n \cdots (a_p)_n z^n}{(b_1)_n (b_2)_n \cdots (b_q)_n n!},$$

provided none of the b_1, \dots, b_q is a nonpositive integer. When $p \leq q$, the series converges for all z and ${}_pF_q$ is entire.

Theorem 6. For each $k \geq 0$ and each $n \geq 3$, the k th moment of distance on $L(n; 1)$ is

$$I_{n,k} = \frac{1}{(k+1)(k+2)} \left[\frac{4}{k+3} \left(\frac{\pi}{n} \right)^{k+2} {}_1F_2 \left[\begin{matrix} 1 \\ \frac{k+4}{2}, \frac{k+5}{2} \end{matrix}; -\frac{\pi^2}{n^2} \right] \right. \\ \left. + \tan \frac{\pi}{n} \left(n \left(\frac{\pi}{2} \right)^{k+1} {}_1F_2 \left[\begin{matrix} 1 \\ \frac{k+3}{2}, \frac{k+4}{2} \end{matrix}; -\frac{\pi^2}{4} \right] - 2 \left(\frac{\pi}{n} \right)^{k+1} {}_1F_2 \left[\begin{matrix} 1 \\ \frac{k+3}{2}, \frac{k+4}{2} \end{matrix}; -\frac{\pi^2}{n^2} \right] \right) \right]. \quad (2.7)$$

Values for small k are given in Table 2.1.

Proof. While the difference equation (2.6) is second-order, the even and odd $I_{n,k}$ are independent of each other, so we can separately reduce each to a first-order difference equation and then solve that first-order equation.

For example, if $k = 2m$ is even, then defining $y_m := I_{n,2m}$ and index-shifting allows us to re-write (2.6) as

$$y_{m+1} = -\frac{(2m+2)(2m+1)}{4} y_m + \frac{1}{2m+3} \left(\frac{\pi}{n} \right)^{2m+2} + \frac{n}{2\pi} \left[\left(\frac{\pi}{2} \right)^{2m+2} - \left(\frac{\pi}{n} \right)^{2m+2} \right] \tan \frac{\pi}{n}$$

with initial condition $y_0 = I_{n,0} = 1$ from (2.3).

Table 2.1: Values of the k th moment of distance $I_{n,k}$ for small k and $n \geq 3$.

k	$I_{n,k}$
0	1
1	$\frac{\pi}{2n} + \left(\frac{1}{4}n - \frac{1}{2}\right)\tan \frac{\pi}{n}$
2	$-\frac{1}{2} + \frac{\pi^2}{3n^2} + \left(\frac{\pi}{8}n - \frac{\pi}{2n}\right)\tan \frac{\pi}{n}$
3	$-\frac{3\pi}{4n} + \frac{\pi^3}{4n^3} + \left(\frac{\pi^2-6}{16}n + \frac{3}{4} - \frac{\pi^2}{2n^2}\right)\tan \frac{\pi}{n}$
4	$\frac{3}{2} - \frac{\pi^2}{n^2} + \frac{\pi^4}{5n^4} + \left(\frac{\pi^3-12\pi}{32}n + \frac{3\pi}{2n} - \frac{\pi^3}{2n^3}\right)\tan \frac{\pi}{n}$
5	$\frac{15\pi}{4n} - \frac{5\pi^3}{4n^3} + \frac{\pi^5}{6n^5} + \left(\frac{\pi^4-20\pi^2+120}{64}n - \frac{15}{4} + \frac{5\pi^2}{2n^2} - \frac{\pi^4}{2n^4}\right)\tan \frac{\pi}{n}$
6	$-\frac{45}{4} + \frac{15\pi^2}{2n^2} - \frac{3\pi^4}{2n^4} + \frac{\pi^6}{7n^6} + \left(\frac{\pi^5-30\pi^3+360\pi}{128}n - \frac{45\pi}{4n} + \frac{15\pi^3}{4n^3} - \frac{\pi^5}{2n^5}\right)\tan \frac{\pi}{n}$
7	$-\frac{315\pi}{8n} + \frac{105\pi^3}{8n^3} - \frac{7\pi^5}{4n^5} + \frac{\pi^7}{8n^7} + \left(\frac{\pi^6-42\pi^4+840\pi^2-5040}{256}n + \frac{315}{8} - \frac{105\pi^2}{4n^2} + \frac{21\pi^4}{4n^4} - \frac{\pi^6}{2n^6}\right)\tan \frac{\pi}{n}$

This is in the standard form $y_{m+1} = g_m y_m + h_m$ for general first-order linear difference equations, and hence has solution

$$\begin{aligned}
 y_m &= \prod_{j=0}^{m-1} g_j \left(y_0 + \sum_{j=0}^{m-1} \frac{h_j}{\prod_{\ell=0}^j g_\ell} \right) \\
 &= (-1)^m \frac{(2m)!}{2^{2m}} \left(1 + \sum_{j=0}^{m-1} \frac{(-1)^{j+1}}{(2j+3)!} \left(\frac{2\pi}{n} \right)^{2j+2} + \frac{n}{2\pi} \tan \frac{\pi}{n} \sum_{j=0}^{m-1} \frac{(-1)^{j+1}}{(2j+2)!} \left(\pi^{2j+2} - \left(\frac{2\pi}{n} \right)^{2j+2} \right) \right)
 \end{aligned} \tag{2.8}$$

after some simplification.

In turn, each of the finite sums becomes one of the hypergeometric functions in (2.7). For example,

$$\begin{aligned}
 1 + \sum_{j=0}^{m-1} \frac{(-1)^{j+1}}{(2j+3)!} \left(\frac{2\pi}{n} \right)^{2j+2} &= \frac{n}{2\pi} \sum_{j=0}^m \frac{(-1)^j}{(2j+1)!} \left(\frac{2\pi}{n} \right)^{2j+1} \\
 &= \frac{n}{2\pi} \sum_{j=0}^{\infty} \frac{(-1)^j}{(2j+1)!} \left(\frac{2\pi}{n} \right)^{2j+1} - \frac{n}{2\pi} \sum_{j=m+1}^{\infty} \frac{(-1)^j}{(2j+1)!} \left(\frac{2\pi}{n} \right)^{2j+1} \\
 &= \frac{n}{2\pi} \sin \frac{2\pi}{n} - \frac{(-1)^{m+1}}{(2m+3)!} \left(\frac{2\pi}{n} \right)^{2m+2} \sum_{i=0}^{\infty} \frac{1}{(m+2)_i (m+\frac{5}{2})_i} \left(-\frac{\pi^2}{n^2} \right)^i.
 \end{aligned}$$

After multiplying each term by $1 = \frac{i!}{i!} = \frac{(1)_i}{i!}$, the remaining sum is the standard power series representation of ${}_1F_2 \left[\begin{matrix} 1 \\ m+2, m+\frac{5}{2} \end{matrix}; -\frac{\pi^2}{n^2} \right]$.

Simplifying the remaining terms in (2.8) and replacing $2m$ with k yields the solution (2.7) for the even moments.

On the other hand, notice that we can solve the difference equation (2.6) for $I_{n,1}$ independent of the value of $I_{n,-1}$. Therefore, if we define $z_m = I_{n,2m-1}$ for $m \geq 1$, we can choose the initial condition z_0 arbitrarily. If we choose $z_0 = 1$,⁷ then the difference equation and initial condition for z_m are essentially identical to those in the problem we just solved. Indeed, solving the system and plugging in $k = 2m - 1$ at the end yields the exact same expression (2.7) for the odd moments, completing the proof. \square

We can't plug $n = 2$ into the expressions (2.5) and (2.6), but taking the limit as $n \rightarrow 2$ gives the corresponding values of the improper integral (2.4):

$$I_{2,1} = \frac{1}{\pi} + \frac{\pi}{4}$$

$$I_{2,k} = -\frac{k(k-1)}{4} I_{2,k-2} + \frac{1}{k+1} \left(\frac{\pi}{2}\right)^k + \frac{k}{\pi} \left(\frac{\pi}{2}\right)^{k-1}.$$

The solution of this initial value problem (together with $I_{2,0} = 1$) is simply the limit of (2.7) as $n \rightarrow 2$:

Corollary 10. *The k th moment of distance on $L(2; 1) = \mathbb{RP}^3$ is*

$$I_{2,k} = \frac{1}{k+1} \left(\frac{\pi}{2}\right)^k \left[2 {}_1F_2 \left[\begin{matrix} 1 \\ \frac{k+3}{2}, \frac{k+4}{2} \end{matrix}; -\frac{\pi^2}{4} \right] + \frac{\pi^2}{(k+2)(k+3)} \left({}_1F_2 \left[\begin{matrix} 1 \\ \frac{k+4}{2}, \frac{k+5}{2} \end{matrix}; -\frac{\pi^2}{4} \right] - \frac{4}{k+4} {}_1F_2 \left[\begin{matrix} 2 \\ \frac{k+5}{2}, \frac{k+6}{2} \end{matrix}; -\frac{\pi^2}{4} \right] \right) \right].$$

⁷We emphasize that $I_{n,-1} \neq 1$; in fact, it is not too hard to show that

$$I_{n,-1} = \frac{n}{\pi} \left[\gamma - \text{Ci} \left(\frac{2\pi}{n} \right) + \log \left(\frac{2\pi}{n} \right) + \left(\text{Si}(\pi) - \text{Si} \left(\frac{2\pi}{n} \right) \right) \tan \frac{\pi}{n} \right],$$

where $\gamma \approx 0.577$ is the Euler–Mascheroni constant and Ci and Si are the cosine integral and sine integral functions, respectively.

We point out that the partially oriented flag manifolds $F\ell((1, 1, 1); \{\{1\}, \{2\}, \{3\}\})$ and $F\ell((1, 1, 1), \{\{1\}, \{2, 3\}\})$ considered in our previous paper [14] are (up to a global scale factor of 2) the lens spaces $L(2; 1)$ and $L(4; 1)$, respectively, and indeed the expected values of distance that we computed on those spaces were exactly $2I_{2,1} = \frac{2}{\pi} + \frac{\pi}{2}$ and $2I_{4,1} = 1 + \frac{\pi}{4}$.

For small k the finite sum formula (2.8) is typically more useful than (2.7) — and, indeed, the finite sum is what we see in Table 2.1 — but one virtue of Theorem 6 and Corollary 10 is that we can easily determine the asymptotic behavior of $I_{n,k}$ as $k \rightarrow \infty$ by retaining only the leading terms in the power series representations of the hypergeometric functions.

Corollary 7. *For fixed $n \geq 3$, the asymptotic growth of the k th moment of distance on $L(n; 1)$ as $k \rightarrow \infty$ is*

$$I_{n,k} \sim \frac{n}{k^2} \left(\frac{\pi}{2}\right)^{k+1} \tan \frac{\pi}{n}.$$

For $n = 2$, the asymptotic growth of the k th moment of distance on $L(2; 1) = \mathbb{RP}^3$ is

$$I_{2,k} \sim \frac{2}{k} \left(\frac{\pi}{2}\right)^k.$$

On the other hand, if we fix k and let n get large, only the middle term in (2.7) survives:

Corollary 11. *For fixed $k \geq 0$,*

$$\lim_{n \rightarrow \infty} I_{n,k} = \frac{\pi}{(k+2)(k+1)} \left(\frac{\pi}{2}\right)^{k+1} {}_1F_2 \left[\begin{matrix} 1 \\ \frac{k+3}{2}, \frac{k+4}{2} \end{matrix}; -\frac{\pi^2}{4} \right].$$

Values for small k are given in Table 2.2.

Another way to package the information contained in Theorem 6 is by computing the moment-generating function of distance:

Theorem 8. *For $n \geq 3$, the moment-generating function of distance on $L(n; 1)$ is*

$$M_n(t) = \frac{2n}{\pi(4+t^2)} \left(\frac{2(e^{t\pi/n} - 1)}{t} + \tan \frac{\pi}{n} (e^{t\pi/2} - e^{t\pi/n}) \right). \quad (2.9)$$

Table 2.2: $\lim_{n \rightarrow \infty} I_{n,k}$ for small k . The coefficient of π is the coefficient of $n \tan \frac{\pi}{n}$ in the corresponding entry in Table 2.1, and the remaining term is the constant term from Table 2.1.

k	$\lim_{n \rightarrow \infty} I_{n,k}$	Decimal approx.
0	1	1.00000
1	$\frac{1}{4}\pi$	0.78539
2	$-\frac{1}{2} + \frac{\pi}{8}\pi$	0.73370
3	$\frac{\pi^2-6}{16}\pi$	0.75979
4	$\frac{3}{2} + \frac{\pi^3-12\pi}{32}\pi$	0.84293
5	$\frac{\pi^4-20\pi^2+120}{64}\pi$	0.98258
6	$-\frac{45}{4} + \frac{\pi^5-30\pi^3+360\pi}{128}\pi$	1.18885
7	$\frac{\pi^6-42\pi^4+840\pi^2-5040}{256}\pi$	1.48090

For $n = 2$, the moment-generating function is

$$M_2(t) = \frac{4}{\pi(4+t^2)} \left(\frac{2(e^{t\pi/2} - 1)}{t} + te^{t\pi/2} \right).$$

Proof. By definition,

$$M_n(t) = \mathbb{E}(e^{td}; L(n; 1)) = \frac{2n}{\pi} \int_0^{\pi/n} \sec^2 \theta_1 \int_{\theta_1}^{\pi/2} e^{tu} \cos u \sin u \, du \, d\theta_1 \quad (2.10)$$

using the same substitution that produced (2.4). Using the identity $\sin 2u = 2 \sin u \cos u$ and integrating by parts twice yields

$$M_n(t) = \frac{2n}{\pi(4+t^2)} \left(\frac{e^{t\pi/n} - 1}{t} + \tan \frac{\pi}{n} e^{t\pi/2} - \int_0^{\pi/n} e^{t\theta_1} (t \tan \theta_1 + \sec^2 \theta_1 - 1) \, d\theta_1 \right)$$

for $n \geq 3$. Integrating the first term inside the integral by parts produces a term which cancels the second, and the rest is straightforward.

For $n = 2$, evaluating the indefinite integral (2.10) boils down to taking the limit of (2.9) as $n \rightarrow 2$, which produces the desired expression for $M_2(t)$. \square

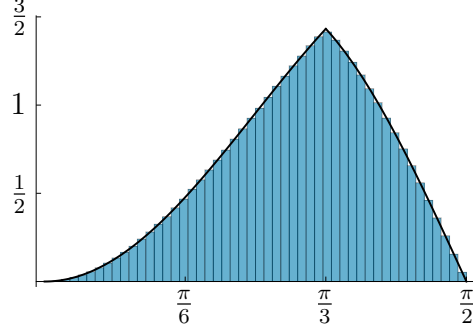


Figure 2.3: Histogram of distances between 10,000,000 random points on $L(3; 1)$ generated by Algorithm 6 compared to the pdf $f_3(x) = \frac{6}{\pi} (\sin^2 x + \Theta(x - \pi/3)(-\sin^2 x + \sqrt{3} \sin x \cos x))$.

We can recover the probability density function (pdf) f_n of distance as the inverse Laplace transform of $M_n(-t)$:

$$f_2(x) = \frac{4}{\pi} \sin^2 x$$

$$f_n(x) = \frac{2n}{\pi} \left(\sin^2 x + \Theta(x - \pi/n) \left(-\sin^2 x + \sin x \cos x \tan \frac{\pi}{n} \right) \right), \quad (2.11)$$

where Θ is the Heaviside function which is zero for negative values and 1 for positive values. See Figure 2.3.

As $n \rightarrow \infty$ we see that $f_n(x) \rightarrow \sin 2x$, the pdf of the *sine distribution* introduced by Gilbert in the study of moon craters [41, 42]. It is not so surprising to see this distribution: as $n \rightarrow \infty$ the lens spaces $L(n; 1)$ converge in the Gromov–Hausdorff sense to a 2-sphere of radius $1/2$ [43, Example 2.85], and the distance distribution on this sphere is exactly the sine distribution.

In turn, given the pdf, we can integrate to get the cumulative distribution function $F_n(x)$ of distance on $L(n; 1)$:

$$F_2(x) = \frac{2}{\pi} (x - \sin x \cos x)$$

$$F_n(x) = \frac{n}{\pi} \left(x - \sin x \cos x + \Theta(x - \pi/n) \left(\frac{\pi}{n} - x + \sin x \cos x - \cos^2 x \tan \frac{\pi}{n} \right) \right);$$

see Figure 2.4.

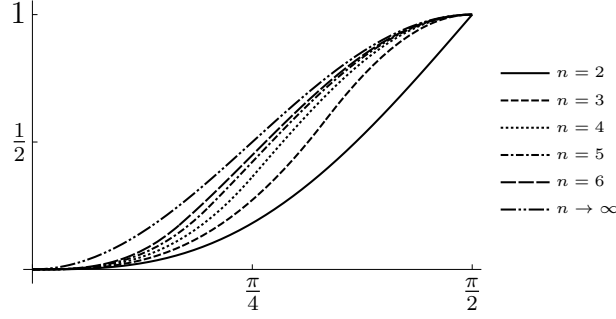


Figure 2.4: The cumulative distribution function of distance on $L(n; 1)$ for $2 \leq n \leq 6$ and in the limit as $n \rightarrow \infty$.

By definition,

$$F_n(x) = \mathbb{P}(d(p, q) \leq x) = \frac{\text{Vol } B_q(x)}{\text{Vol } L(n; 1)}$$

where $q \in L(n; 1)$ is any fixed point and $p \in L(n; 1)$ is random; since $L(n; 1)$ is homogeneous this is independent of q . Hence, we can compute the volume $V_n(r) := \text{Vol } B_q(r)$ of a ball of radius r in $L(n; 1)$ as

$$V_n(r) = \text{Vol}(L(n; 1))F_n(r) = \frac{2\pi^2}{n}F_n(r).$$

This proves:

Theorem 9. For $n \geq 2$, the volume of a ball of radius r in $L(n; 1)$ is

$$V_n(r) = \begin{cases} 2\pi(r - \sin r \cos r) & \text{if } r \leq \frac{\pi}{n} \\ \frac{2\pi^2}{n} - 2\pi \cos^2 r \tan \frac{\pi}{n} & \frac{\pi}{n} < r < \frac{\pi}{2} \\ \frac{\pi}{2} & r \geq \frac{\pi}{2} \end{cases}$$

The last case is easily explained by the fact that the diameter of $L(n; 1)$ is $\frac{\pi}{2}$. Notice also that we never reach the second case when $n = 2$. Finally, $2\pi(r - \sin r \cos r)$ is simply the volume of a ball of radius r in \mathbb{S}^3 ; not surprisingly, things get interesting only when $r > \frac{\pi}{n}$, the injectivity radius of $L(n; 1)$.

Thinking in these geometric terms, the pdfs from (2.11) are scaled areas of spheres. Rescaling by the same $\frac{2\pi^2}{n}$ factor as above yields the surface area $A_n(r)$ of the sphere of radius r centered at

any point in $L(n; 1)$:

$$A_n(r) = \begin{cases} 4\pi \sin^2 r & \text{if } r \leq \frac{\pi}{n} \\ 4\pi \sin r \cos r \tan \frac{\pi}{n} & \text{else.} \end{cases}$$

2.5 Concluding Remarks

Three-dimensional lens spaces are a family of topological/geometric objects that have played a historical role in the development of manifold theory. Their interest derives both from their ease of construction and as examples of manifolds exhibiting unusual phenomena. They appear across several disciplines including topology, geometry, cosmography, and data science, and are a natural setting for spherical data with cyclic symmetries. While lens spaces have been well studied from varying perspectives, we are unaware of other sources which consider distance distributions on them.

Distance distributions have been used in geometric classification and can be used to understand general metric measure spaces. While they can often be approximated effectively using Monte Carlo techniques, it would be interesting to determine analytic expressions for distance distributions on a broader class of manifolds. For manifolds which are not homogeneous spaces, the distribution of distances from a fixed point depends on the point. In other words, the volume formula for a ball is dependent on the location of the center of the ball in the manifold. In turn, integrating the distribution of distances from a fixed point as the fixed point varies over the manifold yields the distribution of distances between pairs of random points.

Non-homogeneous lens spaces, both in three and in higher dimensions, are particularly tractable examples of non-homogeneous manifolds, so in these spaces it may be feasible to find analytic expressions for the distributions of distances both from a fixed point and between random points.

Chapter 3

Spatially Extended Dislocations Produced by the Dispersive Swift-Hohenberg Equation ⁸

3.1 Introduction

The Kuramoto-Sivashinsky (KS) equation occurs in many contexts, including the nonlinear evolution of flame fronts [44], concentration waves in reaction-diffusion systems [45], and nanoscale pattern formation produced by bombardment of a solid surface with a broad ion beam [46–48]. It is among the simplest partial differential equations that exhibit spatiotemporal chaos. Adding a linearly dispersive term to the one-dimensional (1D) KS equation yields the dispersive KS equation in 1D,

$$u_t = -u_{xx} - u_{xxxx} + u_x^2 + \gamma u_{xxx}, \quad (3.1)$$

where $u = u(x, t)$ and γ is real. (The 1D KS equation is recovered for $\gamma = 0$). Surprisingly, when γ is large and the initial condition is low amplitude spatial white noise, highly ordered patterns emerge at sufficiently long times and the spatio-temporal chaos that would otherwise prevail is suppressed [49]. This remains true if a strong linearly dispersive term is added to the anisotropic KS equation in two dimensions (2D) [48, 50].

In the limit that γ tends to infinity, the 1D dispersive KS equation (3.1) becomes the Korteweg-DeVries (KdV) equation. The KdV equation has solutions in which multiple solitons are present. For large but finite γ , there is a repulsive interaction between neighboring solitons, and the solitons eventually arrange themselves in an ordered chain as a consequence [51]. Thus, there is some understanding of how order emerges in solutions of Eq. (3.1) for $\gamma \gg 1$. This picture does not carry over to the anisotropic 2D KS equation with added dispersion, however.

⁸This article is with Patrick Shipman and Mark Bradley. This manuscript was first published in Physical Review E.

When a solid surface is bombarded with a broad ion beam and the angle of ion incidence θ exceeds a threshold value θ_c , self-assembled ripples with wavelengths as short as 10 nm form [52]. If the patterns formed were not almost always disordered, ion bombardment could become a widely employed method of fabricating large-area nanostructures with feature sizes too small to be attained by conventional optical lithography. After rescaling, the equation that describes the time evolution of an ion-bombarded solid surface for θ just above θ_c is

$$u_t = -u_{xx} - u_{xxxx} + u_x^2 + u_{yy} + \gamma u_{xxx}, \quad (3.2)$$

where $u = u(x, y, t)$ is the height of the solid surface about the point (x, y) in the $x - y$ plane at time t and $\gamma \propto (\theta - \theta_c)^{-1/2}$ diverges as $\theta \rightarrow \theta_c^+$ [48]. Equation (3.2) reduces to Eq. (3.1) if u is independent of y . It is a simplified version of the anisotropic 2D KS equation with linear dispersion, and simulations show that it produces highly ordered ripples if γ is large, i.e., if θ is just above θ_c [48, 50]. This finding has the potential to revolutionize the field of nanoscale patterning by ion bombardment, and, accordingly, it is of considerable importance to understand how strong linear dispersion modifies the dynamics.

A second intriguing observation emerges from simulations of Eq. (3.2): dispersion can lead to the formation of transient raised and depressed triangular regions that are traversed by ripples for moderate values of γ . Triangular nanostructures of this kind have been observed in many experiments in which a solid surface is bombarded with an obliquely incident ion beam [52–62], but their formation is currently poorly understood. In simulations, once the triangular nanostructures have disappeared, the surface has a disordered appearance with streaks parallel to the x axis.

The Swift-Hohenberg equation (SHE) is an important model equation in the study of pattern formation in spatially extended nonlinear systems [63]. Close to the threshold for pattern formation, analytical results can be obtained because there is a narrow band of unstable wavelengths. In particular, the amplitude equation, which describes the slow variation of the pattern in space and time, can be derived.

In this paper, we study the SHE with added linear dispersion in both one and two dimensions. Our motivation for doing so is this: the effect of strong linear dispersion can be better understood in the context of the SHE than for the KS equation because there is a narrow band of unstable wavelengths close to threshold in the case of the SHE. We find that the 2D dispersive Swift-Hohenberg equation (DSHE) produces a unique type of spatially extended defect if the linear dispersion is sufficiently strong. These defects — which we will refer to as “seams” — are essentially dislocations that are smeared out along line segments oriented obliquely to the x axis. As we will discuss, these are related to the triangular nanostructures that are observed when a solid surface is bombarded with a broad ion beam.

Simplicity emerges in the DSHE in two limits: close to threshold and in the limit of strong dispersion. Close to threshold, we show that the amplitude equation for the DSHE is a special case of the anisotropic complex Ginzburg-Landau equation (ACGLE). The seams in the original equation of motion are spiral waves in the ACGLE. These spiral waves and the corresponding seam defects tend to arrange themselves into chains. We predict the velocity of the spiral wave cores and the spacing between them for a particular type of controlled initial condition. In the limit of strong dispersion, on the other hand, we carry out a perturbative analysis that shows that the stripes have a nearly sinusoidal dependence on position. The analysis also yields the stripe’s propagation velocity and a relationship between their amplitude and wavelength. These predictions are in excellent accord with the results of our numerical integrations of the equation of motion.

This paper is organized as follows: In Sec. 3.2, we recast the DSHE in dimensionless form and perform a linear stability analysis. We find an approximate solution to the 1D DSHE in the limit of strong linear dispersion in Sec. 3.3. In Sec. 3.4, we derive the amplitude equation that applies close to the threshold for pattern formation. Simulations of the DSHE and the corresponding amplitude equation are carried out in Sec. 3.5. We also study the dynamics of chains of spiral waves both analytically and numerically. Our work is placed in context in Sec. 3.6, and we conclude in Sec. 3.7.

3.2 The Dispersive Swift-Hohenberg Equation

In this paper, we study the DSHE

$$u_t = -a\Delta^2 u - bu_{xx} + cu_{yy} + du_{xxx} + eu - fu^3 \quad (3.3)$$

in one and two dimensions. Here $u = u(x, y, t)$ and a, b, \dots , and f are real parameters. We confine our attention to the case in which a, b and f are positive. We introduce the dimensionless parameters $\tilde{u} = 2(af/b^2)^{1/2}u$, $\tilde{x} = \text{sgn}(d)[b/(2a)]^{1/2}x$, $\tilde{y} = \text{sgn}(d)[b/(2a)]^{1/2}y$, and $\tilde{t} = [b^2/(4a)]t$. Dropping the tildes, we find the rescaled equation of motion to be

$$u_t = -\Delta^2 u - 2(u_{xx} - \beta u_{yy}) + \gamma u_{xxx} + (\mu - 1)u - u^3, \quad (3.4)$$

where $\mu = 1 + 4ae/b^2$, $\beta = c/b$ and $\gamma = [2d^2/(ab)]^{1/2}$. Note that γ is nonnegative. For the case $\gamma = 0$, there is no dispersion and Eq. (3.4) reduces to the usual SHE.

The equation of motion (3.4) has the equilibrium solution $u = 0$. Linearizing about this solution, we obtain

$$u_t = -\Delta^2 u - 2(u_{xx} - \beta u_{yy}) + \gamma u_{xxx} + (\mu - 1)u. \quad (3.5)$$

Setting $u = \exp(i\vec{k} \cdot \vec{x} + \sigma t)$, we find the dispersion relation

$$\sigma = -k^4 + 2(k_x^2 - \beta k_y^2) + \mu - 1 - i\gamma k_x^3, \quad (3.6)$$

where $\vec{k} = (k_x, k_y)$ is the wave vector. An easy calculation shows that $\text{Re } \sigma$ is maximized for $\vec{k} = (\pm 1, 0)$ and has the maximum value μ provided that $\beta > -1$, which we assume to be the case. This tells us that the solution $u = 0$ is linearly stable when $\mu < 0$ and linearly unstable whenever $\mu > 0$. By the continuity of $\text{Re } \sigma = \text{Re } \sigma(\vec{k})$, it follows that there are neighborhoods about the points $\vec{k} = (\pm 1, 0)$ in which $\text{Re } \sigma$ is positive if $\mu > 0$. For small, positive μ , neither neighborhood

contains the zero vector, indicating a type-I instability. Moreover, the phase velocity is

$$v = -\frac{\text{Im } \sigma}{k} = \gamma \frac{k_x^3}{k}. \quad (3.7)$$

For the 1D case in which $u_y = 0$, the phase velocity (3.7) reduces to $v = \gamma k_x^2$.

3.3 The Strongly Dispersive Limit

We begin by studying the equation of motion (3.4) when dispersion is strong, i.e., the case in which $\gamma \gg 1$. We set $u = u(x, t)$ in Eq. (3.4) and so obtain

$$u_t = -(1 + \partial_x^2)^2 u + \gamma u_{xxx} + \mu u - u^3. \quad (3.8)$$

We seek solutions to Eq. (3.8) of the form $u = u(x - vt)$. Moreover, we will set $\epsilon = \gamma^{-1}$ and take γ to be large. Equation (3.8) now yields

$$u_{xxx} + \omega u_x + \epsilon [\mu u - (1 + \partial_x^2)^2 u - u^3] = 0, \quad (3.9)$$

where $\omega \equiv v/\gamma = \epsilon v$. Next, we assume that

$$u = u_0 + \epsilon u_1 + \epsilon^2 u_2 + \text{h.o.t.} \quad \text{and} \quad (3.10)$$

$$\omega = \omega_0 + \epsilon \omega_1 + \epsilon^2 \omega_2 + \text{h.o.t.}, \quad (3.11)$$

where h.o.t. stands for higher-order terms. Then, to zeroth order in ϵ , Eq. (3.9) reads

$$u_{0xxx} + \omega_0 u_{0x} = 0. \quad (3.12)$$

The general solution to Eq. (3.12) is given by

$$u_0 = C + A \cos(\sqrt{\omega_0} x + \phi), \quad (3.13)$$

where C , A and ϕ are arbitrary constants. By choosing the origin appropriately, we may arrange for ϕ to be zero. Thus, we have

$$u_0 = C + A \cos(kx), \quad (3.14)$$

where $k \equiv \sqrt{\omega_0}$ is the wave number.

To first order, Eq. (3.9) may be written

$$\begin{aligned} u_{1xxx} + \omega_0 u_{1x} &= -\omega_1 u_{0x} - \mu u_0 + (1 + \partial_x^2)^2 u_0 + u_0^3 \\ &\equiv q. \end{aligned} \quad (3.15)$$

Let $L_0 = \partial_x^3 + k^2 \partial_x$, so that Eq. (3.15) can be written compactly as

$$L_0 u_1 = q. \quad (3.16)$$

It is a straightforward exercise to show that $L_0 : C^3[-L, L] \rightarrow C[-L, L]$ is a Fredholm operator. The Fredholm Alternative then implies that q is orthogonal to $\ker L_0^\dagger$, where L_0^\dagger denotes the adjoint with respect to the L^2 inner product. Because

$$\ker L_0^\dagger = \text{span}\{1, e^{ikx}, e^{-ikx}\}, \quad (3.17)$$

the constant term in q must be zero, i.e.,

$$-\mu C + C + C^3 = 0. \quad (3.18)$$

Equivalently, $C = 0$ or $C^2 = \mu - 1$. Since C is real, the latter possibility is ruled out whenever $\mu < 1$, and we take this to be the case. This means that

$$u_0 = A \cos(kx). \quad (3.19)$$

Further still, we have

$$q = \omega_1 k A \sin(kx) - \mu A \cos(kx) + A(1 - k^2)^2 \cos(kx) + A^3 \cos^3(kx) \quad (3.20)$$

$$= \omega_1 k A \sin(kx) - \mu A \cos(kx) + A(1 - k^2)^2 \cos(kx) + \frac{1}{4} A^3 [\cos(3kx) + 3 \cos(kx)]. \quad (3.21)$$

$q \in (\ker L_0^\dagger)^\perp$ therefore implies that $\omega_1 = 0$ and

$$A^2 = \frac{4}{3} [\mu - (1 - k^2)^2]. \quad (3.22)$$

Because $A^2 \geq 0$, we must have

$$|1 - k^2| \leq \sqrt{\mu}. \quad (3.23)$$

This establishes that a steady-state, propagating solution is obtained only for wave numbers in the linearly unstable band. We also see that $A^2 = 4\text{Re} \sigma(\vec{k})/3$, and so we come to the natural conclusion that the higher the linear growth rate, the higher the amplitude of the corresponding steady-state solution. Now note that Eq. (3.15) reduces to

$$u_{1xxx} + k^2 u_{1x} = \frac{1}{4} A^3 \cos(3kx). \quad (3.24)$$

We will seek a solution to Eq. (3.24) of the form

$$u_1 = B \sin(3kx). \quad (3.25)$$

In doing so, we obtain

$$B = \frac{1}{96} k^{-3} A^3, \quad (3.26)$$

and hence

$$u(x, t) = A \cos(k(x - vt)) + \frac{1}{96} k^{-3} A^3 \epsilon \sin(3k(x - vt)) + O(\epsilon^2), \quad (3.27)$$

where A and k satisfy Eqs. (3.22) and (3.23), respectively. Equation (3.27) gives the approximate form of the propagating, periodic solution to Eq. (3.8). The presence of the correction with wave number $3k$ in Eq. (3.27) is to be expected because a cubic nonlinearity is present in the equation of motion (3.8).

Since $\omega_0 = k^2$ and $\omega_1 = 0$,

$$\omega = \omega_0 + \epsilon \omega_1 + O(\epsilon^2) = k^2 + O(\epsilon^2). \quad (3.28)$$

This in turn gives us the phase velocity,

$$v = \gamma k^2 + O(\epsilon). \quad (3.29)$$

This shows that in the strongly dispersive ($\gamma \rightarrow \infty$) limit, the phase velocity (3.29) obtained by a perturbative analysis of the full nonlinear equation of motion reduces to the phase velocity (3.7) for the linearized problem.

If we begin a simulation of the equation of motion (3.8) with a low amplitude spatial white noise initial condition, it is not evident whether the solution will evolve toward a solution of the form (3.27) with the phase velocity given by Eq. (3.29) and with A and k related by Eq. (3.22). Even if that turns out to be the case, it is not clear *a priori* what the chosen value of k will be, although the inequality (3.23) would have to be satisfied. Numerical integrations of Eq. (3.8) will be carried out in Section 3.5 to address these issues.

3.4 Near-Threshold Behavior

In this section, we analyze the equation of motion (3.4) close to threshold, i.e., for small, positive μ . Because we have assumed that $\beta > -1$, there are small neighborhoods about the critical wave vectors $\vec{k} = (\pm 1, 0)$ in which $\text{Re } \sigma(\vec{k})$ is positive. This implies the existence of an amplitude equation. To find this amplitude equation, we begin by writing Eq. (3.4) as

$$u_t = \mathcal{L}u - u^3, \quad (3.30)$$

where

$$\mathcal{L} \equiv -\Delta^2 - 2(\partial_x^2 - \beta\partial_y^2) + \gamma\partial_x^3 + \mu - 1 \quad (3.31)$$

is the linear part of the differential operator on the right-hand side of Eq. (3.4). The linear dispersion relation tells us that, to leading order, the solution to Eq. (3.4) is a traveling plane wave with wave number $k = 1$ that propagates in the x direction. Note that the phase velocity of the mode with wave vector $\vec{k} = (1, 0)$ is γ , and the corresponding group velocity is 3γ . Accordingly, we begin with the ansatz

$$\begin{aligned} u &= \mu^{1/2}u_0 + \mu u_1 + \text{h.o.t.} \\ &= \mu^{1/2}A(\xi, Y, T)e^{i(x-\gamma t)} + \text{c.c.} + \mu u_1 + \text{h.o.t.}, \end{aligned} \quad (3.32)$$

where $\xi \equiv \mu^{1/2}(x - 3\gamma t)$, $Y \equiv \mu^{1/2}y$ and $T \equiv \mu t$ are slow variables and c.c. denotes the complex conjugate. As a result, we must make the replacements $\partial_x \mapsto \partial_x + \mu^{1/2}\partial_\xi$, $\partial_y \mapsto \mu^{1/2}\partial_Y$ and $\partial_t \mapsto \partial_t - 3\mu^{1/2}\gamma\partial_\xi + \mu\partial_T$ in Eq. (3.30). This leads to

$$\mathcal{L} \mapsto L_0 + \mu^{1/2}L_1 + \mu L_2 + \text{h.o.t.}, \quad (3.33)$$

where

$$L_0 = \gamma \partial_x^3 - (\partial_x^2 + 1)^2 \quad (3.34)$$

$$L_1 = (-4\partial_x^3 + 3\gamma\partial_x^2 - 4\partial_x) \partial_\xi \quad (3.35)$$

$$L_2 = -6\partial_\xi^2 \partial_x^2 - 2\partial_x^2 \partial_Y^2 + 3\gamma\partial_\xi^2 \partial_x - 2\partial_\xi^2 + 2\beta\partial_Y^2 + 1. \quad (3.36)$$

To order $\mu^{1/2}$, Eq. (3.30) is

$$\partial_t u_0 = L_0 u_0. \quad (3.37)$$

This automatically holds since we set

$$u_0 = A(\xi, Y, T) e^{i(x-\gamma t)} + \text{c.c.} \quad (3.38)$$

To order μ , Eq. (3.30) yields

$$\partial_t u_1 - 3\gamma\partial_\xi u_0 = L_1 u_0 + L_0 u_1. \quad (3.39)$$

Since $L_1 u_0 = -3\gamma\partial_\xi u_0$, Eq. (3.39) reduces to

$$\partial_t u_1 = L_0 u_1. \quad (3.40)$$

This merely tells us that

$$u_1 = A_1(\xi, Y, T) e^{i(x-\gamma t)} + \text{c.c.} \quad (3.41)$$

To order $\mu^{3/2}$, Eq. (3.30) gives

$$\partial_T u_0 - 3\gamma\partial_\xi u_1 + \partial_t u_2 = L_2 u_0 + L_1 u_1 + L_0 u_2 - u_0^3. \quad (3.42)$$

Next, using Eq. (3.38), Eq. (3.42) can be rearranged to obtain

$$\begin{aligned}\Lambda u_2 &= \left[-A_T + A + 4 \left(1 + i \frac{3}{4} \gamma \right) A_{\xi\xi} + 2(1 + \beta) A_{YY} - 3|A|^2 A \right] e^{i(x-\gamma t)} \\ &\quad - A^3 e^{3i(x-\gamma t)} + \text{c.c.}, \\ &\equiv Q,\end{aligned}\tag{3.43}$$

where $\Lambda \equiv \partial_t - \gamma \partial_x^3 + (\partial_x^2 + 1)^2$. A quick check shows that $e^{i(x-\gamma t)} \in \ker \Lambda$, which implies that

$$A_T = A + 4 \left(1 + i \frac{3}{4} \gamma \right) A_{\xi\xi} + 2(1 + \beta) A_{YY} - 3|A|^2 A.\tag{3.44}$$

Equation (3.44) is the amplitude equation for the two-dimensional (2D) DSHE, Eq. (3.4). If we put $A = \tilde{A}/\sqrt{\mu}$ in Eq. (3.44), drop the tilde, and write the result in terms of the original coordinates, we obtain

$$A_t + 3\gamma A_x = \mu A + 4 \left(1 + i \frac{3}{4} \gamma \right) A_{xx} + 2(1 + \beta) A_{yy} - 3|A|^2 A.\tag{3.45}$$

We prefer, however, to put the amplitude equation (3.44) in the standard form used in Refs. [64] and [65] by setting $\hat{A} = \sqrt{3}A$, $\hat{x} = \xi/2$, $\hat{y} = Y/\sqrt{2(1 + \beta)}$ and $\hat{t} = T$ and then dropping the hats. This gives

$$A_t = A + (1 + i\eta)A_{xx} + A_{yy} - |A|^2 A,\tag{3.46}$$

where $\eta \equiv 3\gamma/4$. Equation (3.46) is a special case of the ACGLE [64, 65]. If there is no dispersion, then $\gamma = 0$ and Eq. (3.46) reduces to the isotropic (real) Ginzburg-Landau equation.

3.5 Numerical simulations

We carry out numerical simulations of Eq. (3.8) on $x \in [-L, L]$, and of Eqs. (3.4) and (3.46) on the square domain $(x, y) \in [-L, L]^2$. To do so, we employ Fourier spectral methods with

periodic boundary conditions, coupled with the fourth order exponential time differencing Runge-Kutta method (ETDRK4). Implementations of this method can be found in Refs. [66] and [67], while full derivations of the method can be found in Refs. [68] and [69]. In all simulations in this paper, we employ a spatial grid with $N = 2048$ grid points in 1D and an $N \times N$ spatial grid with $N = 128$ in the 2D simulations unless otherwise noted. The time step in all cases is $\Delta t = 0.01$.

3.5.1 Simulations of the Dispersive Swift-Hohenberg Equation

Figure 3.1 shows results of simulations of the 1D equation of motion Eq. (3.8) and the corresponding power spectral densities (PSDs) at time $t = 100$ for $\mu = 0.1$ and selected values of γ . The initial conditions were low amplitude spatial white noise. The simulations suggest that as γ gets large, the solution tends to a sinusoidal form, in accord with the perturbation theory prediction.

The perturbation theory prediction (3.22) gives the amplitude as a function of the wave number k to order γ^{-1} . Figure 3.2 shows the relative error in Eq. (3.22), where the relative error is defined to be the absolute value of the difference between the measured and predicted values divided by their sum. Note that as γ increases, the relative error decreases and is less than 1% when $\gamma > 50$. Thus, Eq. (3.22) appears to hold in the limit $\gamma \rightarrow \infty$, as expected. The perturbation theory also predicts the phase velocity of the solution. In the simulations, the observed velocity was taken to be $\Delta\phi/(k\Delta t)$, where $\Delta\phi$ is the phase difference in u at two times separated by time Δt and k is the dominant wave number. Figure 3.3 compares the prediction given by Eq. (3.29) to the observed velocities determined from 100 simulations — one for each integer value of γ between zero and 99. The simulations were run until time $t = 100$ and the velocities were determined from the last two time steps. Figure 3.3 is another indication that the simulated results agree very well with perturbation theory.

Turning our attention to the 2D case, Fig. 3.4 shows the time evolution of solutions to Eq. (3.4) and their corresponding PSDs for three values of γ , namely $\gamma = 0, 10$ and 100 . In all three cases, $\mu = 1$. For the nonzero values of γ , the defects are stretched dislocations or seams which are obliquely oriented with respect to the x axis. The phase changes through $\pm 2\pi$ on a contour that

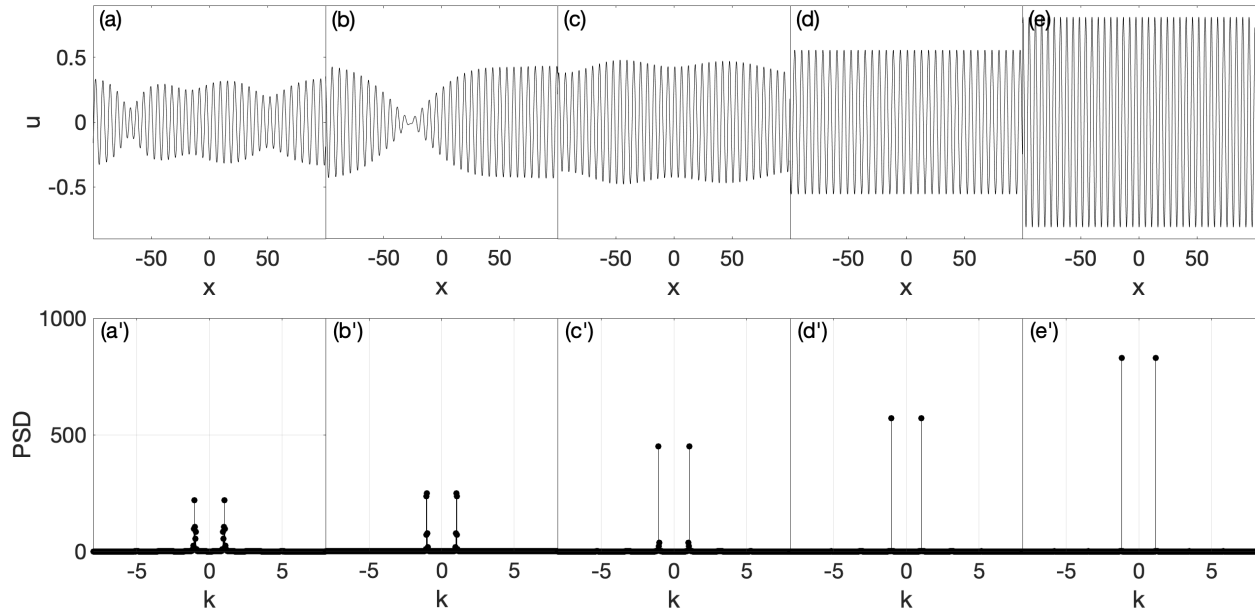


Figure 3.1: The first row depicts solutions to Eq. (3.8) on the spatial domain $x \in [-100, 100]$, and the second row shows the corresponding PSDs. In all cases, $\mu = 0.1$, which is near the threshold for pattern formation. From left to right, $\gamma = 0, 25, 50, 75$ and 100 . All images are for time $t = 100$.

circles a seam. Of particular note is the appearance of several seams at nearly the same y value but differing values of x . We call these defect chains. Figure 3.5 (a) shows a solution to Eq. (3.4) for a spatial white noise initial condition with a chain of three defects. These chains of seam defects are present at early times. At later times, defects of opposite sign meet and mutually annihilate, which ultimately results in a defect-free pattern. The two yellow horizontal reference lines in Fig. 3.5 (a) make it easy to see that the seams make a nonzero angle with the x axis.

Equation (3.4) is the Swift-Hohenberg equation for $\gamma = 0$. As the first two rows of Fig. 3.4 show, spatially extended defects are also present in the stripe pattern when γ is zero. However, in this case, the defects are not straight and are not obliquely oriented relative to the x axis; instead, they wind sinuously through the domain. Accordingly, the defects present for $\gamma = 0$ will not be referred to as seams.

The time evolution that occurs with relatively large γ in one and two dimensions is similar in several ways. In 2D, after some time, multiple roughly horizontal bands have formed in which u is almost independent of y , as seen in Fig. 3.5 (a). These bands are separated by chains of seam

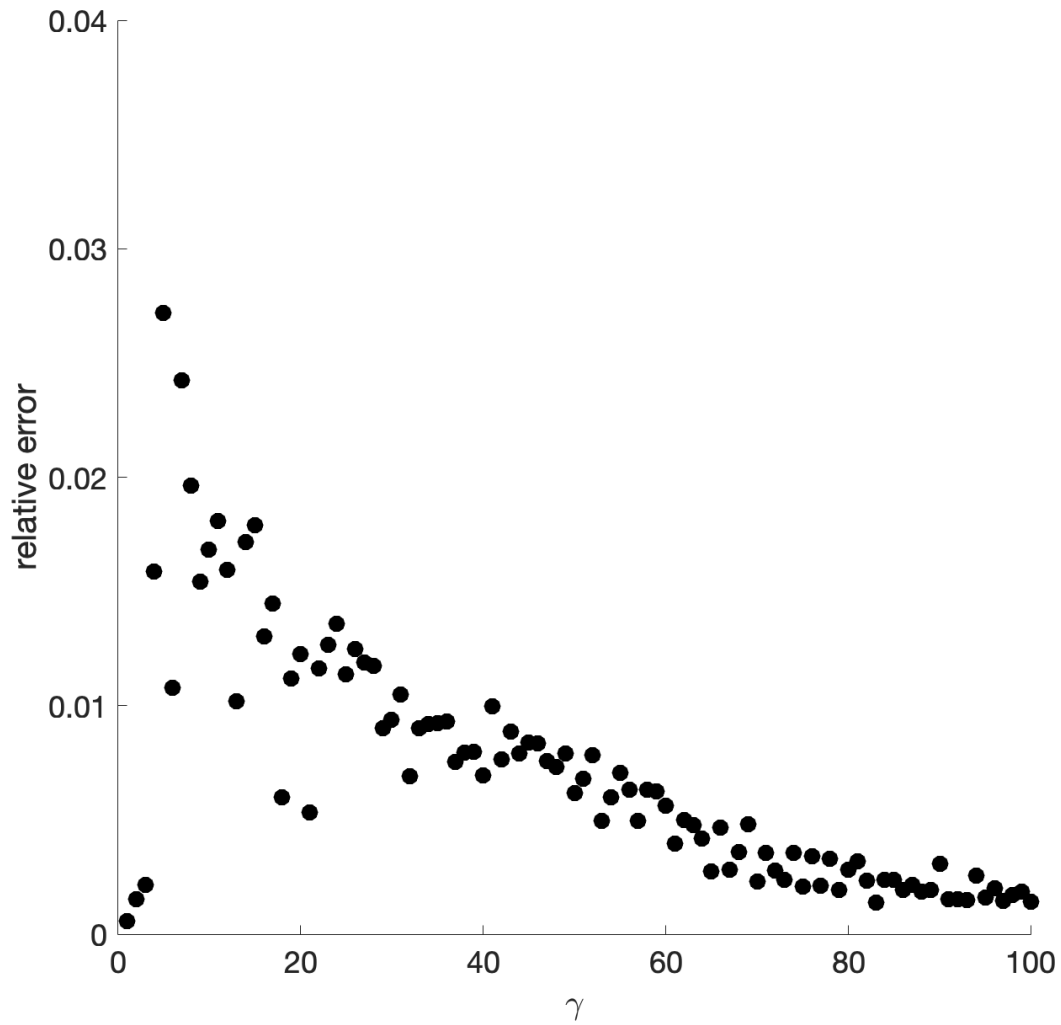


Figure 3.2: Comparison of Eq. (3.22) to simulation results for values of γ between 1 and 100. Each data point gives the relative error of the amplitude for the corresponding value of γ . In each simulation, $\mu = 1$, the domain was $x \in [-100, 100]$, and the measurements were taken at $t = 100$. We note that the relative error is less than 1% for values of γ larger than 50, and decreases as γ increases.

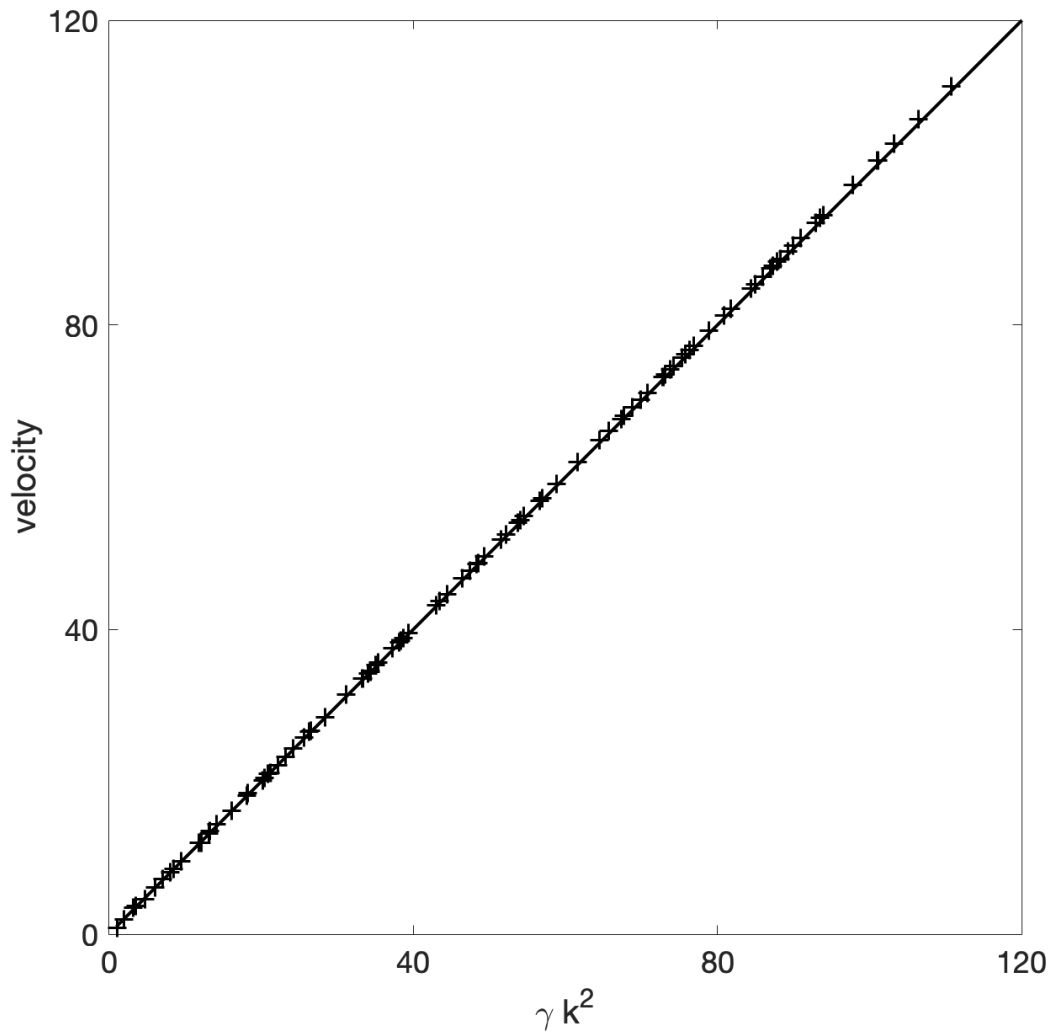


Figure 3.3: The phase velocity of the steady-state propagating solution versus γk^2 , as computed from numerical simulations (+'s). Each point is the result of a single simulation with $\mu = 1$ and a value of γ between 1 and 100. The solid line shows the theoretical prediction. The domain for each simulation was $x \in [-100, 100]$, and the velocities were calculated at time $t = 100$.

defects. Within a band, the form of the solution is close to a solution to the 1D DSHE, and so the phase velocity is approximately equal to γk^2 . Figure 3.6 shows the time evolution of a solution. Defects are present except at the latest time, $t = 1500$. For each of the cuts parallel to the x axis that are shown in Fig. 3.6 (a) - (d), the velocity in the x direction was computed and compared to Eq. (3.29). The results of this comparison are shown in Fig. 3.6 (a') - (d'). The agreement is very good at each of the four times shown in the figure, except where a cut passes directly through a seam.

With a spatial white noise initial condition, chains of seams appear in an unpredictable fashion and the disordered arrangement of defects makes it challenging to discern the underlying order in the dynamics. By choosing a different type of initial condition, we can produce defect chains in a controlled fashion that makes it easier to study them. In particular, we adopt an initial condition in which sinusoidal ripples of two different wave numbers k_1 and k_2 occupy horizontal bands and are in contact with one another: we set

$$u(x, y, 0) = \begin{cases} \cos(k_1 x) & \text{for } |y| < L/2 \text{ and } -L < x < L \\ \cos(k_2 x) & \text{for } |y| > L/2 \text{ and } -L < x < L. \end{cases} \quad (3.47)$$

The initial condition given by Eq. (3.47) must satisfy the periodic boundary conditions, and so we must have $k_i = \pi n_i / L$, where n_i is an integer and $i = 1$ and 2 . We also choose k_1 and k_2 to be within the range of linearly unstable wave numbers, i.e., $(1 - k_i^2)^2 < \mu$ for $i = 1$ and 2 . This requirement ensures that neither of the initial sinusoids has an amplitude that rapidly tends to zero as time passes. Figure 3.5 (b) shows the result of a simulation with this type of banded initial condition. Two defect chains have developed. Notice that the dislocations within a defect chain all have the same sign and are evenly spaced. In addition, the dislocations in the two chains have opposite signs, and will annihilate after some time; see Fig. 3.7. Furthermore, as γ increases, the length of the defects increases, but is restricted by the number of defects in the chain (see Figs. 3.8 and 3.9). Figure 3.9 (a) makes it particularly evident that the seams are oriented obliquely to the x axis.

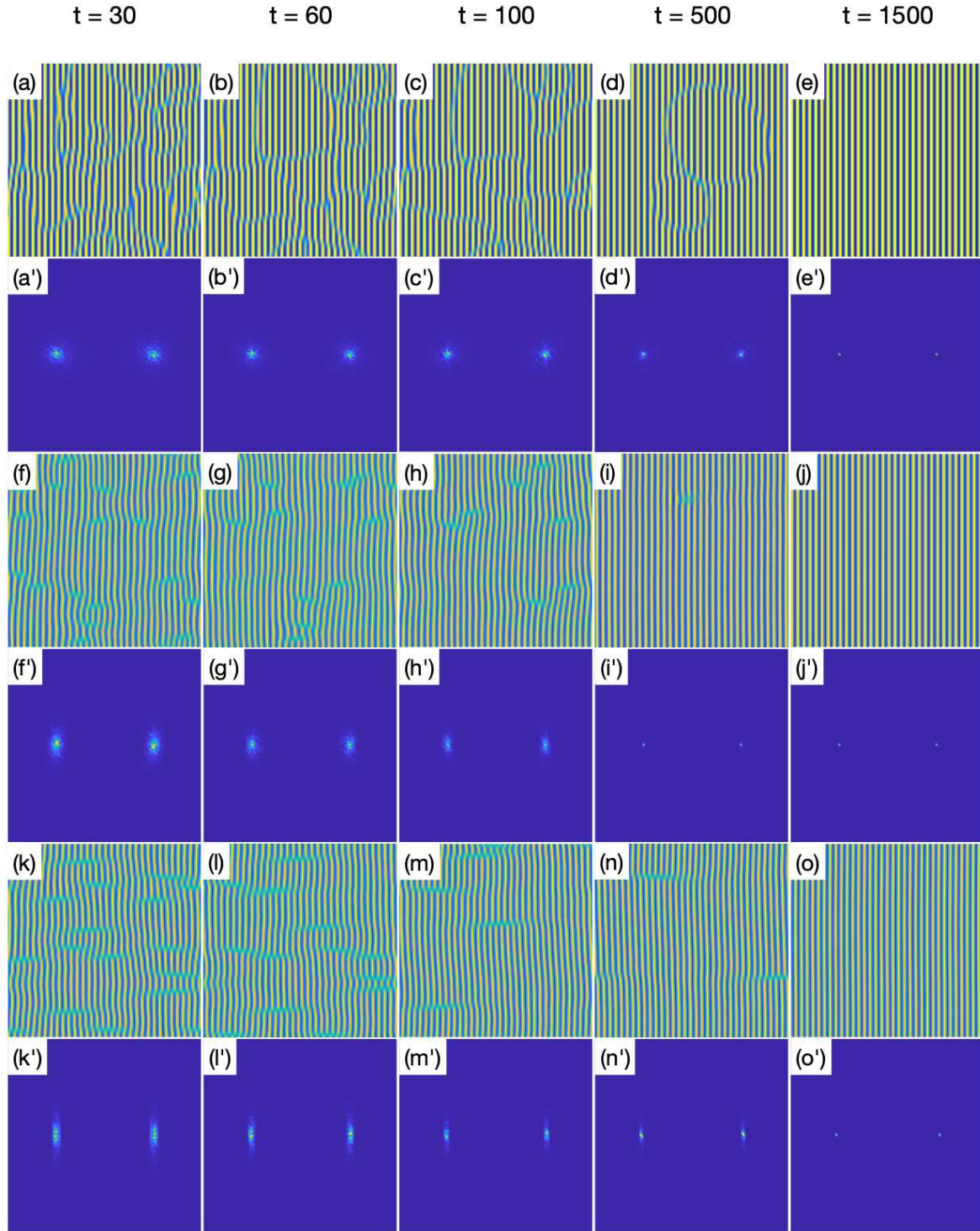


Figure 3.4: Solutions to Eq. (3.4) with parameters $\mu = \beta = 1$ on the domain $(x, y) \in [-100, 100]^2$. The values of γ are the 0, 10 and 100 for the first, second and third pairs of rows, respectively. In each pair of rows, the first row shows the solution at the times listed and the second row shows the corresponding PSDs. The columns from left to right depict the solutions at times $t = 30, 60, 100, 500$ and 1500.

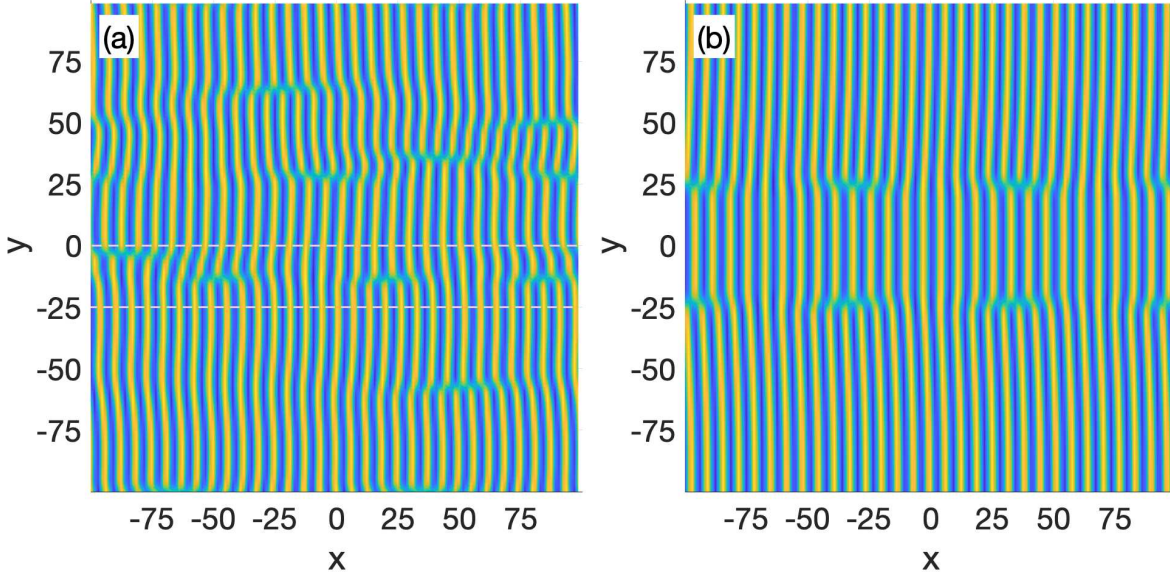


Figure 3.5: (a) A solution to Eq. (3.4) at time $t = 40$ that was started with a low amplitude spatial white noise initial condition. Note the chain of three defects between the horizontal lines. (b) A solution to Eq. (3.4) with a banded initial condition of the form (3.47) at time $t = 100$. The initial condition had $n_1 = 28$ and $n_2 = 31$. The parameter values were $\mu = \beta = 1$ and $\gamma = 100$ in both (a) and (b).

3.5.2 Simulations of the Amplitude Equation

Solutions of the 1D amplitude equation

$$A_t = A + (1 + i\eta)A_{xx} - |A|^2 A \quad (3.48)$$

behave in a fashion analogous to the solutions of the 1D DSHE (3.8). This is illustrated by the simulations of Eq. (3.48) shown in Fig. 3.10. The amplitude $|A|$ and phase ϕ are plotted as functions of x at time $t = 60$ for two simulations with $\eta = 10$ and 100 . For the larger value of η , the solution is close to a plane wave: as seen in panels (b) and (b') of the figure, the amplitude $|A|$ is almost a constant and the phase ϕ is close to being a linear function of x . The plane-wave solution is the analog of the highly ordered ripples seen in Fig. 3.1 for the larger values of γ . The solution shown for $\eta = 10$ still deviates significantly from a plane wave at time $t = 60$ but approaches such a solution at longer times.

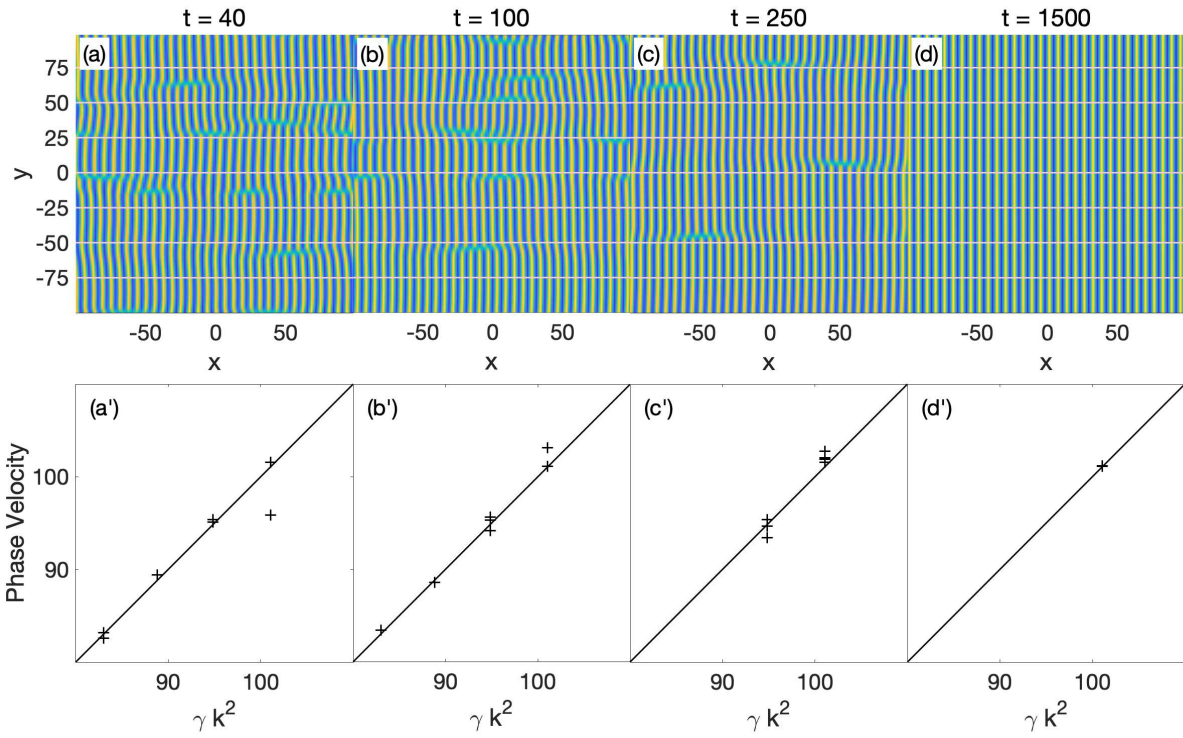


Figure 3.6: The time evolution of a solution to Eq. (3.4) with $\mu = \beta = 1$ and $\gamma = 100$ is shown in the first row. The domain is $(x, y) \in [-100, 100]^2$. The phase velocity in the x direction was computed for each of the cuts parallel to the x axis that are shown. The second row shows the observed velocities along each cut (+'s) versus the velocities predicted by Eq. (3.29) (solid lines).

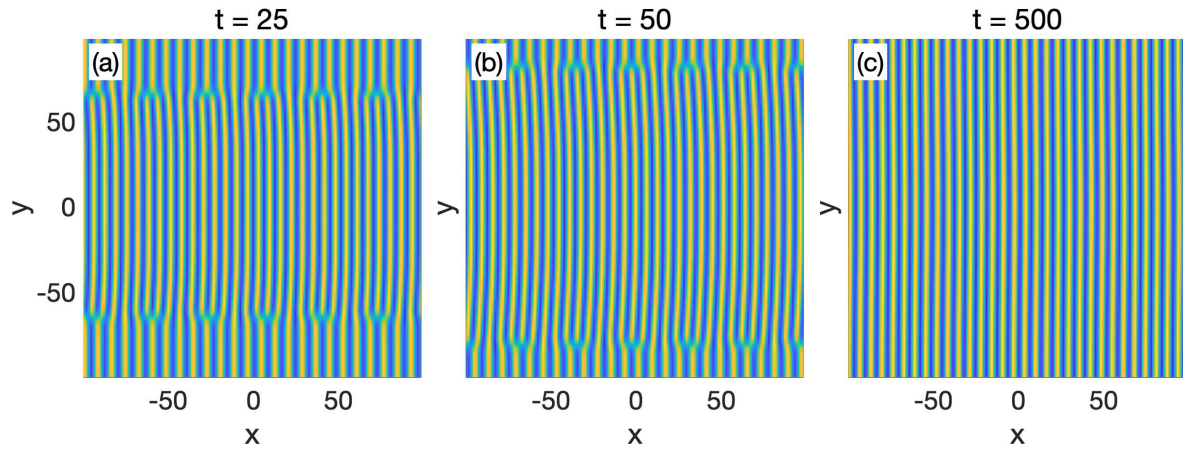


Figure 3.7: A solution to Eq. (3.4) with the parameter values $\mu = \beta = 1$ and $\gamma = 100$ on the domain $(x, y) \in [-100, 100]^2$ at times (a) $t = 25$, (b) $t = 50$ and (c) $t = 500$. The initial condition was given by Eq. (3.47) with k_1 and k_2 chosen so that $n_1 = 25$ and $n_2 = 31$.

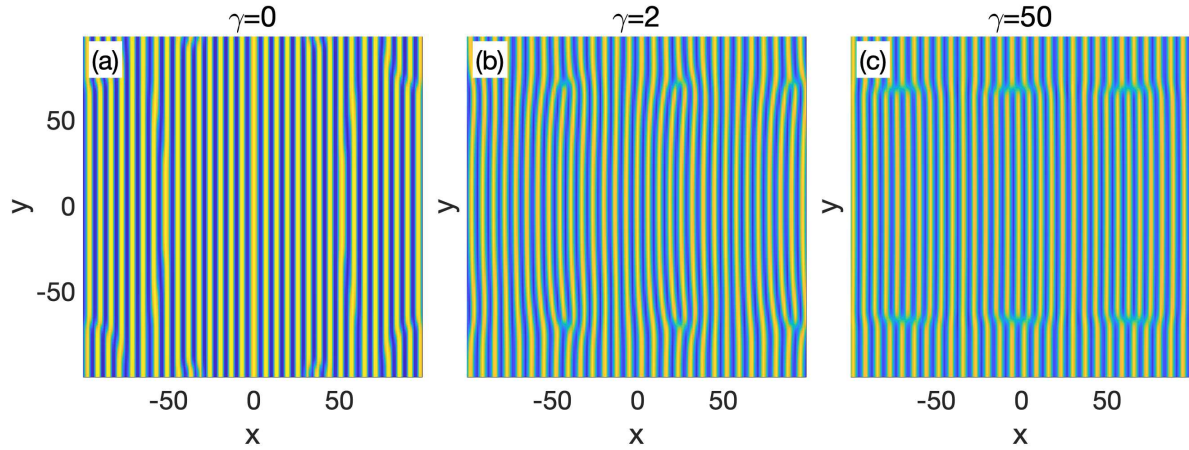


Figure 3.8: Solutions to Eq. (3.4) on the domain $(x, y) \in [-100, 100]^2$ are shown at time $t = 100$. The parameter values are $\mu = \beta = 1$ for each panel, and $\gamma = 0, 2,$ and 50 , as labelled. The initial conditions were given by Eq. (3.47) with k_1 and k_2 chosen so that $n_1 = 28$ and $n_2 = 31$. There are therefore $n_2 - n_1 = 3$ defects in each chain.

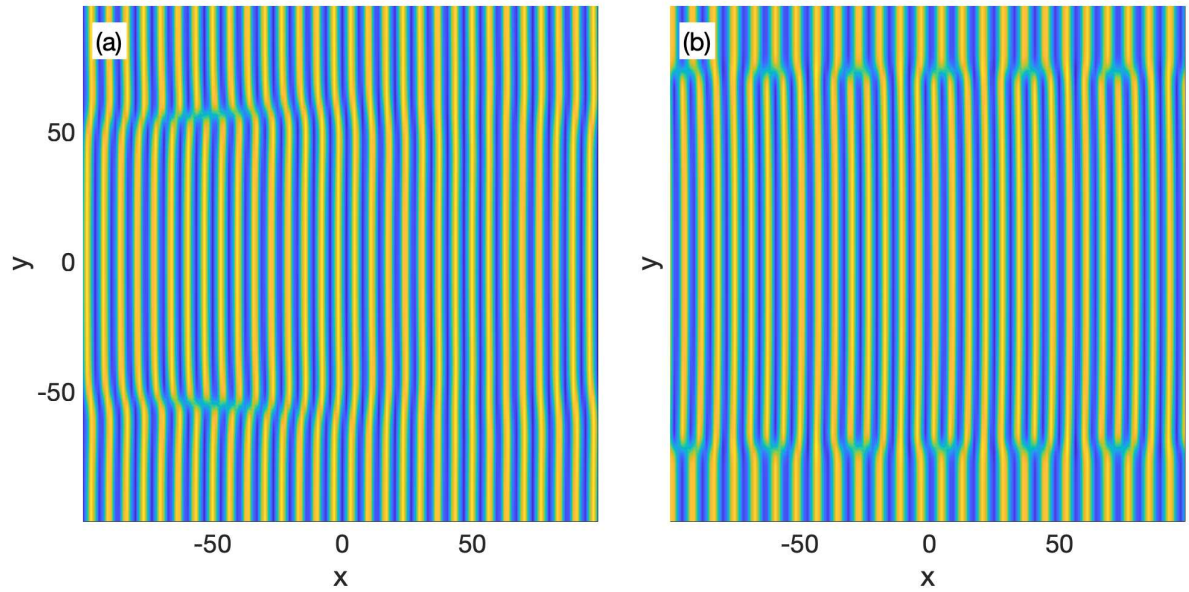


Figure 3.9: Solutions to Eq. (3.4) on the domain $(x, y) \in [-100, 100]^2$. The parameter values are $\mu = \beta = 1$ and $\gamma = 50$. The initial conditions were given by Eq. (3.47). Panel (a) shows a solution at time $t = 100$ with $n_1 = 31$ and $n_2 = 30$, and panel (b) shows a solution at time $t = 50$ with $n_1 = 31$ and $n_2 = 25$.

The analogy between the amplitude equation and the DSHE extends to 2D. Figure 3.11 shows simulations of Eq. (3.46) at different times for selected values of η . The initial condition in each case was low amplitude spatial white noise. For $\eta = 0$, Eq. (3.46) reduces to the much studied real Ginzburg-Landau equation.

For $\eta > 0$, the amplitude $|A|$ is depressed in elongated regions that are obliquely oriented relative to the x direction, as is seen most clearly by looking at the defects close to the upper and lower domain boundaries in Fig. 3.11 (f) - (j). The phase $\phi \equiv \text{Im}(\ln A)$ winds through $\pm 2\pi$ about each of these regions. These defects are the analogs of the seams in the DSHE and are spiral waves, as can be seen in panels (i') and (j') of Fig. 3.11, for example. The spiral waves are anisotropic, in contrast to the isotropic spiral waves produced by the (isotropic) complex Ginzburg-Landau equation. As we would expect based on our simulations of the DSHE, chains of spiral waves appear in the simulations of the ACGLE (3.46). These are most evident in Fig. 3.11 (k) - (o). For $\eta = 0$, the spiral waves reduce to vortices.

We can once again cause chains of defects to form in a controlled fashion using banded initial conditions. We begin by noting that there is a plane-wave solution to Eq. (3.46) of the form $A(x, y, t) = R_0 e^{i(qx - \omega t + \psi)}$, where $R_0^2 = 1 - q^2$, $\omega = \eta q^2$, and ψ is an arbitrary phase. We will study an initial condition that has two adjacent horizontal bands with different wave numbers q_1 and q_2 and phases $\psi_1 = \psi_2 = 0$:

$$A(x, y, 0) = \begin{cases} \sqrt{1 - q_1^2} e^{iq_1 x} & \text{for } |y| < L/2 \text{ and } -L < x < L \\ \sqrt{1 - q_2^2} e^{iq_2 x} & \text{for } |y| > L/2 \text{ and } -L < x < L. \end{cases} \quad (3.49)$$

The initial condition must satisfy the periodic boundary conditions, and so we must have $q_i = \pi n_i / L$, where n_i is an integer and $i = 1$ and 2 . Without loss of generality, we may assume that $n_2 > n_1$. Simulations with banded initial conditions show that two parallel chains of spiral waves form after a short time, as seen in Fig. 3.12 (a) and (b), for example.

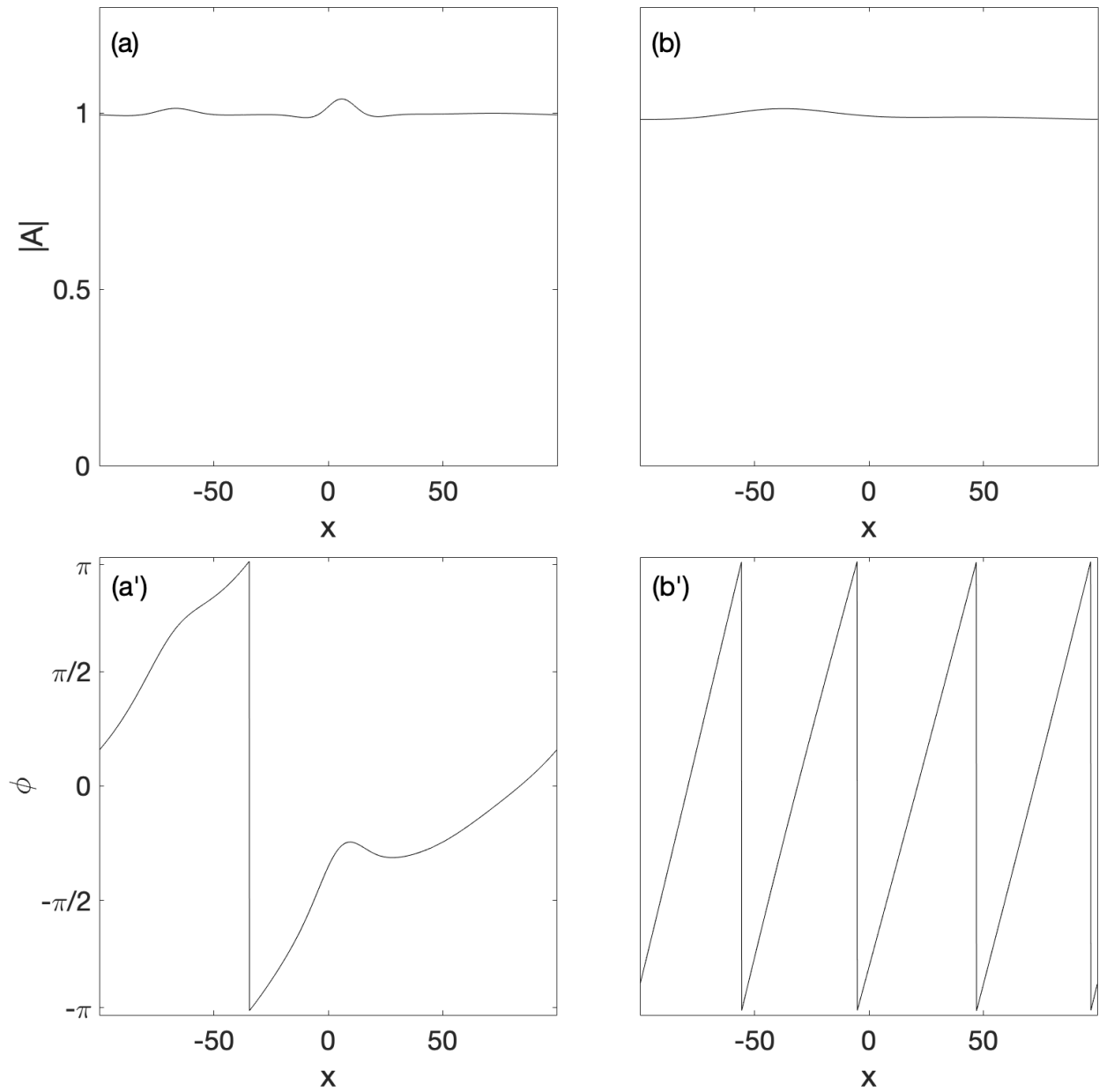


Figure 3.10: Two simulations of Eq. (3.48) starting from low amplitude spatial white noise initial conditions are shown at time $t = 60$. In panels (a) and (b), the amplitude $|A|$ is plotted as a function of x for $\eta = 10$ and 100, respectively. The corresponding phase ϕ is depicted in panels (a') and (b').

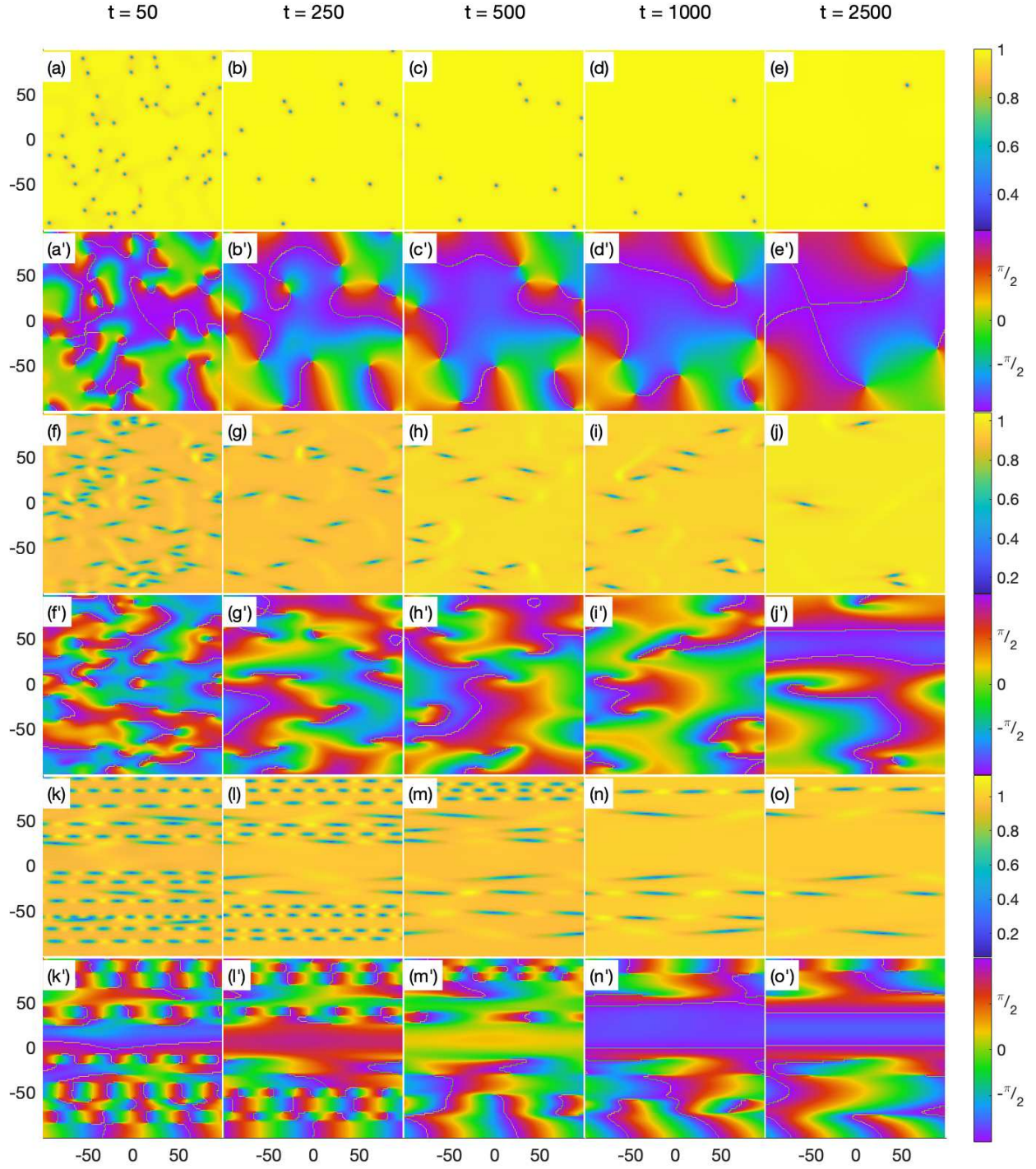


Figure 3.11: The time evolution of three simulations of Eq. (3.46) on the spatial domain $(x, y) \in [-100, 100]^2$. Rows (a)-(e), (f)-(j), and (k)-(o) show the magnitude of the solution $|A(x, y, t)|$ for $\eta = 0, 10$ and 100 , respectively. Rows (a')-(e'), (f')-(j'), and (k')-(o') show the corresponding phases $\phi(x, y, t)$. The solution at times $t = 50, 250, 500, 1000$ and 2500 is shown in columns 1 through 5, respectively.

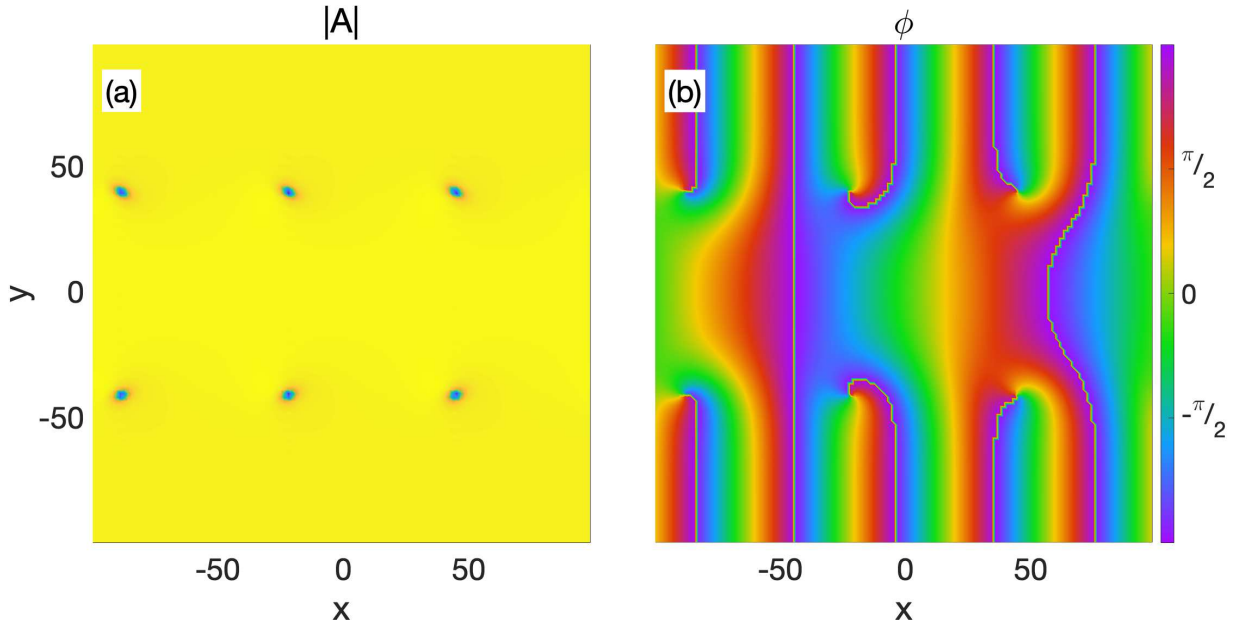


Figure 3.12: Chains of spiral waves created by simulating Eq. (3.46) with a banded initial condition of the form given by Eq. (3.49). The spatial domain was $(x, y) \in [-100, 100]^2$ and the snapshot was taken at $t = 100$. We set $\eta = 1$ and the wave numbers q_1 and q_2 were chosen so that $n_1 = 2$ and $n_2 = 5$.

If the plane waves simply propagated without changing their form, the solution to the ACGLE with the initial condition (3.49) would be

$$A(x, y, t) = \begin{cases} \sqrt{1 - q_1^2} e^{i(q_1 x - \omega_1 t)} & \text{for } |y| < L/2 \text{ and } -L < x < L \\ \sqrt{1 - q_2^2} e^{i(q_2 x - \omega_2 t)} & \text{for } |y| > L/2 \text{ and } -L < x < L, \end{cases} \quad (3.50)$$

where $\omega_i \equiv \eta q_i$ for $i = 1$ and 2 . This of course is not the solution to the initial value problem since the $A(x, y, t)$ given by Eq. (3.50) does not satisfy the ACGLE along the lines $y = \pm L/2$. Nevertheless, let us suppose for the moment that Eq. (3.50) were the solution. The defect cores would then appear at the locations $x = x_n$ where the phase difference between the two bands is 180° , i.e.,

$$q_1 x_n - \omega_1 t = q_2 x_n - \omega_2 t - (2n + 1)\pi \quad (3.51)$$

for $n \in \mathbb{Z}$. This would mean that

$$x_n = \frac{\omega_2 - \omega_1}{q_2 - q_1}t + \frac{(2n + 1)\pi}{q_2 - q_1}. \quad (3.52)$$

Equation (3.52) immediately gives us two results: the spiral wave velocity

$$\dot{x}_n = \frac{\omega_2 - \omega_1}{q_2 - q_1} = \eta(q_1 + q_2) \quad (3.53)$$

and the spacing between the cores of two adjacent spiral waves

$$\Delta x = x_{n+1} - x_n = \frac{2\pi}{q_2 - q_1}. \quad (3.54)$$

It is interesting to note that Eq. (3.53) implies that \dot{x}_n is the sum of the phase velocities of the two plane waves.

As we have noted, Eq. (3.50) does not really give the solution to the ACGLE with the banded initial condition. Instead, as time passes, the amplitude of the solution becomes depressed in the vicinity of the spiral wave cores and the lines of constant phase become curved, as Fig. 3.12 illustrates. However, the initial condition (3.49) is periodic in x with period Δx . As the solution to the ACGLE evolves in time, the solution remains periodic with this period. Equation (3.54) therefore gives the correct separation between the spiral wave cores. In addition, our simulations demonstrate that Eq. (3.53) gives a very good estimate of the spiral wave velocity, as we will now show.

We compared the velocity and spacing predictions given by Eqs. (3.53) and (3.54) with the results of numerical simulations with banded initial conditions. Simulations were carried out for $q_1 = 0$ and $q_2 = \pi n_2/L$, where $n_2 = 2, 3, 4, 5, 6$, and 7 . (We omitted the $n_2 = 1$ case because the spacing between defects is undefined if there is only one defect in a chain.) The simulations were performed for the parameter value $\eta = 100$ on the spatial domain $(x, y) \in [-100, 100]^2$ and were run up to time $t = 200$. The resulting defect velocities and spacings are compared with the

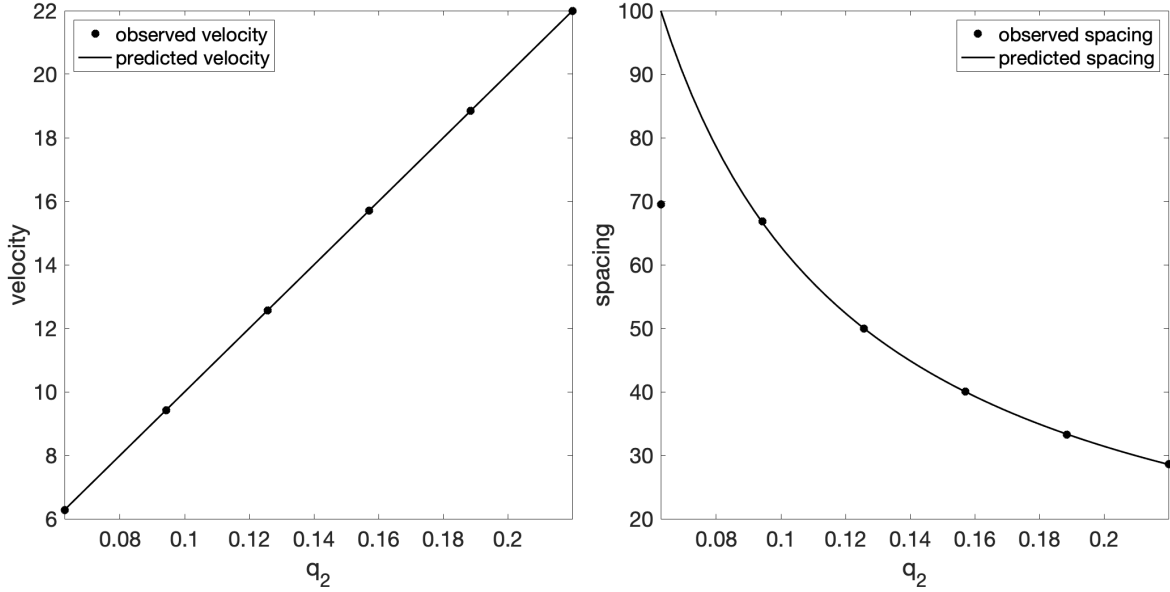


Figure 3.13: Simulations of Eq. (3.46) with banded initial conditions of the form given by Eq. (3.49) were carried out with q_1 fixed at zero and with $q_2 = \pi n_2/L$, where $n_2 = 2, 3, 4, 5,$ and 7 . The spatial domain was $(x, y) \in [-100, 100]^2$ and η was 100. The defect velocities and spacings were computed at $t = 200$. The observed values (dots) are compared to the values predicted by Eqs. (3.53) and (3.54) (solid curves).

predictions given by Eqs. (3.53) and (3.54) in Fig. 3.13 (a) and (b), respectively. The agreement is excellent, provided that η and $\Delta n \equiv n_2 - n_1$ are sufficiently large. If either η or Δn is too small, then the defects velocities oscillate in time. This is the reason for the discrepancy seen in the right panel of Fig. 3.13 for the case $n_2 = 2$.

A comparison of the regions of depressed amplitude $|A|$ obtained for $\eta = 10$ and 100 in Fig. 3.11 suggests that the angle ψ that the spiral wave cores make with the x axis decreases with η . To investigate this further, we defined a new function $\rho \equiv 1 - |A|^2$ within a neighborhood around a defect. We interpreted ρ as a “density,” and then found the moment of inertia tensor for this density distribution. The angle that the principal axis with the smallest principal moment makes with the x axis is the angle ψ . Figure 3.14 shows the value of ψ for a range of values of η . The results are for banded initial conditions with $q_1 = 0$ and $q_2 = n_2\pi/L$, where $n_2 = 2, 3$ and 4 . In addition, the values of ψ were averaged over all of the defects in a given simulation. Our results support the proposition that ψ is a decreasing function of η for given values of n_1 and n_2 . They also suggest that ψ is inversely proportional to η , and hence that ψ vanishes in the limit $\eta \rightarrow \infty$.

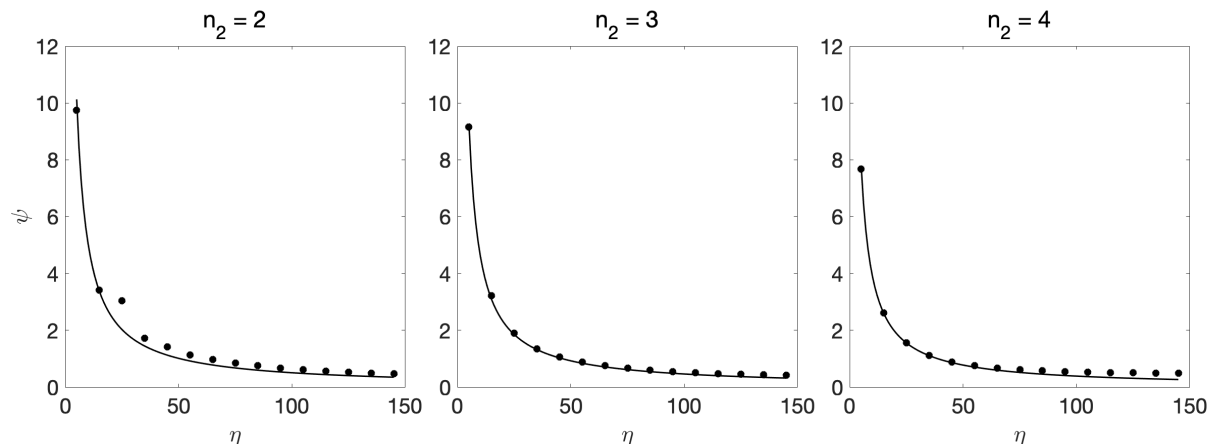


Figure 3.14: Simulations were run of Eq. (3.46) with initial conditions given by Eq. (3.49) on the spatial domain $(x, y) \in [-100, 100]^2$, and the average angle ψ that the defects made with the x -axis was computed. This was repeated for $\eta = 5, 10, \dots, 145$ and for $q_2 = n_2\pi/100$ with $n_2 = 2, 3$, and 4. In each case, $q_1 = 0$. Each data point represents the average angle obtained from a simulation, while the curve is a fit that is proportional to $1/\eta$. The constant of proportionality depends on Δn .

Figure 3.13 shows that the defect spacing depends on q_2 , and of course it depends on q_1 as well. If we take the limit in which both q_1 and q_2 tend to a common nonzero value q , then Δx tends to infinity according to Eq. (3.54). In this limit, the seams are in effect infinitely wide and they become parallel to the x axis. We found an exact solution of the ACGLE (3.46) that gives the form of the seams in this limit:

$$A(x, y, t) = \pm \sqrt{1 - q^2} e^{i(qx - \eta q^2 t)} \tanh \left(\sqrt{\frac{1 - q^2}{2}} y \right). \quad (3.55)$$

Equation (3.55) is a valid solution for any real q with magnitude smaller than 1. If we cross the seam described by Eq. (3.55) anywhere along its length, the phase ϕ changes by π . The amplitude is depressed around the x axis in a region with width proportional to $(1 - q^2)^{-1/2}$; this is the core of the seam.

3.6 Discussion

This study was motivated in part by a need to better understand the nanoscale patterns produced by ion bombardment of solid surfaces. Raised and depressed triangular regions that are

traversed by ripples are commonly observed in experiments, but the formation of these patterns is not currently understood. Simulations of the dispersive KS equation in 2D produce triangular nanostructures that strongly resemble those seen in experiments and show that dispersion plays an important role in their genesis [50]. This finding led us to study the DSHE in 2D.

Our work on the 2D DSHE suggests that the oblique sides of the triangular nanostructures might, in fact, be seams. We therefore examined the results of a numerical integration of the simplified anisotropic KS equation with linear dispersion, Eq. (3.2), and found that this is indeed the case. This is illustrated by Fig. 3.15. Our work therefore indicates that the notion that there are triangular nanostructures is misleading: Instead, the experimentally observed topographies are more properly thought of as ripples with a high density of seams.

The triangular structures found in simulations of the 2D dispersive KS equation are transient [50]. Because the surfaces display a high degree of disorder and the seams are abundant, it is challenging to discern how the so-called triangles disappear. Our simulations of the dispersive KS equation and the associated amplitude equation suggest that seams of opposite signs move toward one another and then annihilate, ultimately leaving a surface without triangular nanostructures.

There are admittedly important differences between the dispersive KS equation and the DSHE in 2D. The ripples are more orderly and the seams are more widely separated from one another in the case of the DSHE, for example. In addition, the anisotropic SHE we studied produces ripples with a high degree of order even in the absence of linear dispersion; in contrast, solutions of the anisotropic KS equation exhibit spatiotemporal chaos, and strong linear dispersion is needed to suppress this and to produce highly ordered ripples. However, we exploited another key difference to our advantage. The DSHE has small regions of unstable wave vectors near threshold which allowed us to derive the associated amplitude equation. This is not possible in the case of the dispersive KS equation because there are unstable modes with arbitrarily long wavelengths. Stated more succinctly, the instability is of Type I in the case of the DSHE but is of Type II in the case of the DKSE [63].

It should be mentioned that the 1D DSHE (3.8) with the quadratic nonlinearity $2u^2$ appended to the right-hand side has previously been studied [70]. The emphasis was on the propagation of fronts and on finding localized states for small γ , however. In our work, we did not touch on those topics and considered only the case in which no quadratic nonlinearity appears in the equation of motion (3.8). We also placed special emphasis on the limit in which the dispersive coefficient γ is large [71].

Chains of spiral waves that appear in simulations of the ACGLE have been studied by Faller and Kramer [65]. Those authors had to carefully adjust the parameters in the ACGLE in order to get chains to form. They also had difficulty getting chains of defects to form starting with spatial white noise initial conditions. In this paper, we studied the special case of the ACGLE in which the coefficients of the terms proportional to A_{yy} and $|A|^2A$ are real. In this case, chains of spiral waves form readily with a spatial white noise initial condition if linear dispersion is sufficiently strong. We also established that chains of spiral waves can easily be produced in a controlled fashion using banded initial conditions. This led us to a prediction of the spacing and velocity of the defects in a chain, and this prediction agrees well with our simulations.

3.7 Conclusions

Spatially extended dislocations were shown in this paper to appear in simulations of the 2D dispersive Swift-Hohenberg equation. These defects, which we call seams, tend to organize themselves into ordered chains. The presence of a narrow band of unstable wavelengths in the DSHE allowed us to make analytical progress towards understanding seam defects. We studied the DSHE in two limits. First, close to threshold, we derived an amplitude equation for the DSHE, which turns out to be a special case of the ACGLE. In this limit, seam defects correspond to spiral waves in the ACGLE. Numerical simulations confirm analytical formulas for the distance between spiral wave cores and their velocities. The second limit was that of large dispersion. A perturbative analysis in this case yielded the propagation velocities of ripple patterns and a relationship between their amplitudes and wavelengths. Our results shed light on the effect dispersion has on the

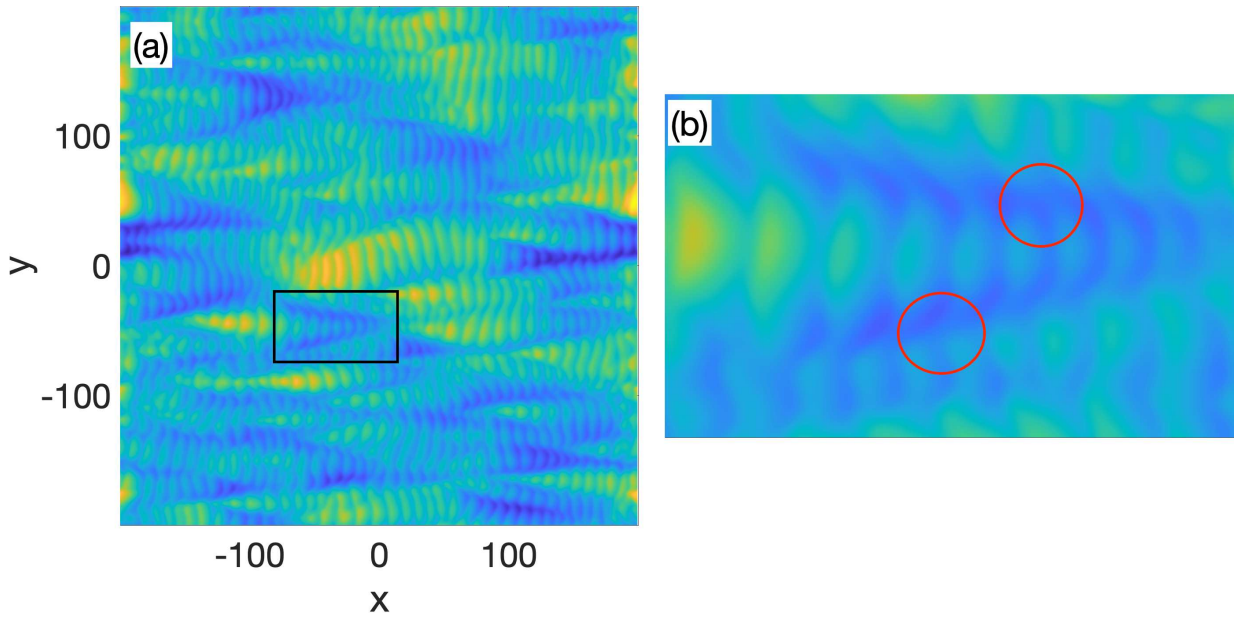


Figure 3.15: (a) A simulation of Eq. (3.2) for $\gamma = 5$ at time $t = 65$ that shows the raised and depressed triangular regions traversed by ripples. The initial condition was low amplitude spatial white noise. We employed an 512×512 spatial grid and a time step of $\Delta t = 0.01$. (b) An enlargement of the portion of panel (a) that is outlined in black. The dislocation cores within two seams are circled.

nanoscale patterns produced by ion bombardment of solid surfaces. In a more general context, our work can be viewed as a first step towards developing a comprehensive understanding of the effects of dispersion on pattern formation in two dimensions.

Chapter 4

Topological Measure of Order⁹

4.1 Introduction

In the study of non-equilibrium pattern forming systems and molecular simulations with periodic boundary conditions, the detection of order is crucial. Ordered patterns emerge when the maxima align themselves in a lattice-like formation. To quantify this order, various measures can be defined. In this text, we explore different measures of order and their applications.

In Section 4.2, we introduce persistent homology and the Delaunay triangulation, as well as the Wasserstein metric as tools for a topological and geometric measures of order. These techniques have been used to characterize the orderliness of lattices in the plane [72, 73]. These topological and geometric methods together with the Wasserstein distance function will allow us to quantify the amount of (dis)order in a lattice pattern.

We compute the necessary data- both topologically and geometrically- on ideal lattices in Section 4.3. We show in detail the calculation of the Vietoris-Rips complex for SC, FCC and BCC lattices, and their persistence diagrams. We also show the Delaunay triangulations of each of these ideal lattices, and their corresponding edge length distributions, and their pairwise angle distributions. These data are used to define measures of order with respect to the ideal cases.

In Section 4.4, we show how the measures of order change when the data being measured is perturbed. This demonstrates the continuity of these measures, which is vital since noise in the data should correlate to noise in the measures of order. We also observe interesting phenomena in the topological measures of order, which turn out to be useful in identifying the onset of a perfect pattern.

Section 4.5 focuses on pattern formation in three dimensions, which occurs naturally in biological morphogenesis, materials science, and fluid dynamics. Modeling three-dimensional lattice pat-

⁹This project is with Patrick Shipman and Mark Bradley. It is to be published.

terns using partial differential equations (PDEs) presents challenges due to the complex bifurcation diagrams. Standard approaches involve perturbing known analytic solutions and using numerical PDE solvers to arrive at perfect patterns. We present two methods to produce three-dimensional lattice patterns from low amplitude white-noise initial conditions- namely, by introducing an linearly dispersive term, or by adding a forcing term to the system. The topological measure of order is used to quantify the patterns' orderliness.

We make concluding remarks on the forced Swift-Hohenberg equation in Section ?? and the time evolution of the topological measure of order. Finally, in Section 3.6, we discuss several open problems encountered as this project nucleated into being.

Overall, this chapter provides an overview of measures of order and their applications in characterizing lattice patterns in non-equilibrium systems and molecular simulations. The presented techniques offer insights into the orderliness of patterns in different dimensions, contributing to the understanding of complex pattern formation.

4.2 Measures of order

In the case of non equilibrium pattern forming systems (or in molecular simulations) with periodic boundary conditions, order can be detected by the location of maxima alone- provided there is no spatial temporal chaos. Indeed, lattice like patterns can be modelled given carefully chosen parameters so that the maxima have a propensity to align themselves, hence ordered patterns emerge. We can exploit this fact, and define a measure of order (MoO) with respect to a given lattice. In this section, we aim to describe several measures of order.

4.2.1 Persistent Homology and the Wasserstein Metric

We draw inspiration from [72] and [73] expand on a topological MoO to three dimensional patterns. In [72], persistent homology (PH) was used to characterize the orderliness of hexagonal lattices via variance of the H_0 data, and the sum of the H_1 data that is encoded in a persistence diagram (PD). In [73], these techniques were expanded to include other lattices in the plane. This

was done with the Wasserstein distance between the PDs of an ideal lattice and those of a nearly ideal lattice obtained from solving non-equilibrium pattern-forming systems.

Techniques from computational topology will be particularly useful for studying patterns in dimensions three and higher. Let X be a point cloud in \mathbb{R}^n , and let $d(_, _)$ be a metric. We may define a filtration, S_r , called the Vietoris Rips (VR) Complex in the following way:

- the points in S_0 are the the points of X .
- for each $x \in X$, define the ball $B_r(x)$ of radius r , and let r vary. Here r is the filtration index.
- for $x, y \in X$, if $d(x, y) \leq r$, we include the edge between x and y in the filtration S_r .
- we include an n -simplex in S_r if all of its edges are included.

The first rows of Figs. 4.1, 4.2, and 4.3 show this process for small portions of ideal simple cubic (SC), face centered cubic (FCC) and body centered cubic (BCC) lattices respectively. This construction allows us to associate a X to a collection of discrete distributions, μ_X^k , with $k = 0, 1, \dots, n - 1$ by keeping track of the filtration values at which simplices are added. Further, these distributions mark the change of topological features and are hence known as birth-death diagrams, or persistence diagrams (PDs) The second rows of Figs. 4.1, 4.2, and 4.3 show the PDs of the ideal SC, FCC and BCC lattices respectively. An important addition to each PD is the inclusion of the diagonal Δ , in which each point has infinite multiplicity. This allows us to 1. compare PDs of different sizes and 2. to quantify noise.

We can then define a MoO via the Wasserstein metric $D(\mu_L, _)$. Thus, if X is a nearly ordered point cloud (representing a disordered system), we may define its MoO relative to L by

$$D(\mu_L, \mu_X) = \inf_{\eta} \sum_{u \in \mu_L} \|u - \eta(u)\|_1, \quad (4.1)$$

where the infimum is taken over all bijections from the points of μ_L (including the diagonal) to those of μ_X . This metric can be likened to moving piles of sand from one position to another,

and as such is often called the 'Earth Mover's Distance.' By taking this measure of order in each dimension, we define a vector of MoOs

$$m_L^k(X) = D(\mu_L^k, \mu_X^k), \quad (4.2)$$

where $k = 0, 1, \dots, n - 1$.

The MoOs defined in this way enjoy several nice properties:

1. invariance under $E(3)$ transformations, so the point cloud and ideal lattice do not need to be lined up to be compared
2. X and L do not have to contain the same number of points. Imperfect configurations are not required to have the same integral number of points an ideal lattice has.
3. two points close together in X (noise) result in topological noise (or transient features) which result in points near the diagonal on the persistence diagram- which add small contributions to the MoO under the Wasserstein metric.

See [74] for more details on persistent homology and the Wasserstein metric.

In practice, we use the sliced Wasserstein metric to approximate $D(_, _)$ [75]. The idea behind this approximation is the following: given two PDs, say μ and μ' , and a line $l(\theta)$ through the origin that makes an angle θ with respect to the x -axis, for each $u \in \mu$ we project u onto $l(\theta)$, (similarly for each $u' \in \mu'$). These give new 'flattened' PDs, which we call μ_θ and μ'_θ . Both μ_θ and μ'_θ are one dimensional distributions, for which there Wasserstein distance is merely

$$D(\mu_\theta, \mu'_\theta) = \inf_{\eta} \sum_{u \in \mu_\theta} \|u - \eta(u)\|, \quad (4.3)$$

where the infimum can be taken care of by sorting the elements of μ_θ and μ'_θ in ascending order, and computing the 1-norm. This can be done for every $\theta \in [0, \pi]$, so that

$$SW(\mu, \mu') = \frac{1}{\pi} \int_0^\pi D(\mu_\theta, \mu'_\theta) d\theta. \quad (4.4)$$

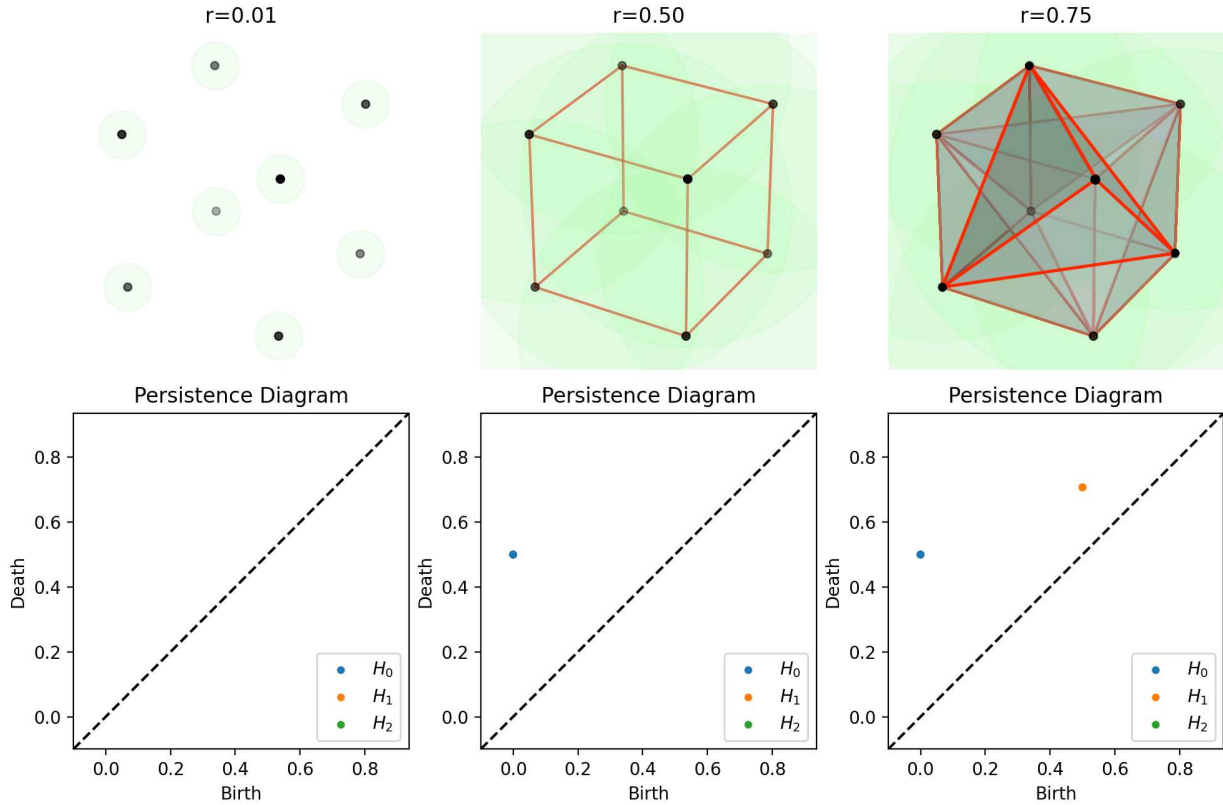


Figure 4.1: The VR complex of an SC cell whose side lengths are $1/2$. Filtration values of $r = .1, .5$ and $.75$ are shown to capture the different stages the VR complex undergoes. The highlighted edges show a tetrahedron in the center of the cell that kills the H_1 data, and also prevents any H_2 data from being formed.

The above integral can be approximated by the mean of $D(\mu_\theta, \mu'_\theta)$ for some sample of θ 's.

4.2.2 Delaunay Triangulation

Delaunay triangulations (DTs) have been used to define a measure of order for hexagonal lattices [72, 76], in which the measures of order are closely related to the first coordination number (or number of nearest neighbors) and the average distance between vertices. The order parameters defined rely on a property unique to hexagonal lattices- namely all points are equidistant from one another (thus the coordination number is readily available from the DT). These properties do not carry over into lattices in higher dimensions since 1. the edge lengths vary and 2. since vertices may have different numbers of neighbors. See Fig. 4.4. In this section, we briefly introduce the

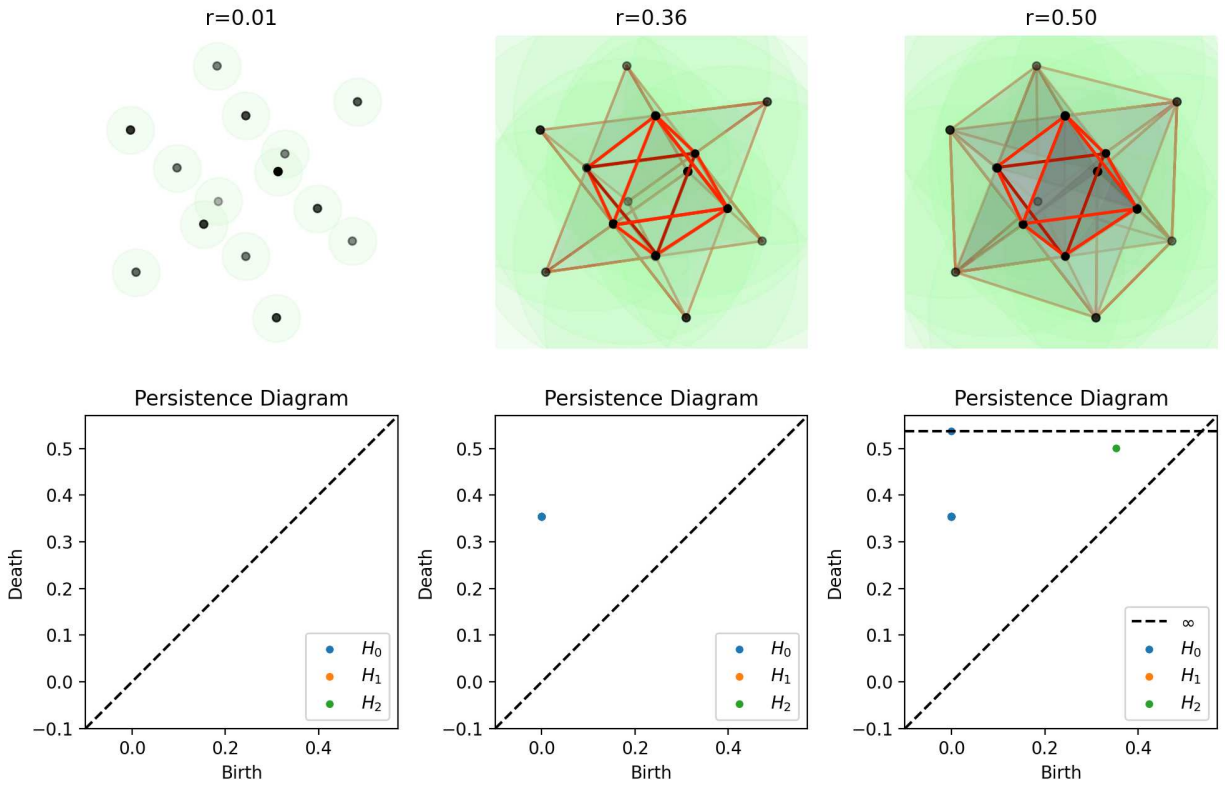


Figure 4.2: The VR complex of an FCC cell whose side lengths are $1/2$. Filtration values of $r = .1, .36$ and $.5$ show the different topologies of the FCC VR complex. The highlighted edges are the edges of the octahedron at the center, which begets the H_2 data.

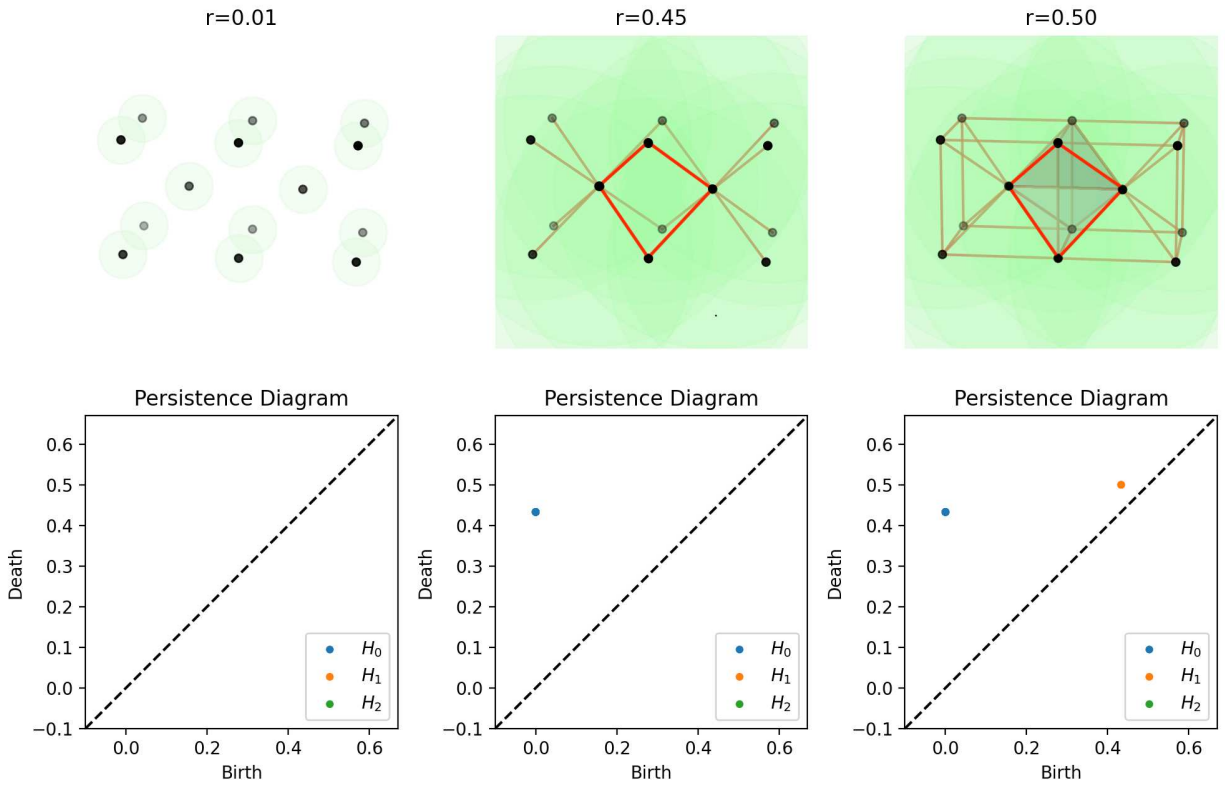


Figure 4.3: The VR complex of two BCC cells whose side lengths are $1/2$. Filtration values of $r = .1, .45$ and $.5$ show the different stages of the VR complex of the BCC lattice. The highlighted edges show one of the loops that is formed, and eventually dies. There are three others- one around each edge that is shared between the two cells of the lattice.

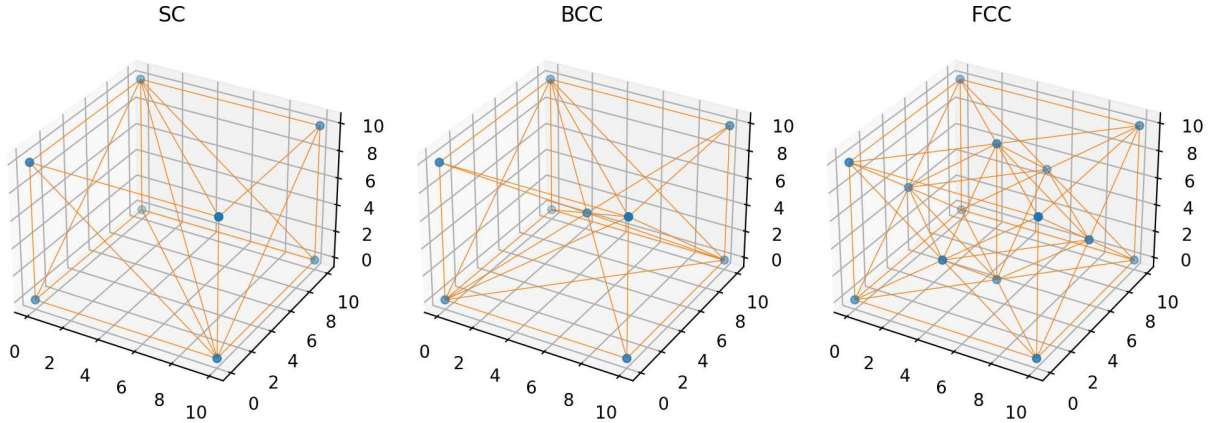


Figure 4.4: Delaunay triangulation of single cell for SC, BCC and FCC lattices. Note that the number of neighbors differs between vertices. Thus the coordination number of 3D lattices are not immediately obvious.

notion of the DT, and we outline the details of an extension to the DT measure of order that is suitable for more general lattices.

In order to obtain a DT, we begin with a Voronoi tessellation. Let X be a set of points in \mathbb{R}^n and let $d(_, _)$ be a metric. For $x \in X$, define the region V_x of points in \mathbb{R}^n that are closer to x than any other point in X . Explicitly, $V_x = \{u \in \mathbb{R}^n | d(x, u) < d(y, u) \text{ for } y \in X, x \neq y\}$. A Voronoi tessellation is then the union of all such V_x for $x \in X$. A DT is a triangulation whose vertices are the points $x \in X$ and whose edges are perpendicular to the boundaries of each region V_x of the tessellation. That is, the DT is dual to the Voronoi tessellation. The text [77] contains more details on Voronoi tessellations and Delaunay triangulations.

Given an ideal lattice L , we can define a measure of order of X with respect to L in the following way: we first find the DTs of both X and L , and calculate the edge lengths. We then define the distributions of edge lengths e_L and e_X , respectively. A suitable measure of order can then be defined by

$$m_L^e(X) = D(e_L, e_X), \quad (4.5)$$

where, once again $D(_, _)$ is the Wasserstein distance of distributions. Since lattices in \mathbb{R}^3 are characterized by their edge lengths and the angles between faces in each cell, we can define the

additional measure of order by finding the distributions of angles found in the triangulation (*i.e.* the angles found in each triangle that appears in the DT), θ_X and θ_L , and define

$$m_L^\theta(X) = D(\theta_L, \theta_X). \quad (4.6)$$

When working with the DT measure of orders on finite subsets of lattices, the boundaries often contain distorted simplices, which in turn yield outliers in the distributional data. Thus we ignore the boundary when necessary.

The MoOs defined via DTs have similar properties as those of the PH flavor- namely:

1. invariance under $E(3)$ transformations
2. X and L do not have to contain the same number of points
3. two points close together in X (noise) result in small edge lengths, or noise in the edge distributions. These are once again detected as noise in the Wasserstein metric between distributions.

One could equally well define a measure of order using the distance distribution of the lattices and point clouds. It is worth noting that in the case of ideal lattices, the edge length distributions are in some sense more distinguishable than the collection of all pairwise distances (Fig. 4.5). Indeed, using the distance distribution would enjoy all of the aforementioned properties as well.

4.3 A note on ideal lattices

In this section, we look at ideal lattices, which are necessary to define our MoOs. The top row of Figure 4.6 shows the persistence diagrams of three ideal Bravais lattices, generated on the domain $[0, 10]^3$, each containing 64 cells. It is important to note that increasing the number of cells only increases the frequency (or multiplicity) of each distribution μ_L^k , $k = 0, 1, 2$, and the size of the domain varies the scale of the lattice parameter, but otherwise the PD looks the same.

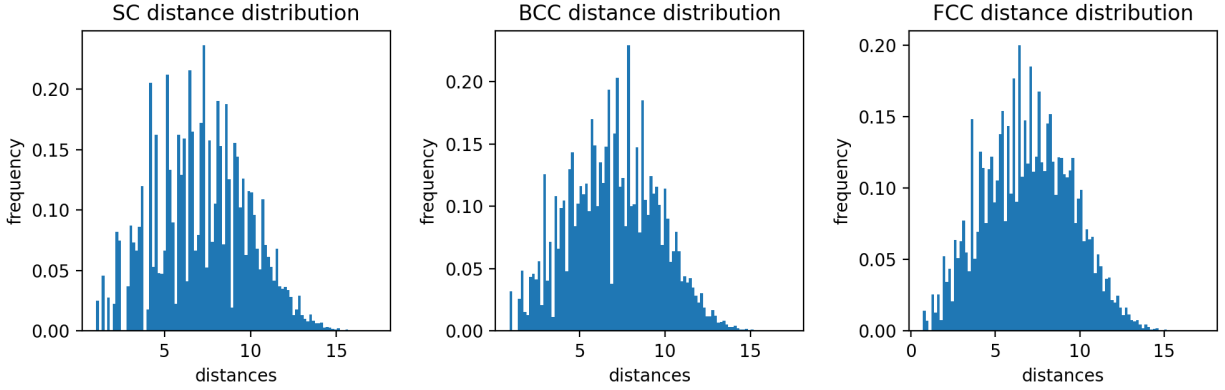


Figure 4.5: The distance distributions of ideal lattices on the domain $[0, 10]^3$ with 10 unit cells. The DT edge length distributions are more distinguishable and are depicted in the first row of Fig. 4.7.

It is also interesting to note that SC and BCC lattices contain no H_2 data, while FCC lattices contain no H_1 data. This can readily be seen. Let a denote the width of a unit cell in each case. For the SC lattice, note that when the filtration value r reaches a , edges are added between each vertex, which is the source of the H_1 data, and the filtration becomes a single connected component. When the filtration value reaches $r = a\sqrt{2}$, edges are added along the diagonal on the faces of the unit cell. In particular, a tetrahedron whose edges may be placed along these diagonals is added to the center of the cube, thus filling the volume, so there is no H_2 data in the SC lattices. Figure 4.1 shows the VR complex and persistence diagrams for different filtration values on a single cell of an SC lattice.

In the case of the FCC lattice, when the filtration value reaches $r = a/\sqrt{2}$, edges are added between the vertex on the face, and the neighboring corners of the unit cell, as well as an edge between neighboring face vertices. Thus at each corner of the unit cell, there is a tetrahedron. Then the center of the cell, remains an octahedron whose vertices lie at the center of each face of a cube, which is the source of H_2 data. The center is filled when the filtration value reaches the width a . See Fig. 4.2 for a depiction of the VR complex for one cell of an FCC lattice, and the corresponding persistence diagrams at a few filtration values.

A single unit cell of a BCC lattice only shows H_0 data— so to see H_1 , we must consider two adjacent cells. When the filtration value reaches $r = \sqrt{3}/2a$, edges are added between the center

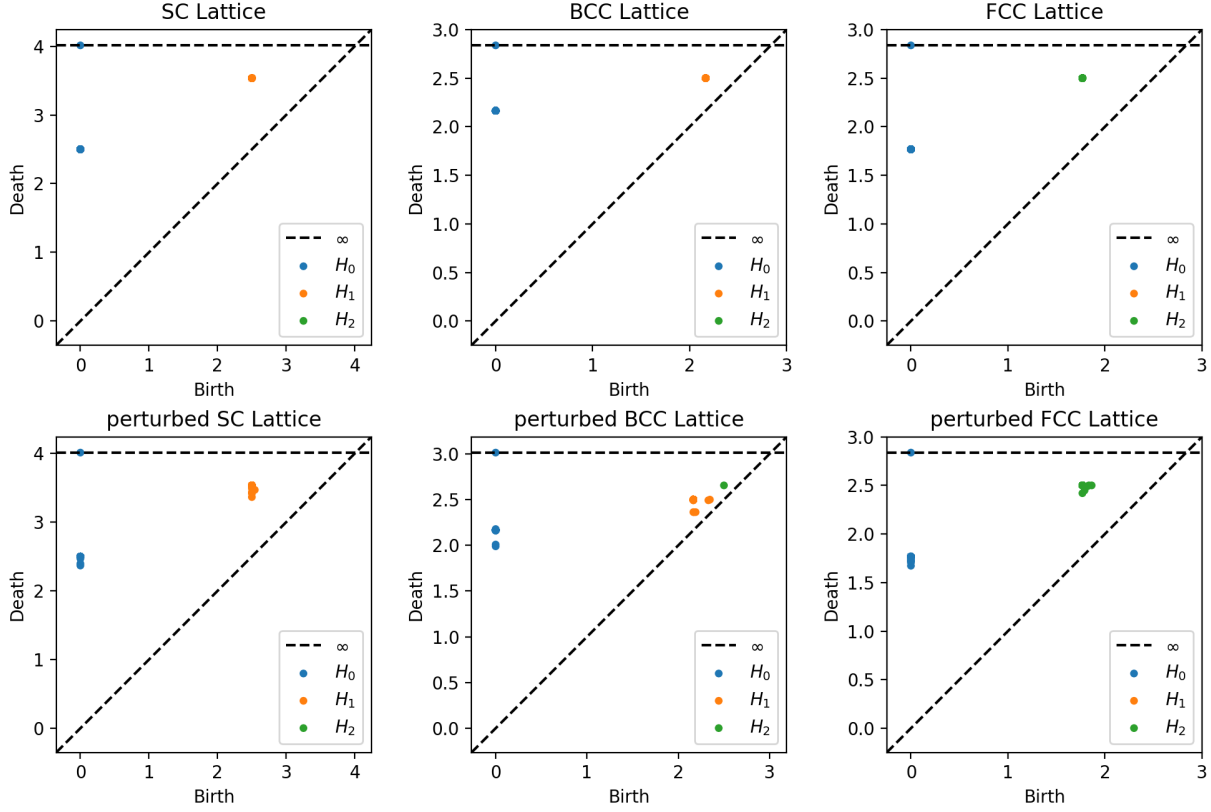


Figure 4.6: (Top row) From left to right, are the persistence diagrams of ideal SC, BCC and FCC lattices. It is interesting to note that SC and BCC have no H_2 data while the FCC lattice has no H_1 data. (Bottom row) The PDs of an ideal Bravais lattice with a randomly selected single point perturbed. The measures of order (written as $(m_L^0(L_p), m_L^1(L_p), m_L^2(L_p))$) are about SC: (0.2328, 0.4253, 0.0), BCC: (0.4407, 0.4152, 0.1367) and FCC: (0.4614, 0.0487, 0.48).

vertex and the neighboring vertices at the corners of the cube (this is true for both cells). Indeed, four loops are formed between the two cells, where each loop contains the two center vertices, and two of the corner vertices, and wraps around a single shared edge between two cubes. When the filtration value reaches $r = a$, edges are added between neighboring corners, and an edge is added between the two centers, thus filling the filtration with simplices which mean there is no H_2 data. Figure 4.3 shows this VR complex and the persistence diagrams for two adjacent cells of a BCC lattice.

To close this section, we present the distributional data from DTs of ideal lattices. The edges present in the distributions are straightforward to see— they are just the distances between neighboring vertices. The DTs of unit cells are shown in Fig. 4.4.

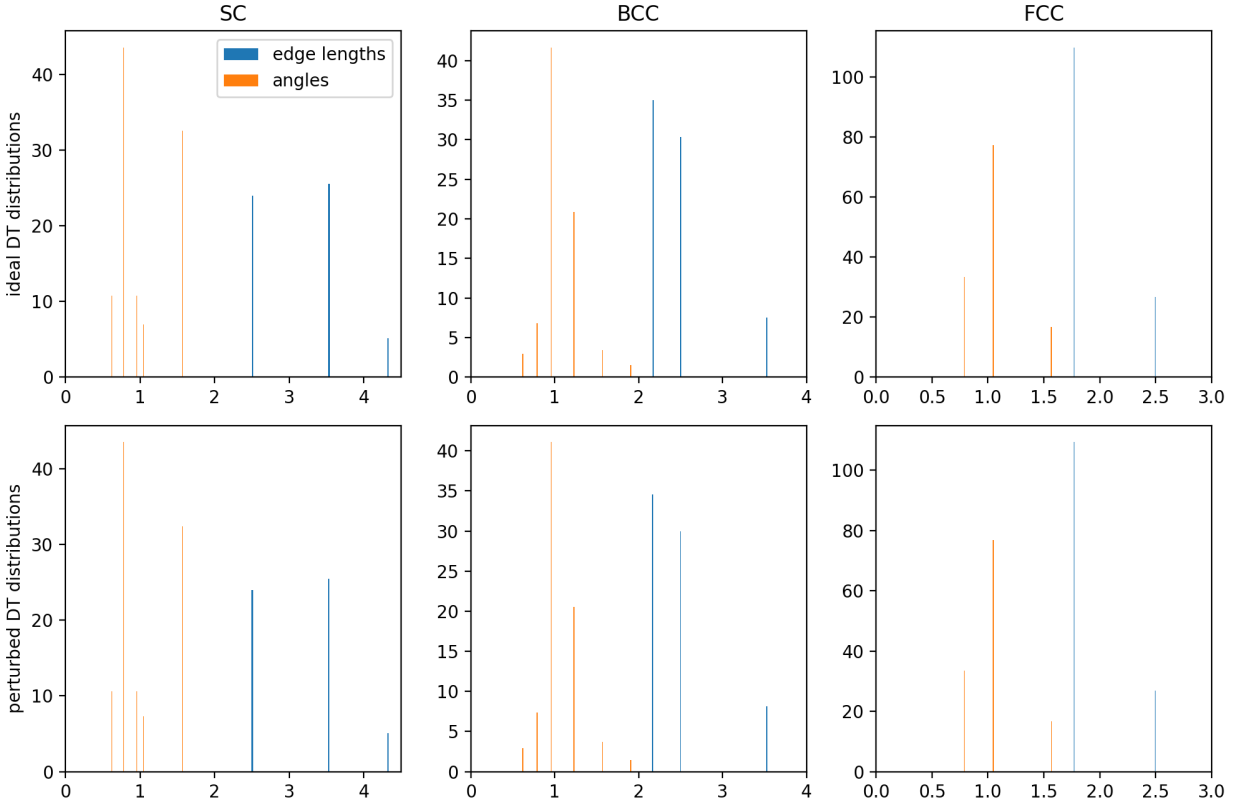


Figure 4.7: (First row) The Delaunay triangulation edge length distributions and angle distributions of the ideal lattices. The lattices are all on the domain $[0, 10]^3$ with 64 unit cells. (Second row) The distribution data from the DT of the perturbed lattices- namely an ideal lattice with one randomly chosen point perturbed a small amount. The measures of orders (written $(m_L^e(L_p), m_L^\theta(L_p))$) are approximately SC: (0.57, 3.33), BCC: (0.24, 1.74) and FCC: (0.24, 1.98).

4.4 Perturbed Lattices

By design, the MoOs in the PH and DT cases are stable [74]. In other words, a small change in the point cloud X will result in a small change in $m_L(X)$ for every MoO defined in the previous section. In this section, we consider perturbations of lattices in order to demonstrate this stability of the MoOs.

4.4.1 Single Point Perturbations

We begin with an ideal Bravais lattice (SC, BCC and FCC) generated on a domain $[0, 10]^3$, each with 216 unit cells (each having a width of $5/3$ spatial units). These lattices have 343, 559, and 1099 points respectively. A random point is then chosen, and perturbed by $b/100$ where b is the lattice parameter. The resulting PDs are shown in the second row of Fig. 4.6 while the DT distributions can be seen in the second row of Fig. 4.7. Note that even small changes to a single point may or may not yield a change in the topology. It is also worth noting that while the DT distributions are not visibly different, the MoO from the angle distributions appear to be the most sensitive to this kind of perturbation.

4.4.2 Random perturbations

Next, we analyze what happens when each point in the ideal lattices is perturbed by allowing each to walk a Brownian path. We used the small variance $\sigma^2 = dt = a^2/1000$, where a is the width of a single cell. In these simulations, we used 27 cells for each lattice (so $a = 10/3$). We also assume that the points bounce off the boundary, since we do not include periodic boundary conditions in our PH calculations, nor in our DT calculations. After long enough time, the points will have walked to a random configuration. Figure 4.8, shows the change in MoOs, both in the PH case (first row) and in the DT case (second row) as the points randomly walk. In each case, the lattices were on a domain of $[0, 10]^3$ with 27 unit cells. It is interesting to note that in the PH MoOs, the H_2 data spikes in case of SC and BCC lattices, while the H_1 data spikes in the FCC lattice- despite those lattices not having those respective data in their ideal configurations.

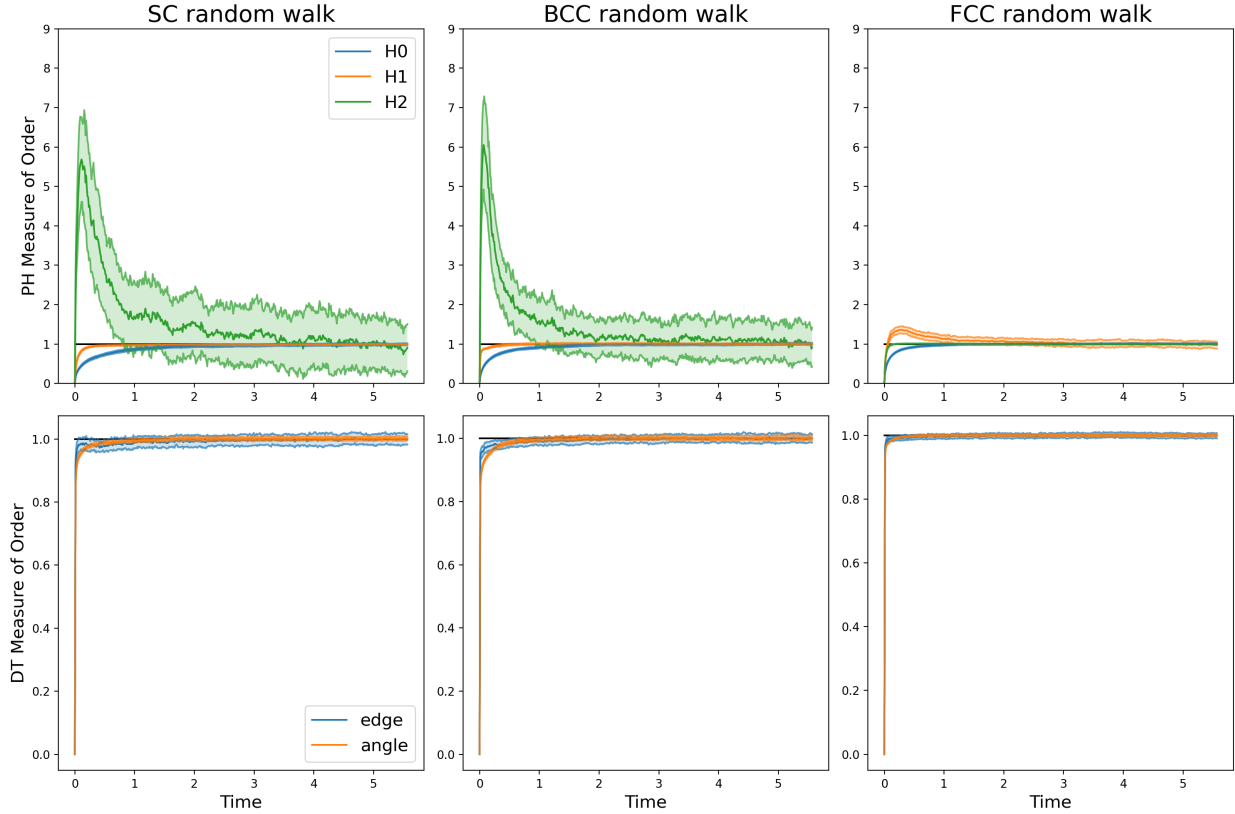


Figure 4.8: These figures exhibit the time evolution of the measure of orders of the perturbed SC, BCC, and FCC lattices with respect their ideal form lattices. The first row shows the MoO in the PH case, while the second row shows their MoO in the DT case. In each case, the perturbations were random walks with the initial configuration being an ideal lattice. The left column shows a random walk where the initial starting configuration is an SC lattice. The middle column shows a random walk with initial configuration of a BCC lattice. The right column depicts random walk whose initial configuration is an FCC lattice. In both the SC and BCC cases, the measure of order (in the PH case) contain a spike in the H_2 data- in part because both ideal lattices have no H_2 . Similarly, the H_1 measure of order spikes in the FCC case.

A similar spike was also observed in [72] and in [73] in the case of hexagonal lattices. We posit that this is the case because of the following: as the vertices walk around, the expected distance between two vertices decreases (this can be seen in H_0 as the configuration diffuses), which leads to the non-trivial topological data. When the perturbations are small, the configurations are nearly ordered. This near order configuration contains more loops (and enclosed volumes) from the VR complex than points in random position in the domain. See subsection 5.3 for more on this idea.

4.5 Pattern Formation in Three Dimensions

Pattern formation in three dimensions occurs both naturally and experimentally, and can be observed in biological morphogenesis, materials science and fluid dynamics [78, 79]. The challenge with modelling patterns in three dimensions with partial differential equations (PDEs) lies in the fact that their bifurcation diagrams are 'crowded'. That is to say, several more types of patterns can arise in three-dimensional systems, than in their two-dimensional counterparts. In the current literature, the standard approach to model three-dimensional ideal lattice patterns is to perturb known analytic solutions and feed them through a numerical PDE solver such as the ETDRK4 algorithm or finite difference methods [80, 81]. It can also happen that a solution that exhibits some pattern occurs at a minimum of a potential function. In this case, it is possible to generate patterns from white-noise initial conditions [82, 83]. A BCC lattice pattern is among the patterns found in [83], but SC and FCC lattices are not found.

Patterns produced from white-noise initial conditions will typically contain defects. While defects are naturally occurring, it may sometimes be desirable to produce perfect lattice patterns. In this section, we offer two ways to produce three-dimensional lattice patterns from low amplitude white-noise initial conditions, and we will use the topological measures of order to quantify their degrees of order. We do so by using a maximum filter to identify the locations of all local maxima, and apply PH to that point cloud. Then an ideal lattice is estimated based of the computed PH data at the last time step, which is then used to compute the time evolution of the measure of order.

4.5.1 Linear Dispersive Terms

In two-dimensional pattern formation, adding a linear dispersion term to a non-equilibrium system causes interesting behavior. If the dispersion is large enough, systems that produce patterns or spatial-temporal chaos are overridden by ripple patterns [84, 85]. If the dispersion is of moderate size, patterns will propagate in the direction of the dispersion, but the patterns will remain, and become increasingly ordered over time, as we will demonstrate by adding dispersive terms to the Brusselator (see Fig. 4.9). The Brusselator is a reaction diffusion system which is often used in the

study of three-dimensional patterns. In principle, we could use any three-dimensional system with a narrow shell of unstable wavelengths, since their amplitude equations (and hence bifurcation diagrams) would be the same [86].

We use the following modified Brusselator:

$$u_t = D_1 \Delta u + CP(u) - (B + 1)u + u^2v + A \quad (4.7)$$

$$v_t = D_2 \Delta v + CP(u) + Bu - u^2v \quad (4.8)$$

where P is a third order, autonomous differential operator. In our experience, different dispersive terms yield differing results. Even if the parameters A, B, D_1 and D_2 are chosen with a specific lattice pattern in mind (according to their bifurcation diagrams, as in [86]), some dispersive terms may change the outcome of patterns entirely. Figure 4.9 shows a solution of the Brusselator as well as two solutions of the dispersive Brusselator, one with $P = \partial_x \partial_y \partial_z$ and the other with $P = \partial_x^3$ and the persistence diagrams from their maximum locations. In all cases, ETDRK4 was used to provide solutions, on a cubic grid with $N = 64$ on the spatial domain $[-3\pi, 3\pi]^3$ with $dt = .1$ and up to time $t = 5000$. The parameters used in each simulation were $A = 2, B = 3.1, C = 1, D_1 = 1$ and $D_2 = 7.1111$, and the initial conditions were low amplitude white noise. The parameters A, B, D_1 and D_2 were chosen since they satisfy the conditions to produce a BCC pattern [86] and $C = 1$ was chosen to be moderately sized. Notice the dispersionless solution produced a nearly perfect BCC pattern but in the case in which $P = \partial_x \partial_y \partial_z$, the pattern produced is a perfect BCC lattice (see the middle column of Fig. 4.9), while when $P = \partial_x^3$ appears to have a hexagonal pattern in the yz -face, which is elongated and slanted in the xz -face (see the right column of Fig. 4.9).

It is not *a priori* clear which dispersive terms will give the desired outcome- nor why. Another dispersive term that produces the BCC lattice pattern (with the choice of parameters) is $P = \partial_x^3 + \partial_y^3 + \partial_z^3$. Note that both $\partial_x \partial_y \partial_z$ and $\partial_x^3 + \partial_y^3 + \partial_z^3$ are invariant under $2\pi/3$ -rotations about the axis $(1, 1, 1)$.

In the case in which $P = \partial_x \partial_y \partial_z$, we can observe what happens to the dispersive Brusselator (Eqs (4.7) and (4.8)) over six separate simulations. We use the same setup and parameters that were used to create the left column of Fig. 4.9, and compute the measures of order through the time evolution of the system with respect to the ideal BCC lattice. Figure 4.10 shows these results. The ideal lattice is easily estimated in this regime- since at the last time step, the pattern converges to a perfect BCC pattern (as in the middle column in Fig. 4.9). This is true for each of the six simulations depicted in Fig. 4.10. Unsurprisingly, the H_2 MoO spikes just before reaching perfect order, just as the second panel in Fig. 4.8 shows the same spike just after perturbing the ideal BCC lattice. Moreover, Fig. 4.10 shows that the system achieves an ideal pattern much sooner than $t=5000$. This is hugely beneficial for cutting back computing time.

We will refrain from pursuing this line of investigation any further since adding dispersion to the Brusselator carries no physical interpretation or use beyond generating patterns from white-noise initial conditions. Additionally, it is not clear whether consistently obtaining SC and FCC patterns from the white noise initial conditions is even possible. Instead, we present another way to produce patterns.

4.5.2 Forced Swift-Hohenberg Equation

Since it is rather difficult to generate solutions with specified lattice patterns from white noise initial conditions via the (dispersive) Brusselator, we will generate desired lattice patterns by adding a spatially periodic forcing term to a non-equilibrium system. Such systems have been studied in one and two dimensions for decades, with early applications stemming from hydrodynamic phenomena such as electrohydrodynamic instabilities in liquid crystals, Rayleigh-Bénard convective fluids, and turbulence [87–96]. Somewhat more recently, spatially periodic perturbations have been used to study optical techniques in Bénard-Marangoni convection experiments [97, 98]. In much of the earlier work, the forcing terms were spatially periodic rolls states with a prescribed forcing wavenumber. Propagating stripe states with $m : n$ resonance forcing terms have been studied extensively in one and two dimensions- see Ref [99] for a unified review at the level of am-

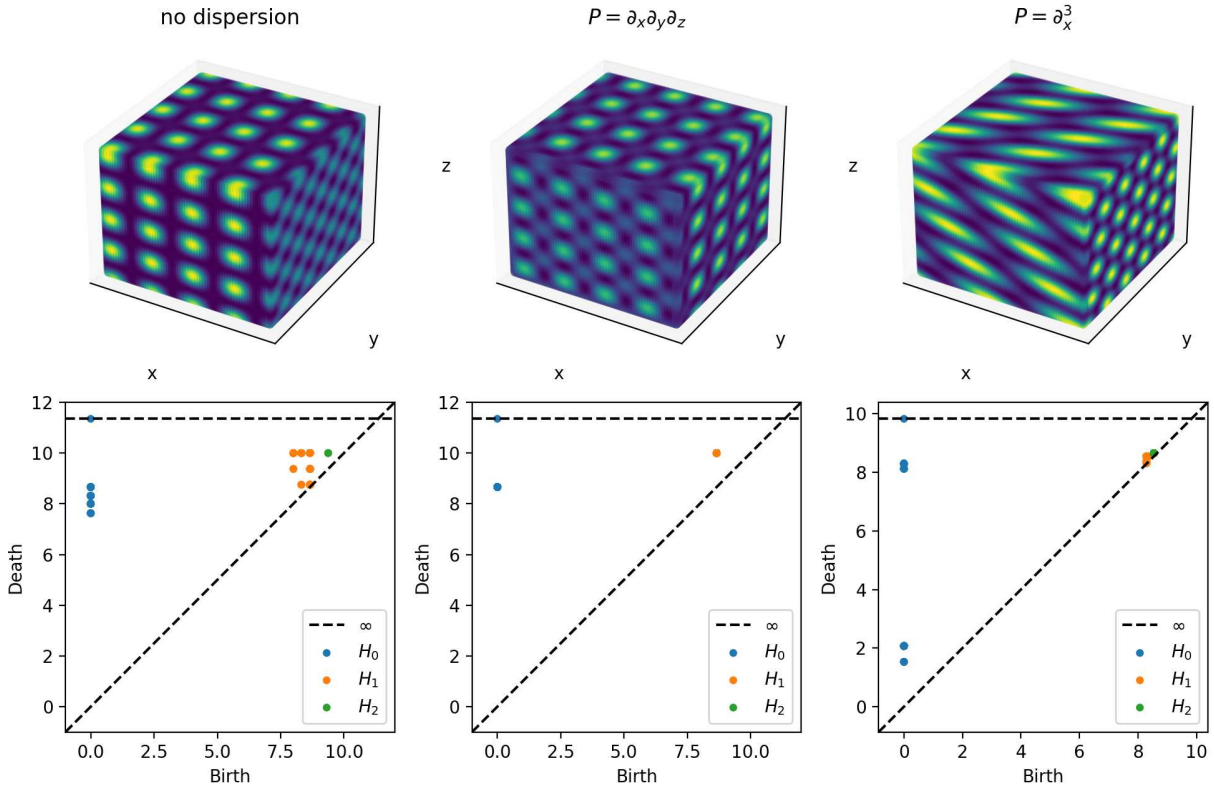


Figure 4.9: The first row depicts solutions of Eqs. (4.7) and (4.8) at $t=5000$. In all cases, the domain is $[-6\pi, 6\pi]^3$ and the parameters used were $A = 2, B = 3.1, C = 1, D_1 = 1$ and $D_2 = 7.1111$. The left column shows a solution obtain with no dispersion. The middle column shows the solution obtained with the dispersive term $P = \partial_x \partial_y \partial_z$ and its corresponding persistence diagram computed from the max locations. The second column shows the solution and its corresponding persistence data with $P = \partial_x^3$.

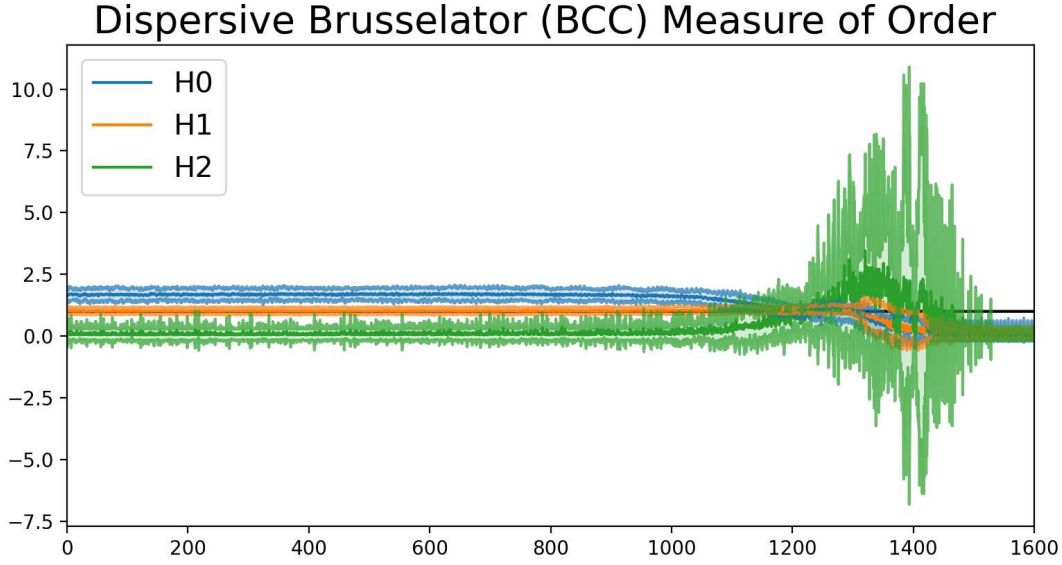


Figure 4.10: This figure shows the time evolution of the measure of orders with respect to the ideal BCC lattice. Six simulations of Eqs. (4.7) and (4.8) on the domain $[-3\pi, 3\pi]^3$ up to $t=5000$ (the time was cut off to $t=1600$ since perfect order was achieved sooner). Each simulation used low amplitude white-noise initial conditions and the parameters were $A = 2, B = 3.1, C = 1, D_1 = 1$ and $D_2 = 7.1111$. The dispersive term was $P = \partial_x^3$. The mean and confidence intervals of two standard deviations are plotted.

plitude equations. Even with a unidirectional forcing term, the authors of Ref. [99] find a wealth of pattern forming phenomena, including the appearance of hexagonal patterns for questionable choices of parameters.

In our study of PH measures of order, we will focus on the forced Swift-Hohenberg equation (FSHe):

$$u_t = -(1 + \Delta)^2 u + \mu u + \beta u^2 - u^3 - \alpha h(x)u. \quad (4.9)$$

The parameters α and β are non-negative, and μ is the bifurcation parameter whose critical value is $\mu_c = 0$. The function

$$h(x) = \sum_{\hat{k}} \cos(k_f \hat{k} \cdot x) \quad (4.10)$$

is a linear combination of cosine functions. Here, the \hat{k} are the unit wavevectors which are (to scale) dual to the lattice pattern, k_f is the forcing wavenumber and is such that $mk_f = n(k_c + q)$ for positive co-prime integers n and m and a small mismatch q of the critical wavenumber, k_c . This k_f is known as the forced wavenumber which has $m : n$ resonance.

The critical wavevectors for SC, BCC and FCC patterns can be found in [86], but we include them here for convenience.

SC lattice:

$$k_1 = -k_4 = k_c(1, 0, 0), \quad k_2 = -k_5 = k_c(0, 1, 0), \quad k_3 = -k_6 = k_c(0, 0, 1) \quad (4.11)$$

BCC lattice:

$$k_1 = -k_7 = \frac{k_c}{\sqrt{2}}(1, 1, 0), \quad k_2 = -k_8 = \frac{k_c}{\sqrt{2}}(0, 1, 1) \quad k_3 = -k_9 = \frac{k_c}{\sqrt{2}}(1, 0, 1) \quad (4.12)$$

$$k_4 = -k_{10} = \frac{k_c}{\sqrt{2}}(1, -1, 0) \quad k_5 = k_{11} = \frac{k_c}{\sqrt{2}}(0, 1, -1) \quad k_6 = -k_{12} = \frac{k_c}{\sqrt{2}}(1, 0, -1) \quad (4.13)$$

FCC lattice:

$$k_1 = -k_5 = \frac{k_c}{\sqrt{3}}(1, 1, 1), \quad k_2 = -k_6 = \frac{k_c}{\sqrt{3}}(1, -1, -1) \quad (4.14)$$

$$k_3 = -k_7 = \frac{k_c}{\sqrt{3}}(-1, 1, -1), \quad k_4 = -k_8 = \frac{k_c}{\sqrt{3}}(-1, -1, 1) \quad (4.15)$$

Here, $k_c = 1$ is the critical wavenumber for the Swift-Hohenberg equation. The forcing terms of Eq. 4.10 only require a basis for a lattice, and so each forcing term can be written as a sum of three terms. As we shall soon see, the addition of our forcing terms may beget unusual patterns with given parameters- but our purpose in this dissertation is not to give a full investigation of this. Rather, we will focus on how the patterns change as the forced amplitude and forced wavenumber change.

Indeed, at exact 1 : 1 resonance, (*i.e.* with no wavenumber mismatch so $q = 0$), the resulting pattern should closely resemble a lattice pattern. Figure 4.11 depicts the three solutions of Eq. 4.9 corresponding to SC, BCC and FCC lattice patterns. In each case, we used the parameters $\mu = -1$, $\beta = 1.1$, and the forcing parameters were $\alpha = 1$ and 1:1 resonance with $q = 0$. It is interesting to note the BCC forcing causes raised tetrahedral regions (the bright regions depicted in the middle column of Fig. 4.9) whose maxima lie on a (nearly) BCC lattice. Moreover, each solution exhibits a small number of defects. It is possible that these defects are the result of the choice of parameters and the forcing term, which compete and cause defects.

In order to continue our study of the forcing parameters, we establish some semblance of a set of control simulations- the case when $k_f = k_c = 1$ and when $\alpha = 1$. Figure 4.12 shows how the measures of order evolve over time given 50 simulations of Eq. 4.9 with of the SC, BCC and FCC forcing terms. These MoOs are once again scaled with the MoOs of random point clouds which give a basis of comparison. Thus when a measure of order is near one, that is an indication that it resembles that of a random point cloud of the same number of points as there are local maxima in the solution at later times. The plot shows the mean of the results in each case, as well as confidence intervals of 2 standard deviations. It is interesting to note the effect of adding the different forcing terms. The left panel of Fig. 4.12 suggests that a solution of Eq. (4.9) with an SC forcing term merely nucleates and is fully formed at early times. Note the spike in the H_2 MoO is consistent with the perturbation simulation of Fig. 4.8, and occurs just before obtaining a high degree of order. The right panel of Fig. 4.12 shows the time evolution of the MoO for the FCC forcing term. The measures in both H_0 and in H_2 begin near 1, which is no surprise given that the initial conditions are white noise. The H_1 MoO starts closer to zero, but spikes as the solution nucleates to a high degree of order. This is consistent with the FCC measure of order seen in Fig. 4.8.

The middle panel of Fig. 4.12 depicting the time evolution of the MoOs given the BCC forcing term is a bit more surprising. Figure 4.13 shows the time evolution of Eq. 4.9 with BCC forcing, at times $t = 4, 8$ and 30 . This figure reveals a surprising artifact of the BCC forcing term- which is

that at early times during the nucleation, the regions near local maxima appear to be spherical, but at later times, become tetrahedral regions. The reason for this behavior is not clear. However, the middle panel of Fig. 4.12 suggests that this is an occurrence that all 50 simulations go through this transition, since there is small variance in the H_2 measure of order roughly between the times $t = 5$ and $t = 12$. The larger variance of the $H - 2$ MoO at times before $t = 5$ may be due to the solution lingering at a developing stage before the formation of a lattice pattern. The larger variance at times later than $t = 15$ is possibly due to discrepancies while pinpointing local maxima in their tetrahedral regions and the maximum filter's ability to single out a single point in that region. The fact that the H_2 MoO averages just above 1.5 at $t = 50$ is consistent with the persistence diagram in the middle panel of fig. 4.11, which shows some noise in the H_2 MoO.

Now we would like to understand how the evolution of the measures of order change as the forcing parameters change. Arguably, the effect of changing the parameter α should be simpler to understand, since it controls the strength of the forcing term. Figure 4.14 illustrates the time evolution of MoOs of Eq. 4.9 for SC, BCC and FCC forcing terms- each at a lower forcing strength. The first row shows the results for when $\alpha = .5$ while the panels in second row had $\alpha = .2$. For the SC forcing term, whenever $\alpha = .5$, the nucleation is delayed until around until around $t = 10$, as indicated by the initial spike in the H_2 MoO. After $t = 10$ the variance of the H_2 MoO is larger than when $\alpha = .5$. This is because the forcing term is competing with the labyrinth pattern formation that is typical of the (unforced) SH equation. When the forcing strength of the SC forcing term is further weakened to $\alpha = .2$, low amplitude SC patterns are visible, but too weak for the max filter to find the peak locations. Starting around $t = 20$ the labyrinthine pattern begins to take precedence over the small forcing term. This is indicated by the large variance in the H_0 and H_2 MoOs, as well as by their means being noticeably above 0.

Turning our attention to the second column of Fig. 4.14, in which we have a BCC periodic forcing term with weekend forcing strength. When $\alpha = .5$, we see that the period of time in which the variance of the H_2 MoO is delayed and extended to the times roughly between $t = 12$ and $t = 20$. During this time period, the forcing term takes precedence over the labyrinthine pattern

of the unforced SH equation. In Fig. 4.12, once the variance of the H_2 MoO begins to widen, the regions about the peaks began transitioning from spherical to tetrahedral level sets. In Fig. 4.14 however, a similar occurrence of the H_2 variance is observed, but these regions about peaks never become fully formed tetrahedra. The nonzero variance does seem to suggest that the solution during this time period undergoes a struggle where the regions around the peaks are competing to between being spherical and tetrahedral. After, the time of about $t = 40$, the spherical regions dominate and continue. When the strength of the forcing term is further lowered to $\alpha = .2$, the BCC patterns nucleate at a much slower rate, but the recurring spike in the H_2 MoO is present, and prolonged. At $t = 50$, a faint BCC pattern is present, and the regions surrounding the peaks are spherical.

A look at the third column of Fig. 4.14, suggests that the FCC forcing term is the least affected by the forcing strength. When $\alpha = .5$, the pattern nucleates at early times, as indicated by the spike in the H_1 MoO, similar to what was observed in 4.8. The pattern undergoes minor changes as peaks begin to settle around $t = 20$. The variance of each of the measures of order are slightly increased, which tells us that there are defects present in the pattern. When $\alpha = .2$, the pattern nucleates at roughly $t = 8$ when the H_1 spike is present. After $t = 8$, the pattern appears to deviate from perfect order as it competes with the parameters chosen to simulate Eq. (4.9). At the end of the simulation when $t = 50$, a highly ordered FCC pattern emerges, albeit a faint one. The noticeably wider variance in each of the MoOs indicate the presence of even more defects than when the stronger forcing terms are used.

Next, we observe what happens when the forcing parameter k_f is altered. Figure 4.15 show several panels of the time evolution of the MoOs. In each panel, 50 simulations of Eq. (4.9) were carried out, using the parameters $\mu = -.1$ and $\beta = 1.1$ and the forcing parameters $\alpha = 1$. In all cases, a 1:1 resonance was used, but a small mismatch in the wavenumber was introduced. The first row shows simulations where $q = .05$ while the second row shows simulations where $q = .1$. The first column of Fig. 4.15 shows what happens when the SC forcing is used with a deviated forced wavenumber. When $q = .05$, the SC pattern forms at around $t = 4$, which is slightly later

than seen in Fig. 4.12. Once again, the characteristic spike in the H_2 MoO appears just before a high degree of order is attained, just as the peaks are prominent enough. After the spike, the pattern quickly settles in to a nearly SC lattice pattern. When the deviation in the wavenumber is increased to $q = .1$, the pattern nucleates, but the higher variance of the H_2 measure of order and the behavior of its mean roughly between $t = 3$ and $t = 12$ indicate that there are defects in the pattern. This is to be expected since the preferred wavenumber of Eq. (4.9) is $k_c = 1$, so $k_f = 1.2$ causes disruption in the pattern.

Whenever the forcing term is BCC periodic, the solutions yet again exhibit strange behavior. Figure 4.16 shows two solutions of Eq. (4.9) with BCC forcing terms and their corresponding PDs at time $t = 50$. Both solutions have a 1:1 resonance, but a small mismatch in the forced wavenumber. The left column of Fig. 4.16 shows when the small mismatch is $q = .05$ and the right column shows a solution when that mismatch is $q = .1$. Notice that when $q = .05$, the most prominent peaks occur along the edges of the domain. It can also be seen that there are depressed ellipsoidal regions where the local minima are located. This is likely the cause of the large variance in the H_2 MoO in the second column of Fig. 4.15 after the pattern is formed at early times. When the forced wavenumber becomes even larger, *i.e.* when $q = .1$, the regions around the local maxima are ellipsoidal (see the second column of Fig. 4.16) as opposed to spherical or tetrahedral as observed earlier. These ellipsoidal regions around the peaks likely cause the wide variance in the H_2 MoO after the formation of the nearly BCC lattice pattern. Since the means of the measures of order are nonzero, the defects are present. Such defects can be seen on the boundary in Fig. 4.16.

The right column of Fig. 4.15 shows the time evolution of the measures of order when the forcing term is FCC periodic. Just as before, the forcing term seems to be the least affected by the change in forcing parameters. In both the $q = .05$ and the $q = .1$ cases, the variances of the measures of order are low. The MoOs also reach a high degree of order and are close to zero at early times, indicating that the FCC patterns nucleate and settle quickly.

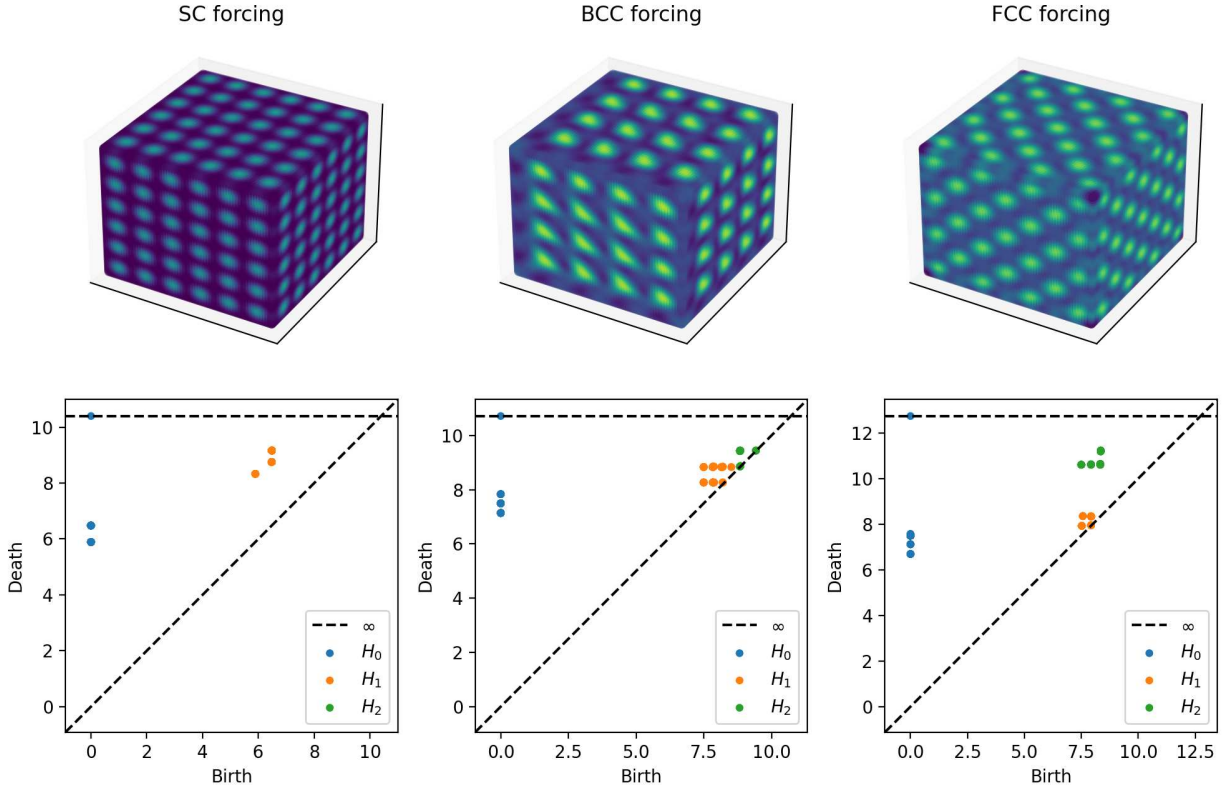


Figure 4.11: Simulations of Eq. 4.9 with SC, BCC and FCC forcing terms respectively. In each case, we used a 64^3 grid on the domain $[-6\pi, 6\pi]^3$ and the parameters $\mu = -0.1$ and $\beta = 1.1$. The forcing parameters were $\alpha = 1$ with a 1:1 resonance with $q = 0$. The initial condition were low amplitude white noise and the solutions are shown at $t = 50$.

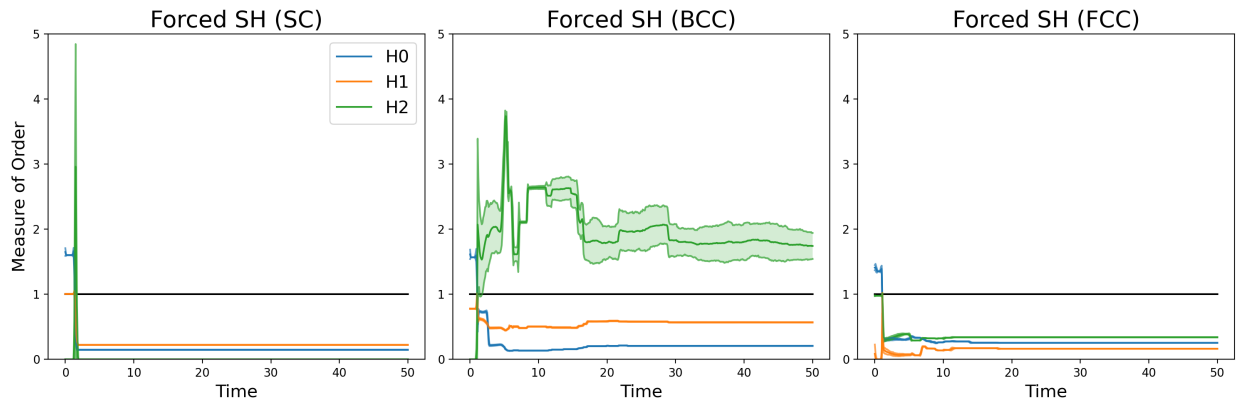


Figure 4.12: Each figure depicts a collection of 50 simulations of Eq. 4.9 with SC, BCC and FCC forcing terms respectively. The measure of order was computed from the PH of the local maxima at each time step of the solution until $t = 50$. In all the the simulations, low amplitude white-noise initial conditions were used, a 64^3 grid was used on the domain $[-6\pi, 6\pi]^3$ with the parameters $\mu = -0.1$, $\beta = 1.1$ and the forcing parameters $\alpha = 1$ and with $k_f = k_c = 1$. The means of the results are plotted, as well as confidence intervals within 2 standard deviations, with the area between the bands being shaded.

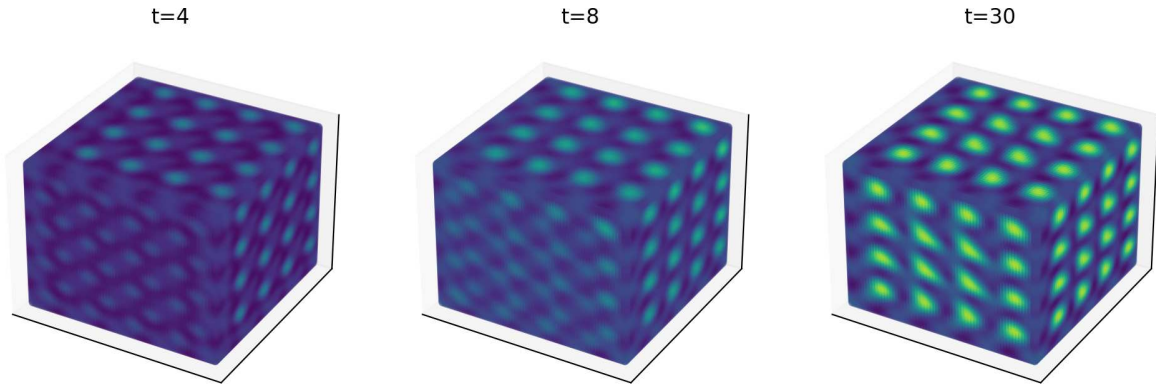


Figure 4.13: Three snapshots of the time evolution of Eq. 4.9 with BCC forcing. A 64^3 grid was used on the domain $[-6\pi, 6\pi]^3$. The parameters were $\mu = -.1$ and $\beta = 1.1$ and the forcing parameters where $\alpha = 1$ and $k_f = k_c = 1$. The times shown are at $t = 4, t = 8$ and $t = 30$ respectively.

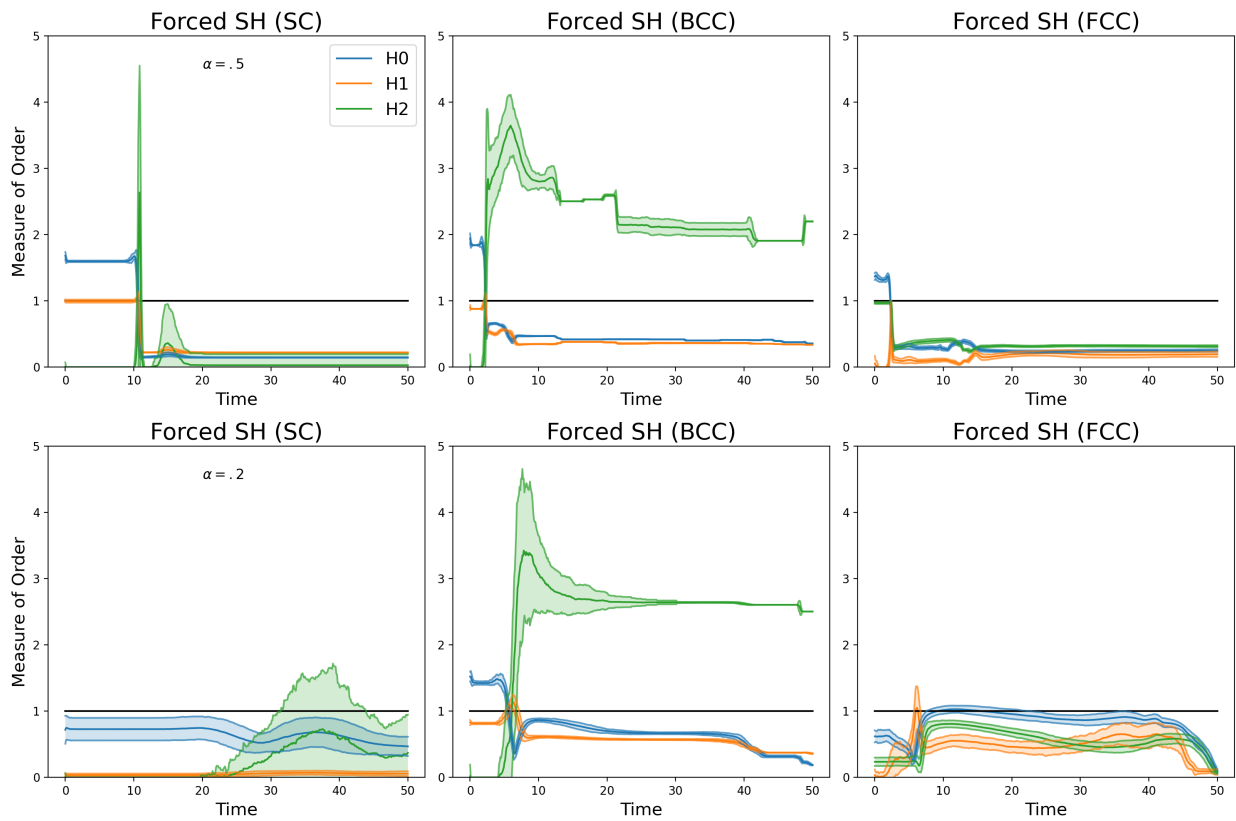


Figure 4.14: Each panel depicts the time evolution of the measures of order for 50 simulations of Eq. 4.9. In each case, a 64^3 grid was used on the domain $[-6\pi, 6\pi]^3$. The parameters were $\mu = -.1$ and $\beta = 1.1$. In the first row, the forcing strength was $\alpha = .5$ and in the second row $\alpha = .2$. In all cases, $k_f = k_c = 1$ and the final time was $t = 50$.

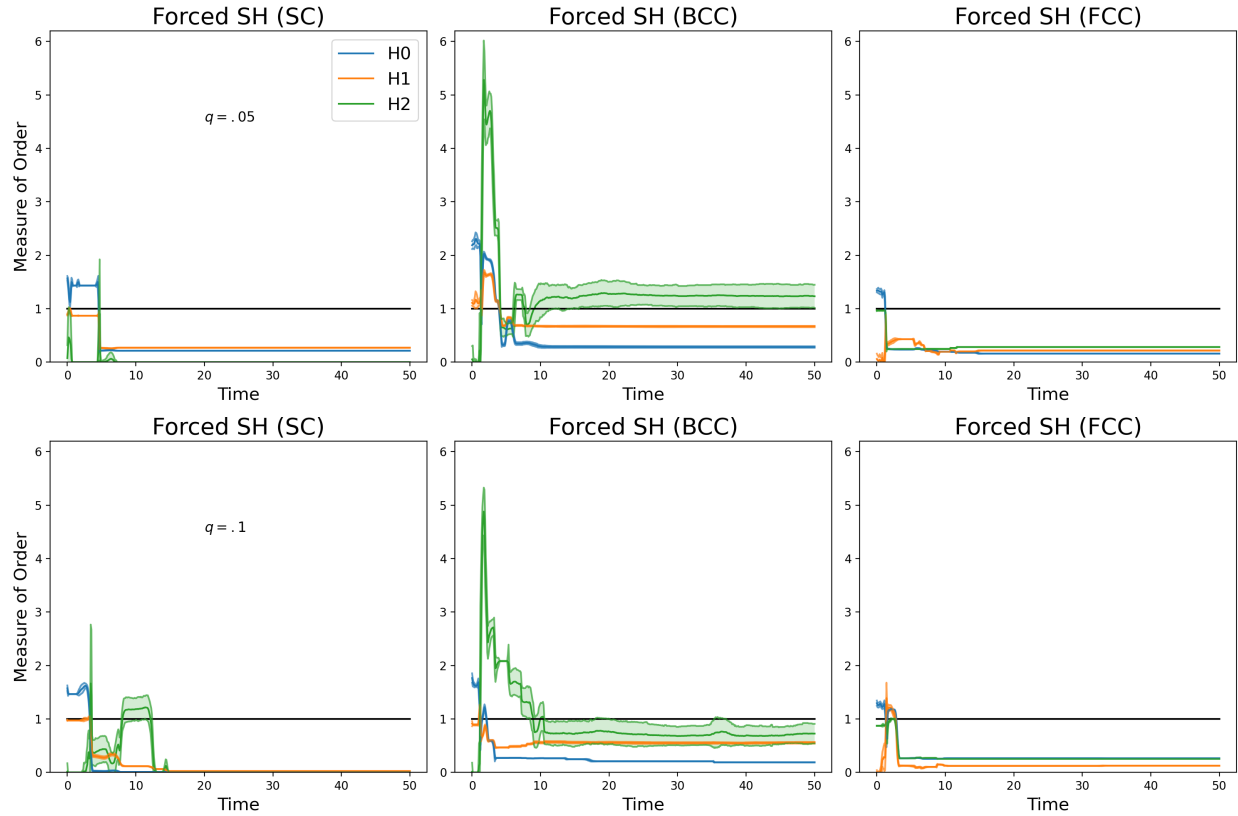


Figure 4.15: Each panel depicts the time evolution of the measures of order for 50 simulations of Eq. 4.9. In each case, a 64^3 grid was used on the domain $[-6\pi, 6\pi]^3$. The parameters were $\mu = -.1$ and $\beta = 1.1$. The forcing strength in each simulation was $\alpha = 1$. The forced resonance was 1:1 but a small deviation in the forced wavenumber was introduced. In the first row, the deviation was $q = .05$ and in the second row $q = .1$. In all cases, the final time was $t = 50$.

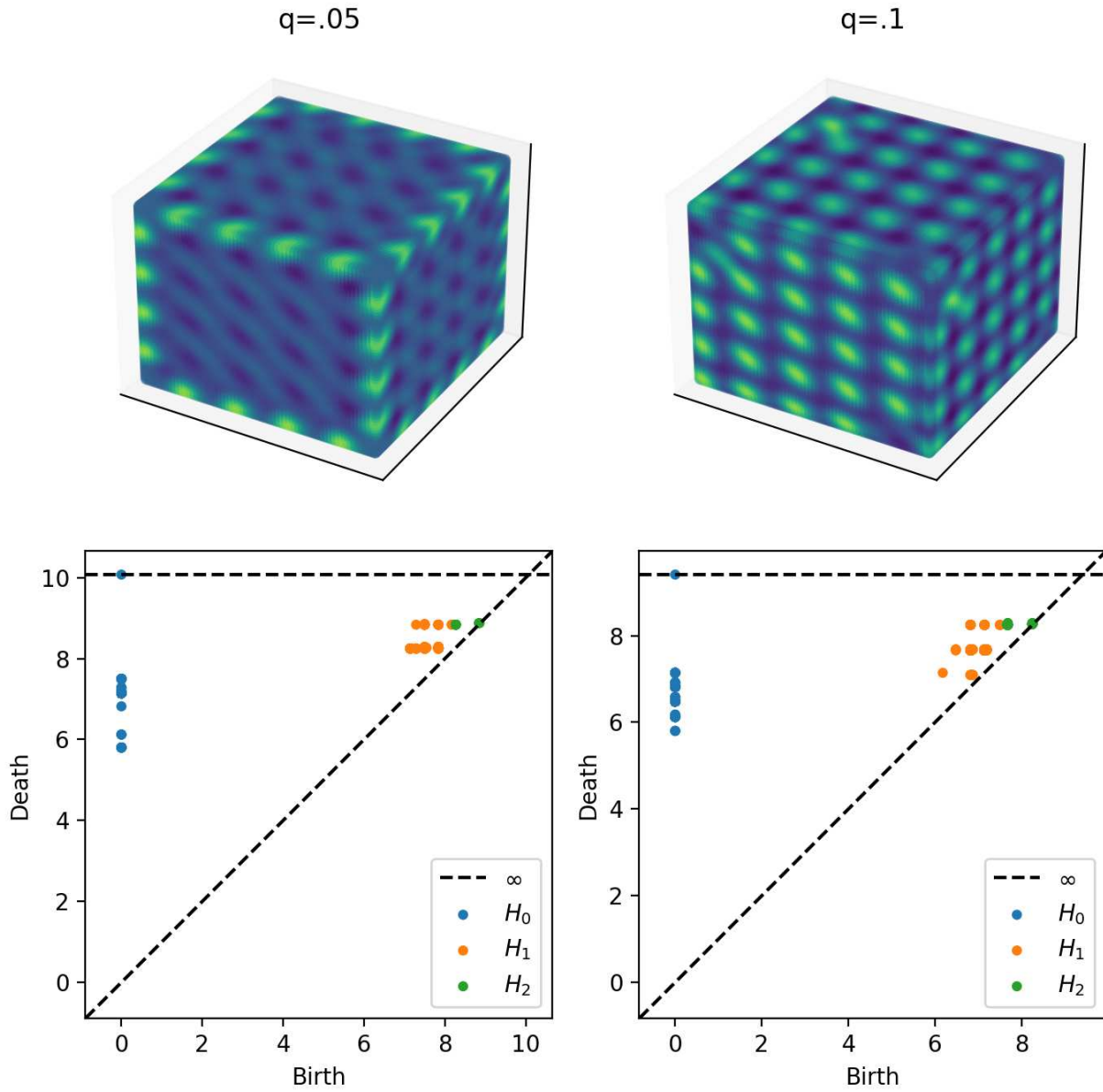


Figure 4.16: This figure shows the results of two simulations of Eq. (4.9) with a BCC periodic forcing term. In each case, we used 64^2 grids on a domain of $[-6\pi, 6\pi]^3$. The parameters were $\mu = -.1$ and $\beta = 1.1$. In both cases the forcing strength was $\alpha = 1$. The left panel shows when the forced wavenumber had a mismatch of $q = .05$ while the right panel shows a solution whose forced wavenumber was $q = .1$. In both cases, the solutions are shown at $t = 50$.

4.6 Conclusions

In this paper, we have discussed a measure of order for imperfect three-dimensional patterns. We introduced the concepts of persistent homology and of Delaunay triangulations, the Wasserstein metric as a tool for quantifying order in point clouds with respect to ideal lattices. We drew some comparisons between this topological measure of order with a more geometric measure of order- via the Delaunay triangulation. We discern that for 3d patterns that the additional data (the H_2) provide a more telling story about the time evolution (dis)ordering systems.

We then explored the application of these measures of order to three-dimensional pattern formation. We discussed how pattern formation of non-equilibrium systems in three dimensions occurs naturally in various fields. We highlighted the challenges in modeling three-dimensional lattice patterns from white-noise initial conditions. To address these challenges, we presented two approaches for producing three-dimensional lattice patterns from low-amplitude white-noise initial conditions. The first approach involved adding linear dispersive terms to the Brusselator equations, which led to surprising outcomes of pattern- including the emergence of a perfectly ordered lattice pattern. The second approach involved a periodic forcing term to the Swift-Hohenberg equation, which has several potential applications in hydrodynamics and optics.

Overall, these topological measures of order provide valuable insights into the orderliness of imperfect three-dimensional patterns and the time evolution of pattern forming systems. By understanding and quantifying the order in such patterns, we can gain a deeper understanding of complex systems and potentially uncover underlying principles governing their formation and behavior.

Chapter 5

Discussion of open problems

The project of Chapter 4 has led to a number of unanswered questions, which are as far as we know, open. In this concluding chapter, we touch on these.

5.1 Moduli Space of Bravais Lattices

Given a basis $\mathcal{B} = \{b_1, b_2, \dots, b_n\}$ of \mathbb{R}^n , a Bravais lattice, L is defined to be the integer span of the basis \mathcal{B} . We would like to parameterize this collection of lattices in a way that is conducive to our study of (dis)order. One approach for two-dimensional lattices, as taken in [72], is to consider the fundamental triangle spanned by the two basis vectors b_1 and b_2 such that the third side of the triangle, $b_1 - b_2$ is scaled to length 1. Under this definition, two lattices are equivalent if there is an orthogonal transformation or a scale factor of the fundamental triangles. This lends itself to a nice description of the moduli space of lattices. The downside to this approach is that this parameterization does little in the way of distinguishing lattices up to their PH - *i.e.* their shape. Moreover, it is not immediately clear how to generalize this to higher dimensions.

There is but another way. Note that we can identify a full rank lattice in \mathbb{R}^n by a matrix $B \in GL(n, \mathbb{R})$, whose columns are the generators of the lattice. In order to distinguish lattices up to shape, we consider two group actions on $GL(n, \mathbb{R})$: the left action of the conformal orthogonal group $CO(n) \cong \mathbb{R}^* \times O(n)$ via $g \cdot B = gB$ for $g \in CO(n)$ and the right action of $GL(n, \mathbb{Z})$ on $GL(n, \mathbb{R})$ given by $B \cdot u = Bu$ for $u \in GL(n, \mathbb{Z})$. The resulting double coset space $CO(n) \backslash GL(n, \mathbb{R}) / GL(n, \mathbb{Z})$ are the lattices up to shape. The above approach is common in number theory [100, 101].

The above description of lattice-shape space is easy to write down, it would be interesting to give a geometric realization of this space in low dimensions. It is conceivable that sampling such a space may help with that endeavor.

Given a basis for a lattice, we can write a matrix, say $A \in GL(n, \mathbb{R})$. We can thus generate a random lattice in the following way: First, generate a random matrix A whose entries are distributed normally. Next, apply the LLL algorithm to write the factorization $A = U\tilde{A}$, where \tilde{A} is a reduced basis and $U \in GL(n, \mathbb{Z})$. This factorization is unique if we require all pairwise angles between the columns to be less than or equal to $\pi/2$. Then, apply the QR algorithm to factor $\tilde{A} = QR$. This factorization is unique if we take the diagonals of R to be positive. Finally, we can re-scale R by defining $K = \det(R)^{-1/n}R$. Thus K is a canonical representation of a lattice up to shape.

The above algorithm could be used for Monte Carlo simulations that could be used to probe questions of random lattices (what is the expected lattice?) and perhaps even help come to grips with a geometric realization of the moduli space of lattices to shape.

5.2 Close-Packed Lattices

Another interesting observation is that in dimensions two and three, close packed lattices (hexagonal, FCC and HCP) contain no H_1 data. Figure 5.1 depicts the PDs for an HCP lattice, with 216 points. We may ask then, do all close packed lattices in \mathbb{R}^n have $\mu_L^1 = 0$? Further, given a random lattice (or perhaps even a random set of points), can we find a close packed lattice by minimizing topological constraints from PH?

5.3 H_1 count of a random set points

In subsection 4.4.2, we made a claim that the spikes in the MoOs are due to the packing of topological features in highly ordered configurations of points. We can back this claim with some Monte Carlo simulations. For these simulations, we focus on hexagonal lattices for simplicity, and note that similar arguments can be applied to lattices in higher dimensions. Further, our configurations will all be made in a domain $[0, 10]^2$ - but it is important to notice that the size of the domain does not matter, only the number of points. We do the following: we create a lattice, which is then perturbed so that each point takes one Brownian step whose variance is proportional to the distance

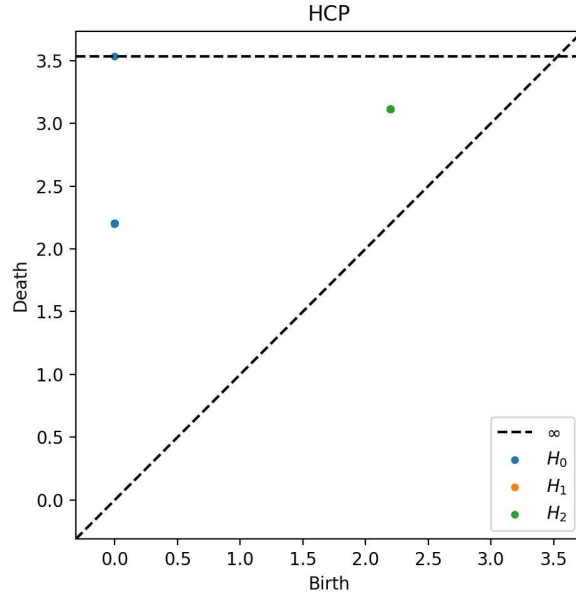


Figure 5.1: The PD of an HCP lattice with 216 points, generated by vertices $r(2i + (j + k) \bmod 2, \sqrt{3}(j + (k \bmod 2)/3), k 2\sqrt{6}/3)$ with $i, j, k = 1, 2, \dots, 6$ and with $r = 1.1$.

between neighboring points in the original lattice. We compute the PH, and count the number of H_1 data that occur. Rinse and repeat for a total of 1,000,000 instances and store the H_1 data count for each instance, and plot the (normalized) H_1 count distribution and cumulative distribution. In tandem, we do the same with a set of uniformly distributed random point cloud of the same number of points as the perturbed lattice. We repeat this simulation for different sized configurations.

The first simulation consisted of configurations that have 4 points. Figure 5.2 depicts an instance of each configuration, and the H_1 count distributions (denoted by $\#PH_1$). Note that the mean number of H_1 obtained from perturbed hexagonal lattices is greater than that of the random point clouds, while their variances are approximately the same. The distributions shown in Fig. 5.2 are Bernoulli distributions, because there can be at most one H_1 data with four given points- so the presence of an H_1 data can be modelled as a success. As the size of the configurations grow, the number of H_1 data becomes Gaussian distributed- a consequence of the Central Limit Theorem. Figure 5.3 shows the H_1 count distributions of larger point clouds. Since the means and variances can be estimated from the simulated data, the Gaussian distributions can thus be estimated. These simulations indicate that the expected number of H_1 data from a nearly hexagonal configuration is

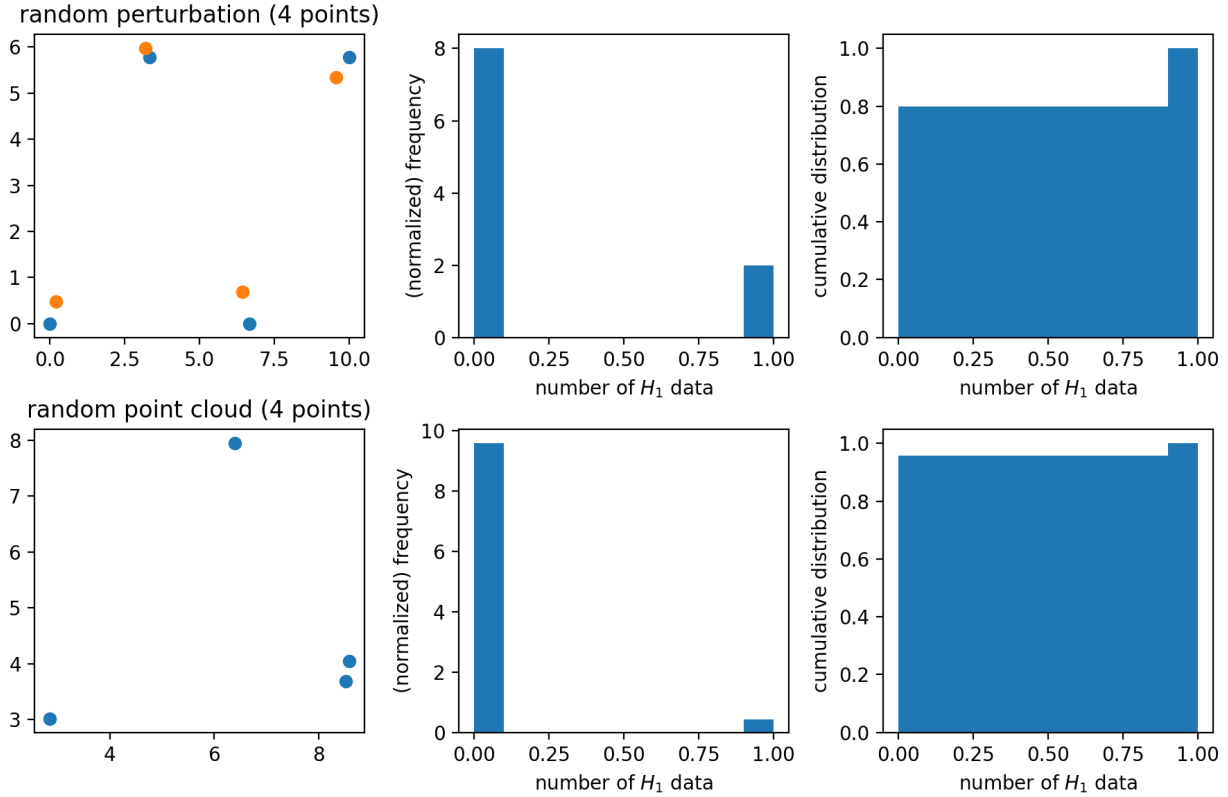


Figure 5.2: The top row shows a single instance of a perturbed lattice (orange points) and the corresponding H_1 count distributions over 1,000,000 independent instances. The second row shows the same but for random point clouds. This simulation gives the $E(\#PH_1) \approx .20$ and $\text{var}(\#PH_1) \approx .16$ for perturbed hexagonal lattices and $E(\#PH_1) \approx .04$ and $\text{var}(\#PH_1) \approx .04$ for the random point clouds. Note in both cases, these are Bernoulli distributions.

greater than the expected number of H_1 data from a random point cloud (with the same number of points). Figure 5.4 shows the mean and variance data of the H_1 count distribution of several Monte Carlo simulations, each using different sized point clouds. It is interesting to note that the variances in the H_1 count between the perturbed hexagonal configuration and the random point cloud are nearly the same.

This would be a neat integral geometry problem to pursue. We can ask, what is the probability that four points in a convex subset of the plane produce H_1 data? If this could be answered rigorously given the two types of distributions (uniformly and from a perturbed hexagonal lattice), we could begin fully explain the spikes in the MoO data that appear in [72, 73] and perhaps have some idea on doing the same for the higher-dimensional cases seen in this paper.

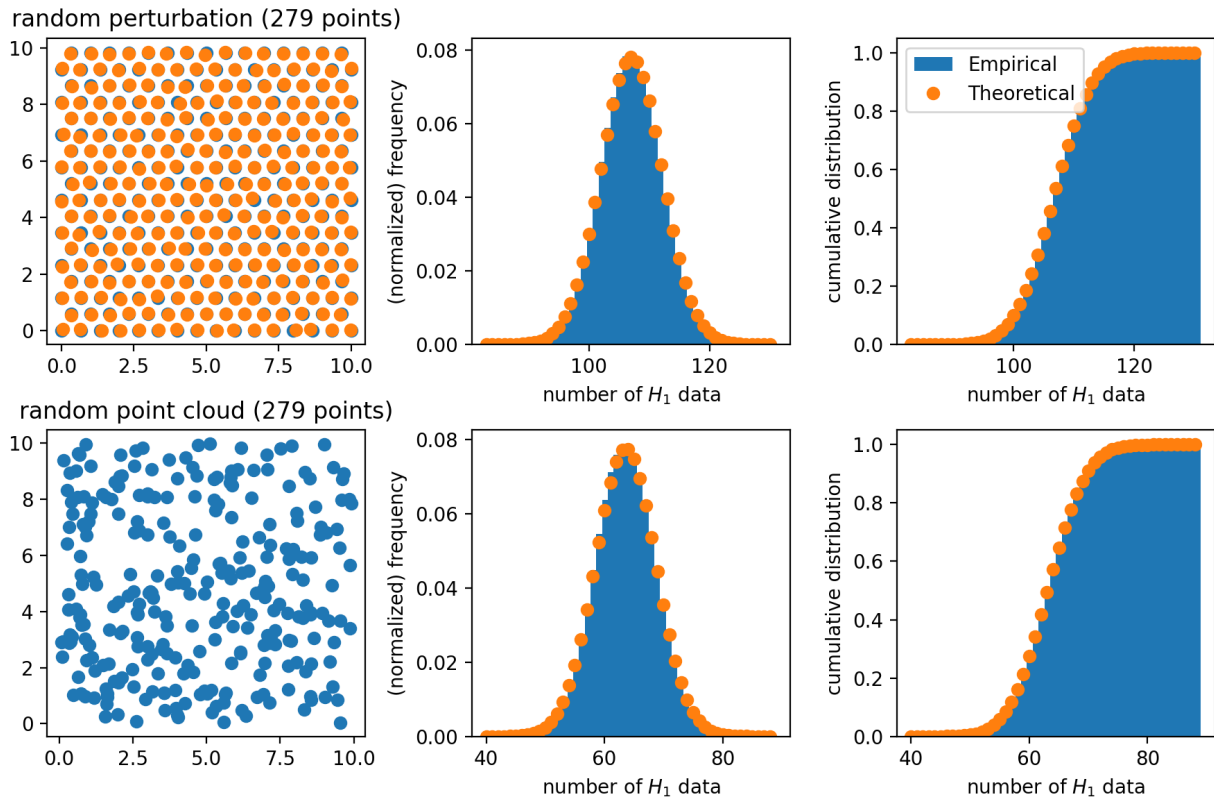


Figure 5.3: The top row shows a single instance of a perturbed lattice (orange points) and the corresponding H_1 count distributions over 1,000,000 independent instances. The second row shows the same but for random point clouds. This simulation gives the $E(\#PH_1) \approx 107$ and $\text{var}(\#PH_1) \approx 26$ for perturbed hexagonal lattices and $E(\#PH_1) \approx 63$ and $\text{var}(\#PH_1) \approx 26$ for the random point clouds.

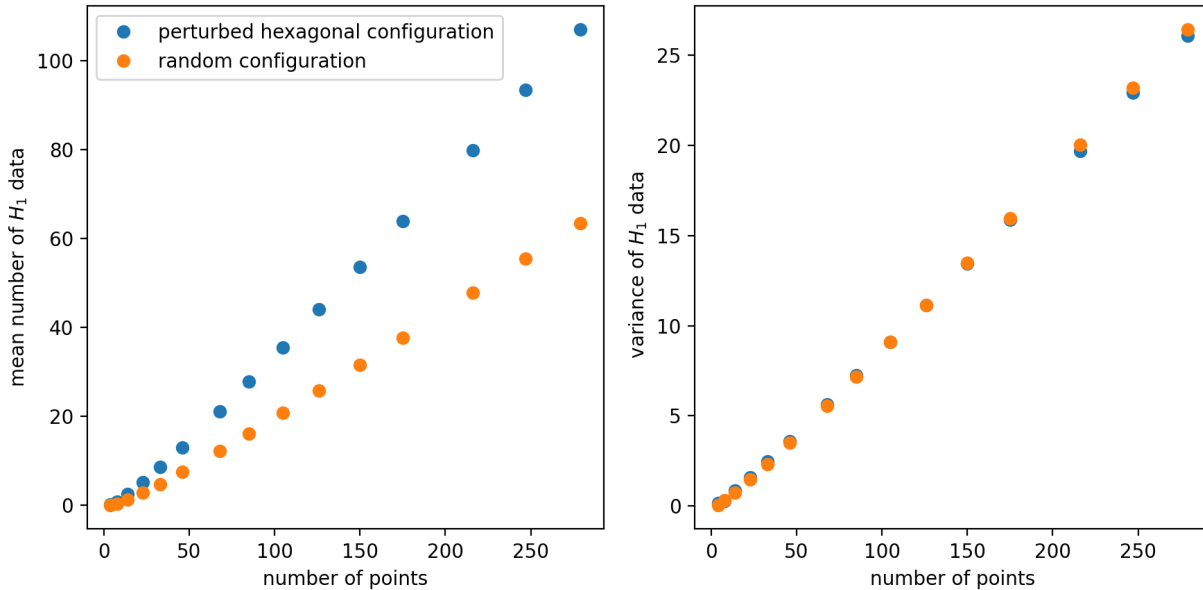


Figure 5.4: This figure shows the mean and variance of the H_1 count data over several Monte Carlo simulations. Each simulation had 1,000,000 samples, and increased the size of each configuration, starting with 3 points, and up to 279 points.

5.4 Linear Dispersive Terms in Non-Equilibrium Pattern Forming Systems

The problem of added linear dispersion has been studied when dispersion is small [102] and when dispersion is large [84, 85, 103]. As far as the authors are aware, the addition of moderately sized linear dispersion to a system with a narrow band of unstable wavelengths has not been studied. In subsection 4.5.1, we observe that the addition of (some) dispersive term can increase the order of a resulting pattern, but it is not exactly known why this is the case. Simulations indicate that this is also true for patterns in two dimensions.

Additionally, in subsection 4.5.1, we had a brief look on the effects of added linear dispersion (of moderately sized) to the Brusselator. We noted that different dispersive terms may beget unexpected patterns. It stands to reason that a third-order (homogeneous) differential operator which is invariant under cubic symmetry may produce the desired lattice patterns- but finding such a differential operator would require a descent amount of algebraic geometry- possibly a modified Derksen's algorithm [104]. The input of Derksen's algorithm is a (finite) linear representation of a

group, and the output is a generating set of homogeneous polynomials which are symmetric under that group action. The modification is slight, and is merely to consider the polynomial ring over the operators $\partial_x, \partial_y, \dots$

Given the right parameters of some non-equilibrium system, it would be interesting to see if we could generate other lattice patterns from low amplitude white-noise initial conditions with a moderately sized linear dispersive term. Indeed, it would be amusing to do so, and to understand why the added dispersive terms (and which ones, at that) contribute to the highly ordered patterns. We posit that the dispersive terms cause a transfer of energy between regions with differing dominating wavenumbers- which would in turn drive defects caused by the local patches to collide and annihilate, thus producing a perfect lattice pattern.

5.5 Forced SH Equation

The discussion of the forced SH equation in this paper barely scratches the surface. It would be interesting and perhaps useful to engage with a deeper study at the level of amplitude equations. As we have noted in section 4.5.2, there are interesting phenomena that occur with the BCC periodic forcing term- thus warranting a deeper study. It would also be reasonable to study what happens at $m : n$ resonance when $m \neq n$. Such a study could be useful for optical lattices.

Bibliography

- [1] Yasunori Nishimori, Shotaro Akaho, and Mark D Plumbley. Riemannian optimization method on generalized flag manifolds for complex and subspace ICA. *AIP Conference Proceedings*, 872(1):89–96, 2006.
- [2] Bruce Draper, Michael Kirby, Justin Marks, Tim Marrinan, and Chris Peterson. A flag representation for finite collections of subspaces of mixed dimensions. *Linear Algebra and its Applications*, 451:15–32, 2014.
- [3] Tim Marrinan, J Ross Beveridge, Bruce Draper, Michael Kirby, and Chris Peterson. Flag manifolds for the characterization of geometric structure in large data sets. In Assyr Abdulle, Simone Deparis, Daniel Kressner, Fabio Nobile, and Marco Picasso, editors, *Numerical Mathematics and Advanced Applications – ENUMATH 2013*, pages 457–465. Springer International Publishing, Cham, 2015.
- [4] Ke Ye, Ken Sze-Wai Wong, and Lek-Heng Lim. Optimization on flag manifolds. Preprint, [arXiv:1907.00949 \[math.OC\]](https://arxiv.org/abs/1907.00949), 2019.
- [5] Kee Yuen Lam. A formula for the tangent bundle of flag manifolds and related manifolds. *Transactions of the American Mathematical Society*, 213:305–314, 1975.
- [6] Parameswaran Sankaran and Peter Zvengrowski. Stable parallelizability of partially oriented flag manifolds. *Pacific Journal of Mathematics*, 128(2):349–359, 1987.
- [7] Parameswaran Sankaran and Peter Zvengrowski. Stable parallelizability of partially oriented flag manifolds. II. *Canadian Journal of Mathematics. Journal Canadien de Mathématiques*, 49(6):1323–1339, 1997.
- [8] Pierre-Antoine Absil, Alan Edelman, and Plamen Koev. On the largest principal angle between random subspaces. *Linear Algebra and its Applications*, 414(1):288–294, 2006.

- [9] Eugene Salamin. Application of quaternions to computation with rotations. Working paper, Stanford AI Lab, 1979.
- [10] Vyacheslav Leonidovich Girko. Distribution of eigenvalues and eigenvectors of orthogonal random matrices. *Ukrainian Mathematical Journal*, 37(5):457–463, 1985. Translated from *Ukrainskii Matematicheskii Zhurnal* 37(5):568–575, 1985.
- [11] Yasuko Chikuse. *Statistics on Special Manifolds*, volume 174 of *Lecture Notes in Statistics*. Springer–Verlag, New York, NY, 2003.
- [12] Alan Edelman, Tomás A Arias, and Steven T Smith. The geometry of algorithms with orthogonality constraints. *SIAM Journal on Matrix Analysis and Applications*, 20(2):303–353, 1998.
- [13] Helaman R P Ferguson, David H Bailey, and Steve Arno. Analysis of PSLQ, an integer relation finding algorithm. *Mathematics of Computation*, 68:351–369, 1999.
- [14] Brenden Balch, Chris Peterson, and Clayton Shonkwiler. Expected distances on manifolds of partially oriented flags. Preprint, 2020, [arXiv:2001.07854](https://arxiv.org/abs/2001.07854) [math.DG].
- [15] José R. Berrendero, Antonio Cuevas, and Beatriz Pateiro-López. Shape classification based on interpoint distance distributions. *Journal of Multivariate Analysis*, 146:237–247, 2016.
- [16] Marco Bonetti and Marcello Pagano. The interpoint distance distribution as a descriptor of point patterns, with an application to spatial disease clustering. *Statistics in Medicine*, 24(5):753–773, 2005.
- [17] Mireille Boutin and Gregor Kemper. On reconstructing n -point configurations from the distribution of distances or areas. *Advances in Applied Mathematics*, 32(4):709–735, 2004.
- [18] Daniel Brinkman and Peter J. Olver. Invariant histograms. *The American Mathematical Monthly*, 119(1):4–24, 2012.

- [19] Facundo Mémoli. Gromov–Wasserstein distances and the metric approach to object matching. *Foundations of Computational Mathematics*, 11(4):417–487, 2011.
- [20] Facundo Mémoli and Tom Needham. Gromov–Monge quasi-metrics and distance distributions. Preprint, 2018, arXiv:1810.09646 [math.MG].
- [21] Robert Osada, Thomas Funkhouser, Bernard Chazelle, and David Dobkin. Shape distributions. *ACM Transactions on Graphics*, 21(4):807–832, 2002.
- [22] Luis Polanco and Jose A. Perea. Coordinatizing data with lens spaces and persistent cohomology. In Zachary Friggstad and Jean-Lou De Carufel, editors, *Proceedings of the 31st Canadian Conference on Computational Geometry (CCCG 2019)*, pages 49–58, 2019.
- [23] Luis Alday, Martin Fluder, and James Sparks. The large N limit of M2-branes on lens spaces. *Journal of High Energy Physics*, 2012:57, 2012.
- [24] Ralf Aurich and Sven Lustig. A survey of lens spaces and large-scale cosmic microwave background anisotropy. *Monthly Notices of the Royal Astronomical Society*, 424(2):1556–1562, 2012.
- [25] Shinya Tomizawa. Multicharged black lens. *Physical Review D*, 100(2):024056, 2019.
- [26] Jean-Philippe Uzan, Alain Riazuelo, Roland Lehoucq, and Jeffrey Weeks. Cosmic microwave background constraints on lens spaces. *Physical Review D*, 69(4):043003, 2004.
- [27] Alfred Gray and Lieven Vanhecke. Riemannian geometry as determined by the volumes of small geodesic balls. *Acta Mathematica*, 142(3–4):157–198, 1979.
- [28] James Waddell Alexander. Note on two three-dimensional manifolds with the same group. *Transactions of the American Mathematical Society*, 20(4):339–342, 1919.
- [29] Elmer Julian Brody. The topological classification of the lens spaces. *Annals of Mathematics, Second Series*, 71(1):163–184, 1960.

- [30] Akira Ikeda and Yoshihiko Yamamoto. On the spectra of 3-dimensional lens spaces. *Osaka Journal of Mathematics*, 16(2):447–469, 1979.
- [31] Roland Lehoucq, Jean-Philippe Uzan, and Jeffrey Weeks. Eigenmodes of lens and prism spaces. *Kodai Mathematical Journal*, 26(1):119–136, 2003.
- [32] Józef H. Przytycki and Akira Yasukhara. Symmetry of links and classification of lens spaces. *Geometriae Dedicata*, 98(1):5–61, 2003.
- [33] Kurt Reidemeister. Homotopieringe und Linsenräume. *Abhandlungen aus dem Mathematischen Seminar der Universität Hamburg*, 11(1):102–109, 1935.
- [34] Paolo Salvatore and Riccardo Longoni. Configuration spaces are not homotopy invariant. *Topology*, 44(2):375–380, 2005.
- [35] Minoru Tanaka. Compact Riemannian manifolds which are isospectral to three-dimensional lens spaces. II. *Proceedings of the Faculty of Science of Tokai University*, 14:11–34, 1979.
- [36] Celso Viana. The isoperimetric problem for lens spaces. *Mathematische Annalen*, 374(1):475–497, 2018.
- [37] Heinrich Tietze. Über die topologischen Invarianten mehrdimensionaler Mannigfaltigkeiten. *Monatshefte für Mathematik und Physik*, 19:1–118, 1908.
- [38] Joseph A. Wolf. *Spaces of Constant Curvature*. AMS Chelsea Publishing, Providence, RI, sixth edition, 2011.
- [39] Alan Edelman, Tomás A. Arias, and Steven T. Smith. The geometry of algorithms with orthogonality constraints. *SIAM Journal on Matrix Analysis and Applications*, 20(2):303–353, 1998.
- [40] Izrail S. Gradshteyn and Iosif M. Ryzhik. *Table of Integrals, Series, and Products*. Elsevier, Amsterdam, eighth edition, 2015.

- [41] Anthony William Fairbank Edwards. Gilbert's sine distribution. *Teaching Statistics*, 22(3):70–71, 2000.
- [42] Grove Karl Gilbert. The moon's face: A study of the origin of its features. *Bulletin of the Philosophical Society of Washington*, 12:241–292, 1893.
- [43] Michel Boileau. Thick/thin decomposition of three-manifolds and the Geometrisation Conjecture. In Riccardo Benedetti and Carlo Mantegazza, editors, *Ricci Flow and Geometric Applications: Cetraro, Italy 2010*, volume 2166 of *Lecture Notes in Mathematics*, chapter 2, pages 21–70. Springer, Cham, 2016.
- [44] Gregory I Sivashinsky. Instabilities, pattern formation, and turbulence in flames. *Annual Review of Fluid Mechanics*, 15(1):179, 1983.
- [45] Y. Kuramoto and T. Tsuzuki. Persistent propagation of concentration waves in dissipative media far from thermal equilibrium. *Progress of Theoretical Physics*, 55:356, 1976.
- [46] Rodolfo Cuerno and Albert-László Barabási. Dynamic scaling of ion-sputtered surfaces. *Phys. Rev. Lett.*, 74(23):4746, 1995.
- [47] M.A. Makeev, R. Cuerno, and A.L. Barabási. Morphology of ion-sputtered surfaces. *Nucl. Instrum. Meth. B*, 197(3):185, 2002.
- [48] R Mark Bradley. Theory of nanoscale ripple topographies produced by ion bombardment near the threshold for pattern formation. *Phys. Rev. E*, 102(1):012807, 2020.
- [49] T. Kawahara. Formation of saturated solitons in a nonlinear dispersive system with instability and dissipation. *Phys. Rev. Lett.*, 51:381, 1983.
- [50] Kevin M Loew and R Mark Bradley. Effect of dispersion on the nanoscale patterns produced by ion sputtering. *Phys. Rev. E*, 100(1):012801, 2019.
- [51] Takuji Kawahara and Sadayoshi Toh. Pulse interactions in an unstable dissipative-dispersive nonlinear system. *Phys. Fluids*, 31(8):2103–2111, 1988.

- [52] J. Muñoz-García, L. Vázquez, M. Castro, R. Gago, A. Redondo-Cubero, A. Moreno-Barrado, and R. Cuerno. Self-organized nanopatterning of silicon surfaces by ion beam sputtering. *Mater. Sci. Eng. R: Rep.*, 86:1, 2014.
- [53] G. Carter, M. J. Nobes, F. Paton, J. S. Williams, and J. L. Whitton. *Radiation Effects Defects Solids*, 33(2):65, 1977.
- [54] Adrian Keller, Steven Roßbach, Stefan Facsko, and Wolfhard Möller. Simultaneous formation of two ripple modes on ion sputtered silicon. *Nanotechnol.*, 19(13):135303, 2008.
- [55] Adrian Keller, Stefan Facsko, and Wolfhard Möller. Minimization of topological defects in ion-induced ripple patterns on silicon. *New J. Phys.*, 10(6):063004, 2008.
- [56] A. Metya, D. Ghose, S. A. Mollick, and A. Majumdar. Nanopatterning of mica surface under low energy ion beam sputtering. *J. Appl. Phys.*, 111(7):074306, 2012.
- [57] Debasree Chowdhury and Debabrata Ghose. High fluence effect on si ripple morphology developed by low energy ion beam sputtering. *AIP Conference Proceedings*, 1536(1):353–354, 2013.
- [58] M Teichmann, J Lorbeer, B Ziberi, F Frost, and B Rauschenbach. Pattern formation on ge by low energy ion beam erosion. *New J. Phys.*, 15:103029, 2013.
- [59] Marc Teichmann, Jan Lorbeer, Frank Frost, and Bernd Rauschenbach. Ripple coarsening on ion beam-eroded surfaces. *Nanoscale Res. Lett.*, 9(1):439, 2014.
- [60] Debasree Chowdhury and Debabrata Ghose. Tuning of nanopatterns on si (100) substrate: role of ion beam processing parameters during sputtering. *Advanced Science Letters*, 22(1):105–110, 2016.
- [61] R Gago, M Jaafar, and FJ Palomares. Surface morphology of molybdenum silicide films upon low-energy ion beam sputtering. *J. Phys.: Condens. Matter*, 30(26):264003, 2018.

- [62] A Lopez-Cazalilla, D Chowdhury, A Ilinov, S Mondal, P Barman, SR Bhattacharyya, D Ghose, F Djurabekova, K Nordlund, and S Norris. Pattern formation on ion-irradiated surface at energies where sputtering is negligible. *J. Appl. Phys.*, 123(23):235108, 2018.
- [63] M. Cross and H. Greenside. *Pattern Formation and Dynamics in Nonequilibrium Systems*. Cambridge University Press, Cambridge, England, 2009.
- [64] Derek Handwerk, Gerhard Dangelmayr, Iuliana Oprea, and Patrick D Shipman. Phase-diffusion equations for the anisotropic complex ginzburg-landau equation. *arXiv preprint arXiv:2009.12945*, 2020.
- [65] Roland Faller and Lorenz Kramer. Ordered defect chains in the 2d anisotropic complex ginzburg-landau equation. *Chaos, Solitons and Fractals*, 10(4):745–752, 1999.
- [66] Aly-Khan Kassam and Lloyd N Trefethen. Fourth-order time-stepping for stiff pdes. *SIAM Journal on Scientific Computing*, 26(4):1214–1233, 2005.
- [67] Richard V Craster and Roberto Sassi. Spectral algorithms for reaction-diffusion equations. *Tech. Report No. 99, Università degli studi di Milano*, 2006.
- [68] Steven M Cox and Paul C Matthews. Exponential time differencing for stiff systems. *Journal of Computational Physics*, 176(2):430–455, 2002.
- [69] Stein Krogstad. Generalized integrating factor methods for stiff pdes. *Journal of Computational Physics*, 203(1):72–88, 2005.
- [70] J Burke, S.M Houghton, and Edgar Knobloch. Swift-hohenberg equation with broken reflection symmetry. *Phys. Rev. E*, 80(3):036202, 2009.
- [71] The 1D DSHE without a quadratic nonlinearity [Eq. (3.8)] was studied for γ values of order one in A. Hariz, L. Bahloul, L. Cherbi, K. Panajotov, M. Clerc, M.A. Ferre, B. Kostet, E. Averlant, and M. Tlidi *Phys. Rev. A* **100**, 023816 (2019).

- [72] Francis C Motta, Rachel Neville, Patrick D Shipman, Daniel A Pearson, and R Mark Bradley. Measures of order for nearly hexagonal lattices. *Physica D: Nonlinear Phenomena*, 380:17–30, 2018.
- [73] Patrick D Shipman, Tejas Sharath, and R Mark Bradley. Topological measures of order for imperfect two-dimensional bravais lattices. *Physical Review E*, 107(4):044216, 2023.
- [74] Herbert Edelsbrunner and John L Harer. *Computational topology: an introduction*. American Mathematical Society, 2022.
- [75] Mathieu Carriere, Marco Cuturi, and Steve Oudot. Sliced wasserstein kernel for persistence diagrams. In *International conference on machine learning*, pages 664–673. PMLR, 2017.
- [76] Stefan Mátéfi-Tempfli, Mária Mátéfi-Tempfli, and Luc Piraux. Characterization of nanopores ordering in anodic alumina. *Thin Solid Films*, 516(12):3735–3740, 2008.
- [77] Franco P Preparata and Michael I Shamos. *Computational geometry: an introduction*. Springer Science & Business Media, 2012.
- [78] Daniel Walgraef. *Spatio-temporal pattern formation: with examples from physics, chemistry, and materials science*. Springer Science & Business Media, 2012.
- [79] Ting Yang, Hongshun Chen, Zian Jia, Zhifei Deng, Liuni Chen, Emily M Peterman, James C Weaver, and Ling Li. A damage-tolerant, dual-scale, single-crystalline microlattice in the knobby starfish, *protoreaster nodosus*. *Science*, 375(6581):647–652, 2022.
- [80] T Leppänen. Computational studies of pattern formation in turing systems [ph. d. thesis]. *Helsinki University of Technology*, 2004.
- [81] Hannes Uecker and Daniel Wetzel. Snaking branches of planar bcc fronts in the 3d brusselator. *Physica D: Nonlinear Phenomena*, 406:132383, 2020.

- [82] Anne De Wit, Pierre Borckmans, and Guy Dewel. Twist grain boundaries in three-dimensional lamellar turing structures. *Proceedings of the National Academy of Sciences*, 94(24):12765–12768, 1997.
- [83] Hiroto Shoji, Kohtaro Yamada, Daishin Ueyama, and Takao Ohta. Turing patterns in three dimensions. *Physical Review E*, 75(4):046212, 2007.
- [84] Brenden Balch, Patrick D Shipman, and R Mark Bradley. Spatially extended dislocations produced by the dispersive swift-hohenberg equation. *Physical Review E*, 107(4):044214, 2023.
- [85] Kevin M Loew and R Mark Bradley. Effect of dispersion on the nanoscale patterns produced by ion sputtering. *Phys. Rev. E*, 100(1):012801, 2019.
- [86] TK Callahan and E Knobloch. Pattern formation in three-dimensional reaction–diffusion systems. *Physica D: Nonlinear Phenomena*, 132(3):339–362, 1999.
- [87] RE Kelly and D Pal. Thermal convection with spatially periodic boundary conditions: resonant wavelength excitation. *Journal of Fluid Mechanics*, 86(3):433–456, 1978.
- [88] Mary Lowe, Jerry P Gollub, and TC Lubensky. Commensurate and incommensurate structures in a nonequilibrium system. *Physical Review Letters*, 51(9):786, 1983.
- [89] Mary Lowe and Jerry P Gollub. Solitons and the commensurate-incommensurate transition in a convecting nematic fluid. *Physical Review A*, 31(6):3893, 1985.
- [90] P Coulet. Commensurate-incommensurate transition in nonequilibrium systems. *Physical review letters*, 56(7):724, 1986.
- [91] P Coulet and P Huerre. Resonance and phase solitons in spatially-forced thermal convection. *Physica D: Nonlinear Phenomena*, 23(1-3):27–44, 1986.
- [92] P Coulet, C Elphick, and D Repaux. Nature of spatial chaos. *Physical review letters*, 58(5):431, 1987.

- [93] P Couillet and D Repaux. Strong resonances of periodic patterns. *Europhysics Letters*, 3(5):573, 1987.
- [94] Pierre Couillet and Daniel Walgraef. Spatial forcing of 2d wave patterns. *Europhysics letters*, 10(6):525, 1989.
- [95] LM Pismen. Bifurcation of quasiperiodic and nonstationary patterns under external forcing. *Physical review letters*, 59(24):2740, 1987.
- [96] Michel Henriot, Javier Burguete, and Roland Ribotta. Entrainment of a spatially extended nonlinear structure under selective forcing. *Physical review letters*, 91(10):104501, 2003.
- [97] Denis Semwogerere and Michael F Schatz. Evolution of hexagonal patterns from controlled initial conditions in a Bénard-Marangoni convection experiment. *Physical review letters*, 88(5):054501, 2002.
- [98] R Neubecker and A Zimmermann. Spatial forcing of spontaneous optical patterns. *Physical Review E*, 65(3):035205, 2002.
- [99] Sten Rüdiger, Ernesto M Nicola, Jaume Casademunt, and Lorenz Kramer. Theory of pattern forming systems under traveling-wave forcing. *Physics Reports*, 447(3-6):73–111, 2007.
- [100] Erik Holmes. *Shapes of pure prime degree number fields*. PhD thesis, University of Hawai'i at Manoa, 2021.
- [101] Manjul Bhargava and Piper Harron. The equidistribution of lattice shapes of rings of integers in cubic, quartic, and quintic number fields. *Compositio Mathematica*, 152(6):1111–1120, 2016.
- [102] J Burke, SM Houghton, and Edgar Knobloch. Swift-Hohenberg equation with broken reflection symmetry. *Physical Review E*, 80(3):036202, 2009.

- [103] R. Mark Bradley and Tejas Sharath. Nanoscale pattern formation on solid surfaces bombarded by two broad ion beams in the regime in which sputtering is negligible. *Physical Review E*, 103(2):022804, 2021.
- [104] William N Traves. Invariant theory and differential operators, 2007.